

ELECTRONIC AND MAGNETIC EXCITATIONS IN GRAPHENE AND  
MAGNETIC NANO-RIBBONS  
(Spine title: Excitations in graphene and magnetic nano-ribbons)  
(Thesis format: Monograph)

by

Maher Ahmed Selim

Graduate Program in Physics

A thesis submitted in partial fulfillment  
of the requirements for the degree of  
Doctor of Philosophy

The School of Graduate and Postdoctoral Studies  
The University of Western Ontario  
London, Ontario, Canada

© Maher Zakaria Ahmed Selim 2012

THE UNIVERSITY OF WESTERN ONTARIO  
School of Graduate and Postdoctoral Studies

**CERTIFICATE OF EXAMINATION**

Supervisor:

.....  
Dr. Michael G. Cottam

Supervisory Committee:

.....  
Dr. Giovanni Fanchini

.....  
Dr. Jeff L. Hutter

.....  
Dr. T. Aaron Sigut

Examiners:

.....  
Dr. Jan Cami

.....  
Dr. Giovanni Fanchini

.....  
Dr. Francois Lagugne-Labarthe

.....  
Dr. Fereidoon S. Razavi

The thesis by

**Maher Zakaria Ahmed Selim**

entitled:

**Electronic and magnetic excitations in graphene and magnetic nano-ribbons**

is accepted in partial fulfillment of the  
requirements for the degree of  
Doctor of Philosophy

.....  
Date

.....  
Chair of the Thesis Examination Board

# Abstract

The discovery of graphene - a 2D material with superior physical properties - in 2004 was important for the intensive global research to find alternatives to three-dimensional (3D) semiconductor materials in industry. At the same time there have been exciting advances for 2D magnetic materials on the nanometer scale. The superior properties of graphene are mainly attributed to its crystal structure and its relatively short-range interactions. These properties show that natural and artificial 2D materials are promising for new applications.

In this thesis we have carried out a comprehensive investigation of the effects of the 2D lattice structures, the roles of nearest neighbor (NN) and next nearest neighbor (NNN) interactions and the formation of coupled bilayer systems in both the electronic and the magnetic geometries (chosen specifically to be nano-ribbons or stripes). In the case of honeycomb lattices (which occur in graphene and can be produced artificially by growing nanodot arrays for ferromagnetic structures) the effects of different edges of the zigzag and armchair types are studied with emphasis on the localized modes that may occur. Impurity sites in the form of one or more lines of impurities introduced substitutionally are considered from the perspectives that they give additional localized mode effects and they change the spatial quantization (for example, as studied via the density of states for the modes). The theoretical methods employed throughout the thesis are based on the second quantization forms of both the tight-binding Hamiltonian for electronic excitations and the Heisenberg exchange Hamiltonian for the ferromagnetic excitations (or spin waves). The translational symmetry along the length of the ribbon or stripe is utilized to make a wave-vector Fourier transform in this longitudinal direction, while the finite number of rows in the transverse direction are treated within a matrix formulation.

**Keywords:** 2D materials, 2D honeycomb lattice, 2D square lattice, graphene nanoribbons, AA-graphene bilayer, spin waves, magnetic nanodots arrayed stripes, zigzag localized edge states, 2D tight binding model, 2D Heisenberg model, next nearest neighbor interaction, nearest neighbor interaction, localized impurity modes, density of states.

## **Acknowledgement**

I kneel humbly to **ALLAH** thanking **HIM** for showing me the right path. Without **HIS** help my efforts would have gone astray. May God send His praises upon his Beloved Prophet Muhammad

My sincere thanks are dedicated to the Egyptian ministry of higher education and scientific research for funding my PhD scholarship, and to my supervisor Prof. M. G. Cottam for his guidance in my graduate studies.

I would like to express my sincere thanks to my parents and my family for their continuous help and encouragement.

# Contents

<b>Certificate of Examination</b>	<b>ii</b>
<b>Abstract</b>	<b>iii</b>
<b>Acknowledgements</b>	<b>iv</b>
<b>List of Figures</b>	<b>vii</b>
<b>List of Tables</b>	<b>xii</b>
<b>List of Appendices</b>	<b>xiii</b>
<b>List of Acronyms</b>	<b>xiv</b>
<b>1 Introduction</b>	<b>1</b>
1.1 Introduction to carbon and graphene . . . . .	5
1.2 Tight binding model for graphene . . . . .	11
1.2.1 Second quantization form of the Hamiltonian . . . . .	18
1.3 Magnetic properties of 2D stripe systems . . . . .	19
1.3.1 Heisenberg exchange Hamiltonian . . . . .	21
1.3.2 Spin waves in ferromagnets . . . . .	24
1.4 Thesis outline . . . . .	29
<b>2 Spin Waves in Ferromagnetic Stripes</b>	<b>31</b>
2.1 Introduction . . . . .	31
2.2 Theoretical model . . . . .	33
2.2.1 Special case of $N \rightarrow \infty$ . . . . .	41
2.2.2 Case of large finite $N$ . . . . .	43
2.3 Numerical calculations . . . . .	44
2.4 SW dispersion relations . . . . .	47
2.4.1 Tridiagonal matrix method results . . . . .	48
2.4.2 Direct diagonalization method results . . . . .	51
2.5 Discussion . . . . .	56
<b>3 Spin Waves in Ferromagnetic Stripes with a Honeycomb Lattice</b>	<b>58</b>
3.1 Introduction . . . . .	58
3.2 Theoretical model . . . . .	60

3.3	Method for numerical calculations . . . . .	65
3.4	SW results for zigzag stripes . . . . .	68
3.4.1	SW dispersion relations . . . . .	68
3.4.2	Density of states . . . . .	71
3.5	SW results for armchair stripes . . . . .	82
3.5.1	SW dispersion relations . . . . .	82
3.5.2	Density of states . . . . .	84
3.6	Discussion and Conclusions . . . . .	93
<b>4</b>	<b>Localized States in Semi-Infinite Zigzag Edged Graphene</b>	<b>94</b>
4.1	Introduction . . . . .	94
4.2	Theory for edge states and impurity states . . . . .	95
4.3	Numerical results . . . . .	103
4.4	Discussion and Conclusions . . . . .	109
<b>5</b>	<b>The Effect of Next Nearest Neighbors on the Properties</b>	<b>112</b>
5.1	Introduction . . . . .	112
5.2	Theoretical model . . . . .	113
5.3	Numerical results . . . . .	119
5.4	Discussion and Conclusions . . . . .	123
<b>6</b>	<b>Some Properties of Bilayer Graphene Nanoribbons</b>	<b>125</b>
6.1	Introduction . . . . .	125
6.2	Theoretical model . . . . .	126
6.3	Numerical results . . . . .	134
6.4	Discussion and Conclusions . . . . .	139
<b>7</b>	<b>Conclusions</b>	<b>140</b>
	<b>Bibliography</b>	<b>144</b>
<b>A</b>	<b>Algorithms used in Chapter 2</b>	<b>162</b>
A.1	Algorithm 1 . . . . .	162
A.2	Algorithm 2 . . . . .	163
<b>B</b>	<b>Derivation of Equation (4.6)</b>	<b>164</b>
<b>C</b>	<b>Partitioning of the <math>D_N</math> matrix in Chapter 4</b>	<b>167</b>
	<b>Curriculum Vitae</b>	<b>171</b>

# List of Figures

1.1	Kurzweil’s extension of Moore’s law from integrated circuits to earlier transistors, vacuum tubes, relays and electromechanical computers. [3]	2
1.2	$\sigma$ ( $\sigma^*$ ) bonding between two hybridized $sp^2$ orbitals, Figure taken from [34].	7
1.3	$\pi$ ( $\pi^*$ ) bonding between two hybridized $sp^2$ orbitals, Figure taken from [34].	7
1.4	Graphene is the mother of all other forms. Figure taken from [8].	8
1.5	The (a) unit cell of graphene is the rhombus shown, and (b) the first Brillouin zone of graphene is the shaded hexagon. Figure taken from [6].	9
1.6	Part of a honeycomb lattice showing both zigzag and armchair edges. Figure taken from [33].	10
1.7	Energy dispersion relation for a graphene single layer, drawn in the first Brillouin zone. The energy bands depend only on $q_x$ and $q_y$ . The $\pi$ band is completely filled and meets the totally empty $\pi^*$ band at the K points. Near these points both bands have a linear dispersion. (b) The dispersion along the high-symmetry points $\Gamma$ MK. Figure taken from [20].	17
1.8	Electronic dispersion in the honeycomb lattice (in units of the NN hopping $t$ ) for finite values of $t_0$ and $t_1$ , with $t_0=2.7$ eV and $t_1=0.2t$ . Right: zoom in of the energy bands close to one of the Dirac points. Figure taken from [33].	18
1.9	Possible configurations due to Coulomb interaction between two electrons at neighboring sites in a spin lattice. The curves show the two-electron wave-function envelopes: (a) parallel alignment of spins, (b) anti-symmetry of the spatial wave function, (c) anti-parallel spin configurations, (d) Coulomb interaction between electrons with opposite spin populating the same site. Figure taken from [46].	22
1.10	Spin-wave excitation (magnon) from the spin ground state of a ferromagnet. Figure taken from [46].	25
1.11	Spin-wave spectrum of europium oxide as measured by inelastic neutron scattering at a reference temperature of 5.5 K. Figure taken from [67].	27
2.1	Geometry of a 2D Heisenberg ferromagnetic square lattice nanoribbon. The spins are in the $xy$ -plane and the average spin alignment is in the $z$ direction. The nanoribbon is finite in the $y$ direction with $N$ atomic rows ( $n = 1, \dots, N$ ).	33
2.2	Calculated values of $x^+$ and $x^-$ for several values of $\Delta < -1$ and for $N$ from 10 to 100.	43

2.3	The values for minimum positive (P) and maximum negative (N) of $\Delta$ for even (E) and odd (O) number $N$ that satisfy the edge modes condition (2.28), are computed from the first polynomial (F) (2.26) and from the second polynomial (S) (2.27). . . . .	46
2.4	Frequencies of the edge SW modes (in units of $SJ$ ) plotted against the wavevector $q_x a$ for stripe with width $N = 3$ , where the lines corresponding to $x = 1$ and $x = -1$ are the upper and lower boundary for the area modes. . . . .	49
2.5	Frequencies of the edge SW modes (in units of $SJ$ ) plotted against the wavevector $q_x a$ for stripe with width $N = 4$ , where the lines corresponding to $x = 1$ and $x = -1$ are the upper and lower boundary for the area modes. . . . .	49
2.6	Frequencies of the edge SW modes (in units of $SJ$ ) plotted against the wavevector $q_x a$ for stripe with width $N = 7$ , where the lines corresponding to $x = 1$ and $x = -1$ are the upper and lower boundary for the area modes. . . . .	50
2.7	Frequencies of the edge SW modes (in units of $SJ$ ) plotted against the wavevector $q_x a$ for stripe with width $N = 8$ , where the lines corresponding to $x = 1$ and $x = -1$ are the upper and lower boundary for the area modes. . . . .	50
2.8	SW dispersion relations for area and edge modes for pure material ferromagnetic 2D square lattice stripes for $N = 8$ where $D = D_e = D_I = 1.0$ and $\alpha = -0.95$ (a) $J_e = J$ (b) $J_e = 0.5J$ (c) $J_e = 0.1J$ . . . . .	53
2.9	SW dispersion relations for area and edge modes for material with an impurity ferromagnetic 2D square lattice stripes for $N = 8$ where $D = D_e = D_I = 1.0$ and with adding an impurity line at line number 4 for $J_e = 0.1J$ with (d) $J_I = 0.0J$ (e) $J_I = 0.5J$ (f) $J_I = 0.9J$ . . . . .	54
3.1	Armchair (left) and zigzag (right) edges for 2D Heisenberg ferromagnetic dots forming honeycomb stripes in the $xy$ -plane. The black (gray) dots refer to the sublattice A(B) with the additional possibility of a line of impurities (white dots) in the middle of the sheet. The stripes are finite in the $y$ direction with $N$ rows ( $n = 1, \dots, N$ ) and they are infinite in the $x$ direction. . . . .	60
3.2	SW dispersion for zigzag ferromagnetic honeycomb stripes with $N = 20$ , $J = J_e = 1$ , $D = D_e = 0$ and $\alpha = 0.01$ . . . . .	70
3.3	SW dispersion for zigzag ferromagnetic honeycomb stripes with $N = 20$ , $J = J_e = 1$ , $D = D_e = 1.0$ and $\alpha = 1.01$ . . . . .	70
3.4	SW dispersion for zigzag ferromagnetic honeycomb stripes with $N = 21$ , $J = J_e = 1$ , $D = D_e = 1$ and $\alpha = 1.01$ . . . . .	71
3.5	SW dispersion for zigzag ferromagnetic honeycomb stripes with an impurity line at line number 11, where $N = 20$ , $J = J_e = 1$ , $J_I = 0.0J$ $D = D_e = D_I = 1.0$ and $\alpha = 1.01$ . . . . .	72
3.6	SW dispersion for zigzag ferromagnetic honeycomb stripes with an impurity line at line number 11, where $N = 21$ , $J = J_e = 1$ , $J_I = 0.0J$ $D = D_e = D_I = 1.0$ and $\alpha = 1.01$ . . . . .	72
3.7	SW dispersion for zigzag ferromagnetic honeycomb stripes with two impurities lines at line number 11 and line number 14, where $N = 20$ , $J = J_e = 1$ , $J_I = 0.0J$ , $J_{II} = 0.0J$ , $D = D_e = D_I = 1.0$ and $\alpha = 1.01$ . . . . .	73



3.8	SW dispersion for zigzag ferromagnetic honeycomb stripes with two impurities lines at line number 11 and line number 14, where $N = 21$ , $J = J_e = 1$ , $J_I = 0.0J$ , $J_{II} = 0.0J$ , $D = D_e = D_I = 1.0$ and $\alpha = 1.01$ . . . . .	73
3.9	The effect of stripe width on the relative density of states near the Fermi level (RDSFL) in the zigzag case. . . . .	74
3.10	The effect of stripe width on the relative density of states of the center band (RDSCB) in the zigzag case. . . . .	75
3.11	Contour plot for the effects of edge uniaxial anisotropy and zigzag stripe width on the RDSCB . . . . .	76
3.12	The effects of edge exchange and zigzag stripe width on the RDSCB . . . . .	76
3.13	The effects of position and impurity exchange for $N = 20$ zigzag stripe on the RDSCB in the case of one line of impurities. . . . .	77
3.14	The effect of a second line of impurities position and impurities exchange on the RDSCB for a $N = 20$ zigzag stripe. There is one line of impurities at $N = 11$ with impurities exchange $J_I = 0$ . . . . .	78
3.15	The effect of one line of impurities position and impurities exchange for a $N = 21$ zigzag stripe on its RDSCB . . . . .	79
3.16	The effect of a second line of impurities position and impurities exchange for a $N = 20$ zigzag stripe with one line of impurities at $N = 11$ with impurities exchange $J_I = 0$ on its RDSCB . . . . .	80
3.17	SW dispersion for armchair 2D Heisenberg ferromagnetic honeycomb stripes with $J = J_e = 1.0$ , $D = D_e = 1.0$ , and $\alpha = 1.01$ for $N = 20, 21$ and $22$ respectively. . . . .	81
3.18	SW dispersion for armchair 2D Heisenberg ferromagnetic honeycomb stripes with an impurity line at line number 11, where $J = J_e = 1$ , $J_I = 0.0J$ , $D = D_e = D_I = 1.0$ and $\alpha = 1.01$ for $N = 20, 21$ and $22$ respectively. . . . .	83
3.19	SW dispersion for armchair 2D Heisenberg ferromagnetic honeycomb stripes with an impurity lines at line number 11 and line number 14, where $J = J_e = 1$ , $J_I = J_{II} = 0.0J$ , $D = D_e = D_I = 1.0$ and $\alpha = 1.01$ for $N = 20, 21$ and $22$ respectively. . . . .	85
3.20	The effect of armchair stripe width for the three armchair types on the relative density of states of center band (RDSCB) . . . . .	86
3.21	The effects of edge uniaxial anisotropy and armchair stripe width on its RDSCB	87
3.22	The effects of edge exchange and zigzag stripe width on its RDSCB . . . . .	88
3.23	The effect of one line of impurities position and impurities exchange on the armchair stripe RDSCB for stripes width $N = 20, 21$ and $22$ respectively. . . . .	89
3.24	The effect of a second line of impurities position and impurities exchange on the armchair stripe RDSCB with one line of impurities at $N = 11$ with impurities exchange $J_I = 0$ for stripes width $N = 20, 21$ and $22$ respectively. . . . .	90
3.25	The variation of bandgaps of the three types of armchair stripes as a function of width (number of rows) $W$ . . . . .	91
3.26	Variation of the energy gap versus the strength of the edge exchange for armchair stripes. The solid line is for a 20-line ribbon, dashed line for 21 lines, and dotted line for a stripe with 22 lines. . . . .	92

3.27	Variation of the energy gap versus the strength of the impurity exchange when the impurities line is in the 11th line of armchair stripes. The solid line is for a 20-line stripe, dashed line for 21 lines, and dotted line for a stripe with 22 lines.	92
4.1	Geometry of a graphene ribbon with zigzag edges. The black (gray) dots are the sublattice $A$ ( $B$ ) atoms, where $A(B)$ sublattice type are labeled by index $n(n')$ ( $= 1, 2, \dots, N$ ) and the white dots show a row of impurities. Figure taken from [39].	96
4.2	Edge localized states for different edge hopping calculated with $\Delta_s = 0$ , where the shaded band represent the area modes continuum.	104
4.3	Edge localized states for different edge hopping calculated with a nonzero value of $\Delta_s = -2.61$ , where the shaded band represent the area modes continuum.	104
4.4	The variation of TRLDOS, FRLDOS, and LOFRLDOS as a function of edge hopping ratio from 0 to 2.9. (a) for $\Delta_s = 0$ and (b) for $\Delta_s = -2.61$ .	105
4.5	The variation of TRLDOS, FRLDOS, and LOFRLDOS as functions of the impurities hopping from 0 to 2.9 for the impurities line in sublattice $A$ at positions (a) 2, (b) 3, (c) 4, and (d) 5.	108
4.6	The localized edge and impurities states (indicated by black dots) plotted versus wavevector to illustrate the effects of an edge and two lines of impurities at sublattice $A$ . The shaded band represents the area modes continuum. The edge hopping is $t_e/t = 0.5$ , the first impurities line position is $n_0 = 4$ with the impurities hopping $t_{n_0}/t = 1.5$ , and the second impurities line position is $n'_0 = 7$ with the impurities hopping $t_{n'_0}/t = 0.3$ .	109
5.1	Armchair (left) and zigzag (right) graphene 2D honeycomb nanoribbons in the $xy$ -plane, where the black (gray) dots are the sublattice sites $A(B)$ with a line of impurities (white dots) in the middle of the sheet. The stripes are finite in the $y$ direction with $N$ rows ( $n = 1, \dots, N$ ) and they are infinite in the $x$ direction. Figure taken from [39].	113
5.2	The effect of NNN interaction on the dispersion relations, edge states, and impurities states in the graphene zigzag nanoribbons. Left side: stripe width $N = 20$ with (a) $t' = 0.036t$ (b) $t' = 0.1t$ (c) $t' = 0.1t$ and with the impurities line at row number 11 with $J_I = 0$ . Right side: stripe width $N = 21$ with (d) $t' = 0.036t$ (e) $t' = 0.1t$ (f) $t' = 0.1t$ and with the impurities line at row number 11 with $J_I = 0$ .	120
5.3	The effect of NNN interaction on the dispersion relations, band gap, and impurities states in the graphene armchair nanoribbons. Left side: $t' = 0.1t$ for stripe width (a) $N = 20$ (b) $N = 21$ (c) $N = 22$ . Right side: $t' = 0.1t$ and with the impurities line at row number 11 with $J_I = 0$ for stripe width (d) $N = 20$ (e) $N = 21$ (f) $N = 22$ .	121
5.4	The effect of a higher NNN interaction corresponding to $t' = 0.5t$ on the dispersion relations on the zigzag (left panel) and armchair (right panel) nanoribbons with width $N = 20$ .	123

6.1	Direct on-top AA-stacking bilayer graphene (BLG). Left: the 2D unit cell is shown $a = b = 0.267nm$ , $\gamma = 120^\circ$ . Right: AA-stacking BLG nanoribbons. Figures taken from [143, 142]. . . . .	127
6.2	The tunable dispersion relations of AA-BLG nanoribbons with zigzag edge and width $N = 20$ . (a) $\gamma_0 = 0.0$ (b) $\gamma_0 = 0.12$ and $t' = 0.036t$ (c) $\gamma_0 = 0.12$ , $t' = 0.036t$ , $N_{ii} = 11$ , and $t_{ii} = 0.0t_t$ (d) $\gamma_0 = 0.12$ , $t' = 0.036t$ , $N_{ii} = 11$ , $t_{ii} = 0.0t_t$ , $N_{bi} = 14$ , and $t_{bi} = 0.0t_b$ . . . . .	134
6.3	The tunable dispersion relations of AA-BLG nanoribbons with zigzag edge and width $N = 21$ . (a) $\gamma_0 = 0.0$ (b) $\gamma_0 = 0.12$ and $t' = 0.036t$ (c) $\gamma_0 = 0.12$ , $t' = 0.036t$ , $N_{ii} = 11$ , and $t_{ii} = 0.0t_t$ (d) $\gamma_0 = 0.12$ , $t' = 0.036t$ , $N_{ii} = 11$ , $t_{ii} = 0.0t_t$ , $N_{bi} = 14$ , and $t_{bi} = 0.0t_b$ . . . . .	135
6.4	The tunable dispersion relations of AA-BLG nanoribbons with armchair edge and width $N = 20$ . (a) $\gamma_0 = 0.0$ (b) $\gamma_0 = 0.12$ and $t' = 0.036t$ . . . . .	136
6.5	The tunable dispersion relations of AA-BLG nanoribbons with armchair edge and width $N = 21$ . (a) $\gamma_0 = 0.0$ (b) $\gamma_0 = 0.12$ and $t' = 0.036t$ . . . . .	136
6.6	The tunable dispersion relations of AA-BLG nanoribbons with armchair edge and width $N = 22$ . (a) $\gamma_0 = 0.0$ (b) $\gamma_0 = 0.12$ and $t' = 0.036t$ . . . . .	137
6.7	For comparison, the tunable dispersion relations of 2D square lattice magnetic stripes with width $N = 8$ . (a) $\gamma_0 = 0.0$ (b) $\gamma_0 = 0.12$ and $t' = 0.036t$ . . . . .	137

# List of Tables

2.1	Nearest neighbor exchange matrix elements for 2D square lattice . . . . .	52
3.1	Nearest neighbor exchange matrix elements for a 2D magnetic honeycomb lattice	65
4.1	NN hopping matrix elements for the zigzag graphene nanoribbon . . . . .	96
5.1	NN hopping matrix elements for the graphene honeycomb lattice . . . . .	117
5.2	NNN hopping matrix elements for the graphene honeycomb lattice . . . . .	117

# List of Appendices

Appendix A Algorithms used in Chapter 2 . . . . .	162
Appendix B Derivation of Equation (4.6) . . . . .	164
Appendix C Partitioning of the $D_N$ matrix in Chapter 4 . . . . .	167

# List of Acronyms

<b>2D</b>	Two Dimensional
<b>3D</b>	Three Dimensional
<b>BLGs</b>	Bilayer Graphenes
<b>CNTs</b>	Carbon Nanotubes
<b>DFT</b>	Density Functional Theory
<b>DD</b>	Direct Diagonalization method
<b>GNRs</b>	Graphene Nanoribbons
<b>GSL</b>	Graphene Single Layer
<b>HTS</b>	High-Temperature Superconductors
<b>HP</b>	Holstein-Primakoff transformation
<b>LOFRLDOS</b>	Liftoff Percentage of Relative Localized Density of States near Fermi level
<b>NN</b>	Nearest Neighbor
<b>NNN</b>	Next Nearest Neighbor
<b>QED</b>	Quantum Electrodynamics
<b>RDSFL</b>	Relative Density of States near Fermi Level
<b>RDSCB</b>	Relative Density of States of Center Band
<b>FRLDOS</b>	Relative Localized Density of States near Fermi level
<b>SW</b>	Spin Wave
<b>TBM</b>	Tight-Binding Model
<b>TRLDOS</b>	Total Relative Localized Density of States
<b>TM</b>	Tridiagonal Matrix method
<b>ZGNR</b>	Zigzag Graphene Nanoribbons

# Chapter 1

## Introduction

It is clear from the recorded history of mankind on Earth that the human ability to understand the physics of the Earth's materials was the starting point to build human civilization. A key step was knowing the properties of stone, which was used by humans without any engineering skills in the Stone Age.

From this start our knowledge of the Earth's materials has increased, first to include copper in the Bronze Age and then iron in the Iron Age [1], until at the beginning of the 20th century a revolution in the understanding of the physics of materials happened. This was mainly due to the use of x-rays in crystallography and to the use of the newly-discovered quantum mechanics in material science [2]. It was the first time that mankind understood the electronic structure of materials at the atomistic level, thus allowing the engineering of the materials properties. This ability has changed the face of civilization on Earth with many applications that cover all aspects of human lives, for example in communication, computation, and automation.

In the computing field, for example, the growth of physics materials research has translated to technological increases in computing speeds along with decreases in the costs. Kurzweil

found that computing devices have been consistently multiplying in the number of calculations (per units of time and cost). This is an extension of the famous Moore's law (see Figure 1.1) of integrated circuits [3]:

“Moore's law of Integrated Circuits was not the first, but the fifth paradigm to forecast accelerating price-performance ratios. Each time one paradigm runs out of steam, another picks up the pace. Computing devices have been consistently multiplying in power (per unit of time) from the mechanical calculating devices used in the 1890 U.S. Census, to the CBS vacuum tube computer that predicted the election of Eisenhower, to the transistor-based machines used in the first space launches, to the integrated-circuit-based personal computer.” [3]

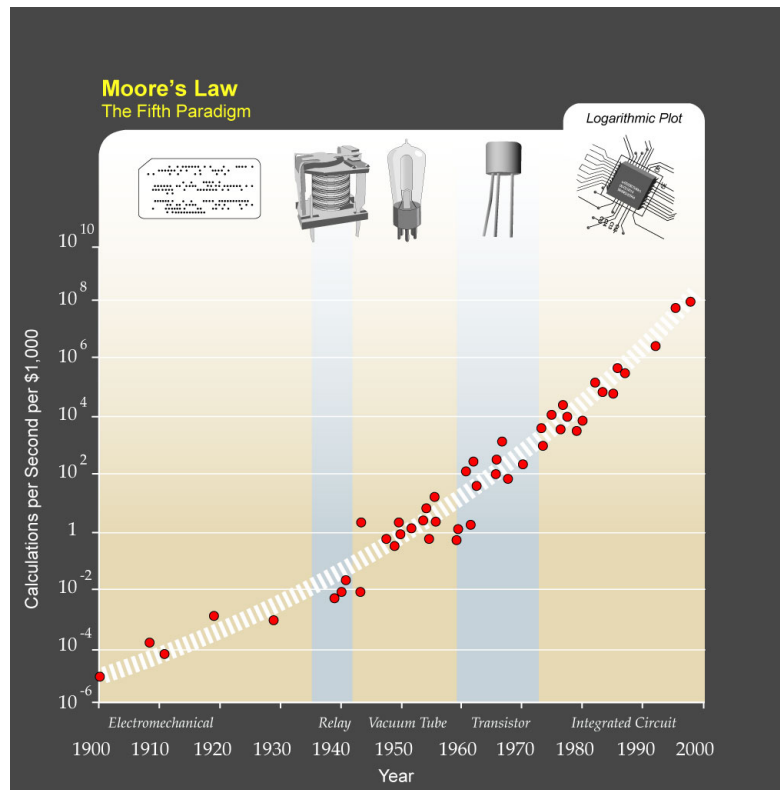


Figure 1.1: Kurzweil's extension of Moore's law from integrated circuits to earlier transistors, vacuum tubes, relays and electromechanical computers. [3]

The technology exists now in the Moore's law paradigm in which three dimensional (3D)



semiconductor physics and photolithography are used in integrated circuits technology. The photolithography technique has been used for several decades for the continuing miniaturization of electronics by increasing the density of transistors per unit area, in order to carry out faster and faster electronic processes. However, due to the physical and the technological limitations the process of miniaturization soon will be difficult to continue [4, 3]. To overcome these limitations, there is intensive research globally for new materials and technologies that work to extend Moore's law, i.e., a new physics of materials and a new paradigm [4, 3, 5]. Since the 3D semiconductor physics is used in the Moore's law paradigm, the research has been directed to new materials where the electrons are restricted to move in 2D, 1D, or 0D. In particular the 2D materials offer very important properties for applications [4, 6, 7, 8].

Already the physics of 2D play an important role in many 3D physical systems, such as the high-temperature superconductors (HTS), where the electronic interactions in the copper-oxygen planes play a major role [9, 10, 11], and also in graphite where 2D carbon sheets (called graphene) with a thickness of just one atom play a great role in the physical properties [12, 13, 14].

In 2004 Andre Geim and Konstantin Novoselov [15, 8, 7, 16, 17] used scotch tape in a remarkably simple technique to extract, for first time, a flake of carbon with a thickness of just one atom, i.e., graphene from graphite. They also measured its properties, which showed many superior features [18, 19, 4, 8, 7, 16, 17, 20]:

“Graphene is a wonder material with many superlatives to its name. It is the thinnest material in the universe and the strongest ever measured. Its charge carriers exhibit giant intrinsic mobility, have the smallest effective mass (it is zero)

and can travel micrometer-long distances without scattering at room temperature. Graphene can sustain current densities 6 orders higher than copper, shows record thermal conductivity and stiffness, is impermeable to gases and reconciles such conflicting qualities as brittleness and ductility. Electron transport in graphene is described by a Dirac-like equation, which allows the investigation of relativistic quantum phenomena in a bench-top experiment.” [17]

The above properties make graphene a prime candidate to replace silicon in industry and start a new paradigm for electronics [4, 16, 21, 5]. The first graphene experimental publication began what has nowadays become a graphene ‘gold rush’ [22, 20], which comes from the huge number of researchers who are working toward creating graphene applications. Some examples are single-molecule gas detectors [23], 100-GHz graphene transistors [24, 25], transparent conducting electrodes [26], light-emitting devices [27], a reference material for electrical standards [28], solar cells [29], ultracapacitors [29], graphene biodevices [30], and anti-bacterial devices [31]. The groundbreaking experiments on graphene by Andre Geim and Konstantin Novoselov resulted in them being awarded the Nobel Prize in Physics for 2010. There are many review articles that are recommended for more information about graphene (see, e.g., [19, 32, 20, 33, 5, 4, 6]).

The aim of this introductory chapter is to cover the main principles and concepts that will be used in the following chapters for graphene. We also provide an introduction to 2D ferromagnetic ribbons or stripes, which are physically quite distinct from graphene but are formally similar with respect to some of the mathematical techniques to be employed.

## 1.1 Introduction to carbon and graphene

To help understand the structure and the properties of graphene, the physics and chemistry of carbon will first be reviewed in this section. Carbon (C) is the chemical element of all lifeforms on the earth. C has six electrons, i.e., its atomic number is 6, there are three naturally occurring isotopes with  $^{12}\text{C}$  and  $^{13}\text{C}$  being stable while  $^{14}\text{C}$  is radioactive. The electronic structure of the free carbon atom is  $1s^2 2s^2 2p^2$  [34]. Carbon is unique in that it can form a vast number and variety of compounds [35], due to its ability to form different stable bonding by its hybridized atomic orbitals. The carbon hybridized atomic orbitals are formed by the mixing of its electronic orbitals wavefunctions to minimize the binding energy of that carbon atom with its neighboring atoms [34, 6].

For a carbon atom there are three possible ways of mixing for the spherical symmetric  $2s$  orbital and the three suborbitals  $2p_x$ ,  $2p_y$ , and  $2p_z$ . The first possibility is the mixing of  $2s$  with one suborbital of  $2p$ , for example  $2p_x$ , to create two  $sp$  hybridized orbitals, such as found in acetylene  $\text{HC}\equiv\text{CH}$  [34, 6].

The second possibility is the mixing of  $2s$  with two suborbitals of  $2p$ , for example  $2p_x$  and  $2p_y$ , to create three  $sp^2$  lying in one plane with angle  $120^\circ$ , while the remaining  $2p_z$  orbital is normal to the plane of the  $sp^2$ .

The third possibility is the mixing of  $2s$  with all three  $2p$  suborbital ( $2p_x$ ,  $2p_y$ , and  $2p_z$ ) to create four  $sp^3$  with tetragonal symmetry.

When the carbon atoms participate in any chemical reaction, the hybridized orbitals share their electrons, leading to two possibilities. One way is when two orbitals, like two  $sp^2$ , overlap in phase along an axis between the atoms, i.e., the orbitals overlap in an head-to-head fashion,

and they form a sigma ( $\sigma$ ) bond. In the case when the overlap of the two orbitals is out of phase, they form a sigma antibond  $\sigma^*$ . For a  $\sigma(\sigma^*)$  bond the electron density is highest (lowest) in the space between the atoms [34, 6], as illustrated in Figure 1.2. The other way is when two orbitals, like two  $2p_z$ , overlap side by side such that the orbitals overlap in phase (out of phase). Then they form a pi bond (pi antibond) denoted by  $\pi(\pi^*)$  [34, 6], as in Figure 1.3.

In order to understand the bonding of carbon atoms in graphene, we first consider a ring of six carbon atoms bonded together as in the benzene ( $C_6H_6$ ) molecule. Benzene is a ring of six carbon atoms with three double bonds shared equally among them, just as in graphene. The six  $2p_z$  orbitals are all parallel to one another, and each contains one electron. Therefore there are three  $\pi$  bonds, but due to energy considerations those three  $\pi$  bonds are delocalized over the whole molecular ring [34, 6]. This also shows how the  $2p_z$  orbitals lead to the delocalized carriers in graphene, which is a reason for graphene's superior properties [33, 4, 8, 7, 16, 17, 20]. According to the kind of hybridization of the atomic orbitals for the carbon atoms, their bonding types ( $\sigma$  or  $\pi$ ) are determined such as to create several possible allotropes of carbon, of which the best known are diamond, graphite, graphene, carbon nanotubes (CNTs), and fullerenes [6].

Graphene can be defined as a flat monolayer of carbon atoms tightly packed into a 2D honeycomb lattice. It is a basic building block for graphitic materials of all other dimensionalities. It can be wrapped up into 0D fullerenes, rolled into 1D nanotubes or stacked into 3D graphite [8, 16]. In this thesis we will focus on planar geometries and develop the theoretical models accordingly. The atomic orbitals of carbon atoms in graphene are  $sp^2$  hybridized, with the three planar  $sp^2$  suborbitals for each carbon atom being used to make three very strong planar  $\sigma$  bonds with other carbon atoms. This leads to the formation of planar hexagonal carbon rings,

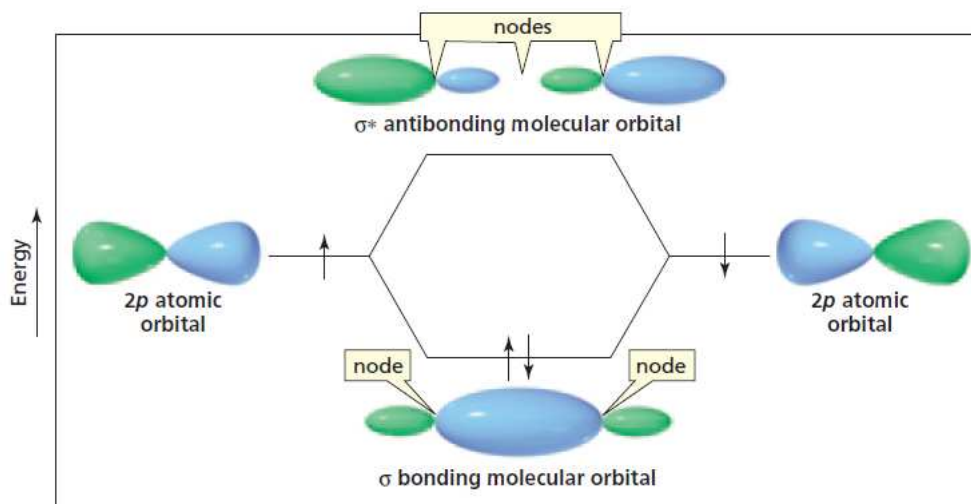


Figure 1.2:  $\sigma$  ( $\sigma^*$ ) bonding between two hybridized  $sp^2$  orbitals, Figure taken from [34].

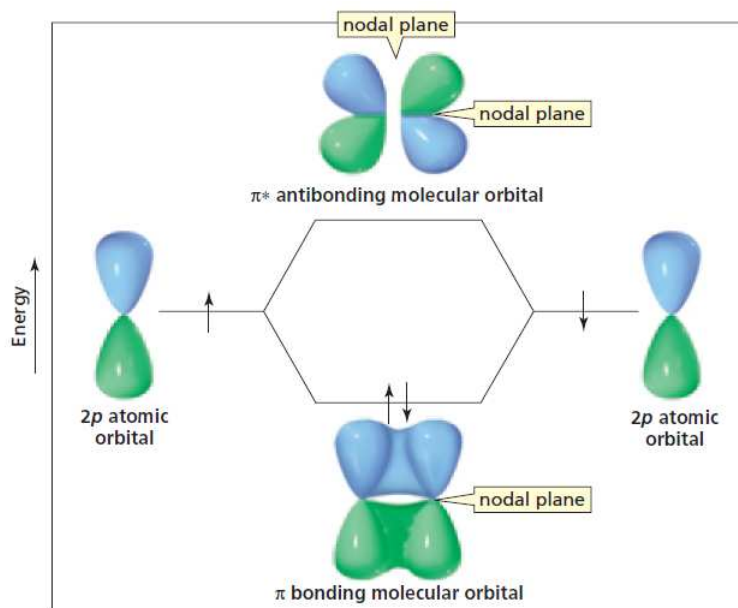


Figure 1.3:  $\pi$  ( $\pi^*$ ) bonding between two hybridized  $sp^2$  orbitals, Figure taken from [34].

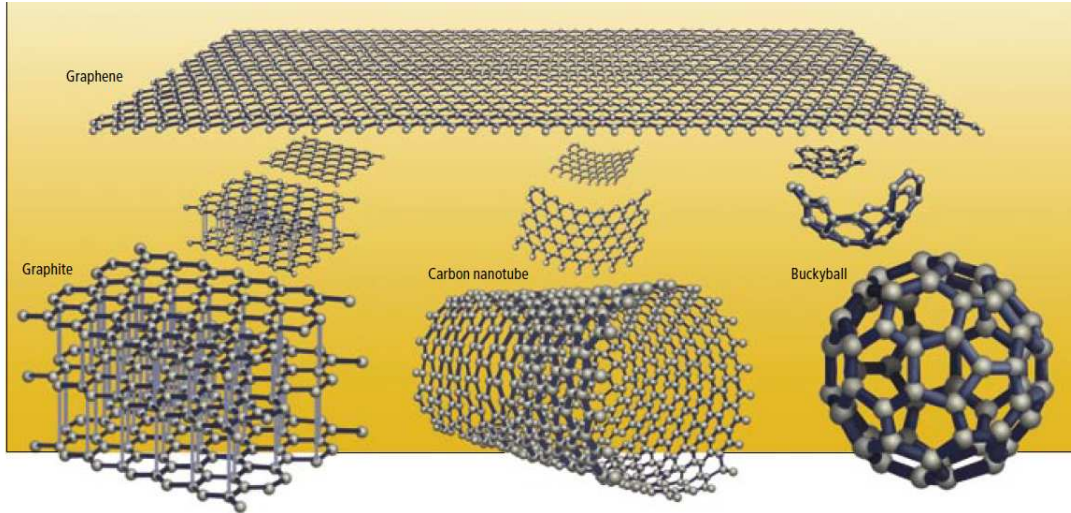


Figure 1.4: Graphene is the mother of all other forms. Figure taken from [8].

i.e., a 2D honeycomb lattice of carbon atoms which is “graphene”. All the  $2p_z$  orbitals are used to form  $\pi$  bonds, which create delocalized electrons, and these are capable of moving freely in the 2D honeycomb lattice of carbon atoms. At low energy the delocalized electrons behave like 2D relativistic free particles, which can be described by quantum electrodynamics (QED) in 2D. They are the reason behind graphene superior properties [33, 4, 8, 7, 16, 17, 20, 36].

To explain the motion of delocalized electrons of  $\pi$  bonds a crystallographic description for the graphene lattice is needed. There is no set of lattice vectors such that their primitive translations can describe graphene, i.e., graphene does not correspond to a Bravais lattice [37]. Actually, graphene can be described by two sublattices (labeled A and B) that are triangular Bravais lattices, i.e., it is a bipartite lattice (see Figure 1.5).

The unit cell of this system of two triangular sublattices A and B of graphene is a rhombus, which contains two atoms per unit cell. The nearest neighbors of the A sites are always B sites

and vice versa [20, 33, 6] (see Figure 1.5). The lattice vectors are conveniently written as

$$\mathbf{a}_1 = \frac{a}{2}(1, \sqrt{3}) \quad \mathbf{a}_2 = \frac{a}{2}(-1, \sqrt{3}), \quad (1.1)$$

where  $a = \sqrt{3}d_{CC}$  is the lattice constant, and  $d_{CC} \approx 1.42\text{\AA}$  for the carbon-carbon distance [20, 33, 6]. The unit vectors of the reciprocal lattice are given by

$$\mathbf{b}_1 = \frac{2\pi(\mathbf{a}_2 \times \hat{\mathbf{z}})}{\mathbf{a}_1 \cdot (\mathbf{a}_2 \times \hat{\mathbf{z}})} \quad \mathbf{b}_2 = \frac{2\pi(\hat{\mathbf{z}} \times \mathbf{a}_1)}{\mathbf{a}_2 \cdot (\hat{\mathbf{z}} \times \mathbf{a}_1)}, \quad (1.2)$$

where  $\hat{\mathbf{z}}$  is the unit vector normal to the graphene plane. This leads to

$$\mathbf{b}_1 = \frac{2\pi}{\sqrt{3}a}(\sqrt{3}, 1) \quad \mathbf{b}_2 = \frac{2\pi}{\sqrt{3}a}(-\sqrt{3}, 1). \quad (1.3)$$

The first Brillouin zone is a hexagon (Figure 1.5b), where the corners are called the K points.

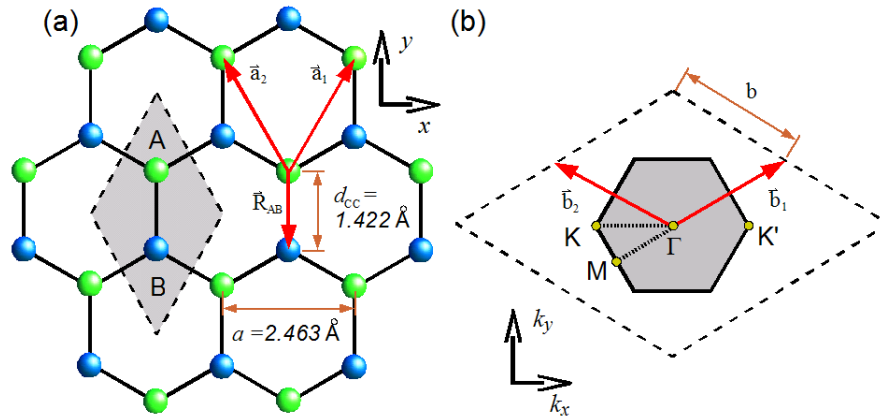


Figure 1.5: The (a) unit cell of graphene is the rhombus shown, and (b) the first Brillouin zone of graphene is the shaded hexagon. Figure taken from [6].

The six corners form two inequivalent groups of K points, usually labeled K and  $K'$  [38].

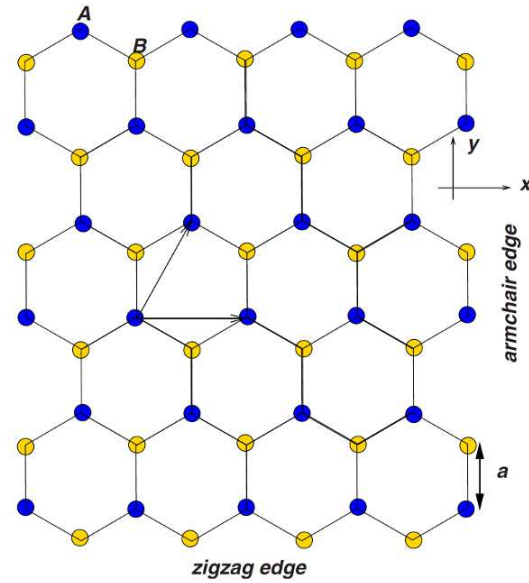


Figure 1.6: Part of a honeycomb lattice showing both zigzag and armchair edges. Figure taken from [33].

There are two edges or boundaries commonly seen in graphene crystallites: the armchair and the zigzag edges [16]. Figure 1.6 shows a honeycomb lattice having zigzag edges along the  $x$  direction and armchair edges along the  $y$  direction. If the graphene nanoribbon is chosen to be infinite in the  $x$  direction but finite in the  $y$  direction, a nanoribbon with zigzag edges is produced; conversely, choosing the nanoribbon to be infinite along the  $y$  but finite in the  $x$  direction, a nanoribbon with armchair edges is produced. It is found experimentally and theoretically [33, 39, 21, 5, 40, 41, 42] that the nature of the graphene nanoribbon edges as zigzag or armchair plays very important role in their physical properties.

This crystallographic description is the basis the calculation of graphene's electronic properties as well as for some analogous magnetic structures described later.



## 1.2 Tight binding model for graphene

The electronic energy of a single electron can be calculated in principle by solving Schrödinger's equation:

$$-\frac{\hbar^2}{2m_e}\nabla^2\Psi(\mathbf{r}) + V(\mathbf{r})\Psi(\mathbf{r}) = E\Psi(\mathbf{r}), \quad (1.4)$$

where  $m_e$  is the mass of the electron. Schrödinger's equation could alternatively be written in the following Dirac notation:

$$\hat{H}|\Psi\rangle = E|\Psi\rangle. \quad (1.5)$$

Here  $\hat{H}$  is the Hamiltonian of the electron, which consists of the particle kinetic energy term  $-(\hbar^2/2m_e)\nabla^2$  and the potential energy term  $V(\mathbf{r})$ . When the electronic Hamiltonian  $\hat{H}$  operates on the wavefunction  $|\Psi\rangle$  of the particle, the total energy of the electron  $E$  is obtained as an eigenvalue [37, 43, 44].

To calculate the energy of the delocalized electrons of  $\pi$  bonds on a 2D honeycomb lattice of graphene, Schrödinger's equation should be solved for all  $\pi$ -bonded electrons of the graphene lattice, not just for a single electron. In this case the potential  $V(\mathbf{r})$  represents the effective potential seen by those electrons in the honeycomb lattice, which mean that the potential has the periodicity and the symmetry for the lattice of graphene. Consequently the total lattice Hamiltonian will have the same periodicity.

The wavefunction of Schrödinger's equation must satisfy Bloch's theorem [38, 37, 43], which states that an eigenfunction  $\Psi$  will satisfy the symmetry property

$$\hat{T}_{\mathbf{a}_i}\Psi = e^{-i\mathbf{q}\cdot\mathbf{a}_i}\Psi, \quad (1.6)$$

where  $\hat{T}_{\mathbf{a}_i}$  is the translation operator along a lattice vector  $\mathbf{a}_i$  and  $\mathbf{q}$  is a wavevector. It is seen that the phase factor is characterized by the wavevector  $\mathbf{q}$  which is the eigenvalue of the momentum operator with  $\mathbf{p} = \hbar\mathbf{q}$ . A function that satisfies Equation (1.6) is called a Bloch function.

An approximation is generally needed to construct the lattice wavefunctions for graphene that satisfy the above requirements. One approach is to consider that the electrons spend most of their time occupying their own lattice atoms and occasionally jump from one atom to another one in the lattice. This approximation is the basis of the *tight binding model* [37, 38, 43], in which every electron is tightly bound to an atom in the graphene lattice and satisfies the following form of Schrödinger's equation:

$$-\frac{\hbar^2}{2m_e}\nabla^2\varphi_n^{A/B}(\mathbf{r}) + U^{A/B}(\mathbf{r})\varphi_n^{A/B} = E_n^{A/B}\varphi_n^{A/B}, \quad (1.7)$$

where  $\varphi_n^{A/B}(\mathbf{r})$  is the normalized  $n$ -th state wavefunction of an A/B isolated atom with  $U^{A/B}(\mathbf{r})$  atomic potential [45, 37, 38].

A linear combination of atomic orbitals, formed from the  $\varphi_n^{A/B}(\mathbf{r})$  wavefunctions, is then used to approximate the required Bloch function  $\Psi_\alpha(\mathbf{q}, \mathbf{r})$  as follows:

$$\Psi_\alpha(\mathbf{q}, \mathbf{r}) = \frac{1}{\sqrt{N}} \sum_{\mathbf{R}_\alpha}^N e^{i\mathbf{q}\cdot\mathbf{R}_\alpha} \varphi_\alpha(\mathbf{r} - \mathbf{R}_\alpha) \quad (\alpha = A, B), \quad (1.8)$$

where  $\mathbf{R}_\alpha$  is the atomic position of allowed lattice vectors,  $\alpha$  is called the pseudospin index, the summation is taken over the set of atomic sites in the A or B sublattice, and  $\varphi_\alpha$  is the atomic wavefunction [38, 45, 6]. It is easy to show that the above function in Equation (1.8) satisfies Bloch's theorem (Equation (1.6)).

Now the above Bloch function will be used to construct the graphene lattice *Bloch wavefunction* [38, 45, 6] as follows

$$\Phi_j(\mathbf{q}, \mathbf{r}) = \sum_{\alpha=1}^N C_{j\alpha} \Psi_{\alpha}(\mathbf{q}, \mathbf{r}), \quad (\alpha = A, B). \quad (1.9)$$

Then the above Bloch wavefunctions can be used in solving Schrödinger's equation to get the energy:

$$\hat{H}|\Phi_j\rangle = \epsilon_j(\mathbf{q})|\Phi_j\rangle, \quad (1.10)$$

where  $\hat{H}$  is the graphene lattice Hamiltonian, and  $\epsilon_j(\mathbf{q})$  is the energy as a function of the wavevector  $\mathbf{q}$ , which is obtained from

$$\epsilon_j(\mathbf{q}) = \frac{\langle \Phi_j | \hat{H} | \Phi_j \rangle}{\langle \Phi_j | \Phi_j \rangle} = \frac{\int \Phi_j^* \hat{H} \Phi_j d\mathbf{r}}{\int \Phi_j^* \Phi_j d\mathbf{r}}. \quad (1.11)$$

Substituting Equation (1.8) into Equation (1.11) yields [38]:

$$\epsilon_j(\mathbf{q}) = \frac{\sum_{\alpha, \alpha'=1}^N C_{j\alpha}^* C_{j\alpha'} \langle \Psi_{\alpha} | \hat{H} | \Psi_{\alpha'} \rangle}{\sum_{\alpha, \alpha'=1}^N C_{j\alpha}^* C_{j\alpha'} \langle \Psi_{\alpha} | \Psi_{\alpha'} \rangle} \equiv \frac{\sum_{\alpha, \alpha'=1}^N C_{j\alpha}^* C_{j\alpha'} \hat{H}_{\alpha\alpha'}}{\sum_{\alpha, \alpha'=1}^N C_{j\alpha}^* C_{j\alpha'} S_{\alpha\alpha'}}, \quad (1.12)$$

where the Hamiltonian matrix elements are given by

$$\hat{H}_{\alpha\alpha'}(\mathbf{q}) = \langle \Psi_{\alpha} | \hat{H} | \Psi_{\alpha'} \rangle = \int \Psi_{\alpha}^* \hat{H} \Psi_{\alpha'} d\mathbf{r}, \quad (1.13)$$

and the overlap integral matrix elements are

$$S_{\alpha\alpha'}(\mathbf{q}) = \langle \Psi_{\alpha} | \Psi_{\alpha'} \rangle = \int \Psi_{\alpha}^* \Psi_{\alpha'} d\mathbf{r}. \quad (1.14)$$

The coefficients  $C_{j\alpha'}$  could be written in terms of the following column matrix

$$C_j = \begin{pmatrix} C_{j1} \\ \vdots \\ C_{jN} \end{pmatrix}. \quad (1.15)$$

Then Schrödinger's Equation (1.10) can be re-expressed as

$$\sum_{\alpha'=1}^N C_{j\alpha'} \hat{H}_{\alpha\alpha'} = \epsilon_j(\mathbf{q}) \sum_{\alpha'=1}^N C_{j\alpha'} S_{\alpha\alpha'}, \quad (1.16)$$

or compactly in matrix form as

$$\hat{H}C_j = \epsilon_j(\mathbf{q})C_jS. \quad (1.17)$$

This matrix equation leads to the following condition [38, 6] for non-trivial solutions:

$$\det[\hat{H} - \epsilon S] = 0. \quad (1.18)$$

This secular equation is an equation of degree  $\alpha$  whose solutions give the eigenvalues  $\epsilon_j(\mathbf{q})$ , which are the energy dispersion relations for the branch  $\alpha$ . This energy dispersion has been plotted in the highly symmetric directions of the first Brillouin zone. [38, 6]

For graphene with its atoms of  $A$  and  $B$  types (see Figure 1.5), this means  $\alpha = 2$ , so the Hamiltonian matrix and overlap integral matrix are both of size  $2 \times 2$ . Equation (1.9) may be substituted into Equations 1.13 and 1.14 to obtain the  $\hat{H}$  and  $S$  matrix elements.

The  $2 \times 2$  matrix Hamiltonian,  $\hat{H}_{\alpha\beta}$ , ( $\alpha, \beta \in A, B$ ) [38, 6] is given as follows:

$$\hat{H}_{\alpha\beta}(\mathbf{r}) = \frac{1}{N} \sum_{\mathbf{R}_\alpha, \mathbf{R}_\beta}^N e^{i\mathbf{q} \cdot (\mathbf{R}_\alpha - \mathbf{R}_\beta)} \langle \varphi_\beta(\mathbf{r} - \mathbf{R}_\beta) | \hat{H} | \varphi_\alpha(\mathbf{r} - \mathbf{R}_\alpha) \rangle. \quad (1.19)$$

When  $\alpha = A$  and  $\beta = B$  we have

$$\hat{H}_{AB}(\mathbf{r}) = \frac{1}{N} \sum_{\mathbf{R}_A, \mathbf{R}_B}^N e^{i\mathbf{q} \cdot (\mathbf{R}_A - \mathbf{R}_B)} \langle \varphi_B(\mathbf{r} - \mathbf{R}_B) | \hat{H} | \varphi_A(\mathbf{r} - \mathbf{R}_A) \rangle, \quad (1.20)$$

where the transfer integral

$$t_0 = \langle \varphi_B(\mathbf{r} - \mathbf{R}_B) | \hat{H} | \varphi_A(\mathbf{r} - \mathbf{R}_A) \rangle \quad (1.21)$$

represents the energy needed for an electron to hop from the site  $A$  to one of its nearest neighbors (NN), which are always  $B$  sites (see Figure 1.5). The values of the vectors  $\mathbf{R}_A - \mathbf{R}_B = \delta_i$  that connect this atom of type  $A$  with its three NN atoms of type  $B$  are substituted into Equation (1.20) to give

$$\hat{H}_{AB}(\mathbf{r}) = t_0 (e^{i\mathbf{q} \cdot \delta_1} + e^{i\mathbf{q} \cdot \delta_2} + e^{i\mathbf{q} \cdot \delta_3}) = t_0 f(\mathbf{q}). \quad (1.22)$$

Since the Hamiltonian  $\hat{H}$  is Hermitian [46, 38, 6], the other off-diagonal matrix element  $\hat{H}_{BA}$  is equal to  $\hat{H}_{AB}^*$ .

When  $\alpha = \beta$  in Equation (1.19), the atomic sites are on the same sublattice. These atomic sites are the next-nearest neighbors (NNNs) with six position vectors from the original site as

follows: the lattice vectors  $\mathbf{a}_1$  and  $\mathbf{a}_2$  along with  $\mathbf{a}_3 = \mathbf{a}_1 - \mathbf{a}_2$ , and their negatives. Substituting these position vectors into the Hamiltonian, we find that the diagonal matrix element  $\hat{H}_{AA}$  are

$$\begin{aligned}\hat{H}_{AA}(\mathbf{r}) &= \frac{1}{N} \sum_{\mathbf{R}_A, \mathbf{R}'_A}^N e^{i\mathbf{q} \cdot (\mathbf{R}_A - \mathbf{R}'_A)} \langle \varphi_A(\mathbf{r} - \mathbf{R}'_A) | \hat{H} | \varphi_A(\mathbf{r} - \mathbf{R}_A) \rangle, \\ &= \epsilon_{2p} + 2t_1(\cos(\mathbf{q} \cdot \mathbf{a}_1) + \cos(\mathbf{q} \cdot \mathbf{a}_2) + \cos(\mathbf{q} \cdot \mathbf{a}_3)) + (\text{more distant terms}),\end{aligned}\quad (1.23)$$

where  $\epsilon_{2p}$  is a characteristic energy of the  $\pi$  bonds between two  $2p_z$  orbitals and  $t_1$  is a NNN hopping energy. From the symmetry between the sublattices in graphene,  $\hat{H}_{BB}$  is equivalent to  $\hat{H}_{AA}$ . Using the deduced values of the Hamiltonian matrix elements and keeping only NN contributions, one obtains

$$\hat{H} = \begin{pmatrix} \epsilon_{2p} & t_0 f(\mathbf{q}) \\ t_0 f^*(\mathbf{q}) & \epsilon_{2p} \end{pmatrix}. \quad (1.24)$$

In a similar manner, using Equation (1.14), the overlap integral matrix  $S$  is

$$S = \begin{pmatrix} 1 & s_0 f(\mathbf{q}) \\ s_0 f^*(\mathbf{q}) & 1 \end{pmatrix}, \quad (1.25)$$

where

$$s_0 = \langle \varphi_B(\mathbf{r} - \mathbf{R}_B) | \varphi_A(\mathbf{r} - \mathbf{R}_A) \rangle. \quad (1.26)$$

Substituting the above matrices  $\hat{H}$  and  $S$  in the NN approximation into the secular Equation (1.18) and solving it, one obtains the following tight-binding model energy dispersion relation

$$\epsilon_{NN}(\mathbf{q}) = \frac{\epsilon_{2p} \pm t_0 |f(\mathbf{q})|}{1 \pm s_0 |f(\mathbf{q})|}, \quad (1.27)$$

where  $|f(\mathbf{q})|$  is calculated using the lattice vectors shown in Figure 1.5 as

$$|f(\mathbf{q})| = \sqrt{1 + 4 \cos\left(\frac{\sqrt{3}q_x a}{2}\right) \cos\left(\frac{q_y a}{2}\right) + \cos^2\left(\frac{q_y a}{2}\right)}. \quad (1.28)$$

Here the (+) signs give the bonding  $\pi$  energy band, and the (-) signs give the anti-bonding  $\pi^*$  band. If the overlap integral  $s_0$  is set to zero, the  $\pi$  and  $\pi^*$  bands become symmetrical around  $E = \epsilon_{2p} = 0$  [47, 38, 6]. The energy dispersion relations are commonly used in this case as a simple approximation (see Figure 1.7) [12, 38, 20]:

$$E_{2D}(q_x, q_y) = \pm t_0 \sqrt{1 + 4 \cos\left(\frac{\sqrt{3}q_x a}{2}\right) \cos\left(\frac{q_y a}{2}\right) + \cos^2\left(\frac{q_y a}{2}\right)} \quad (1.29)$$

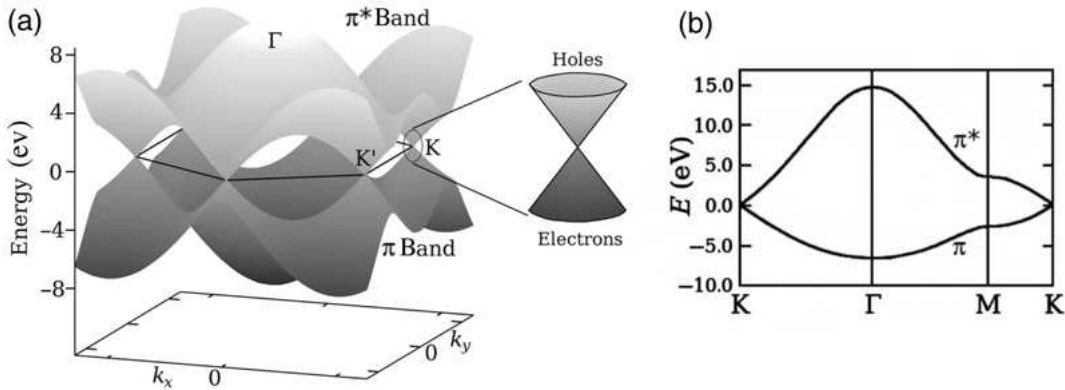


Figure 1.7: Energy dispersion relation for a graphene single layer, drawn in the first Brillouin zone. The energy bands depend only on  $q_x$  and  $q_y$ . The  $\pi$  band is completely filled and meets the totally empty  $\pi^*$  band at the K points. Near these points both bands have a linear dispersion. (b) The dispersion along the high-symmetry points  $\Gamma$ MK. Figure taken from [20].

### 1.2.1 Second quantization form of the Hamiltonian

The tight-binding graphene Hamiltonian in Equation (1.19) describes a hopping between NNs A and B, so that electrons at the site of an atom of the type A/B can hop to any of the three nearest B/A atoms, respectively. The graphene Hamiltonian can be rewritten as follows [45]:

$$\hat{H} = - \sum_{\langle ij \rangle} t_{ij} |\varphi_j^A\rangle \langle \varphi_i^B| + \text{h.c.} \quad (1.30)$$

In the above Hamiltonian an electron leaving an atom site is a particle annihilation event in the language of the second quantization and is represented by an annihilation operator. When an electron moves to a new atom site this is a particle creation event and is represented by a creation operator. Let the operator  $\mathbf{a}_i^\dagger$  create an electron on site  $i$  in the sublattice A, and the operator  $\mathbf{a}_i$  annihilate an electron on site  $i$  in the sublattice A. Also let the operator  $\mathbf{b}_j^\dagger$  create an electron on site  $j$  in the sublattice B, and the operator  $\mathbf{b}_j$  annihilate an electron on site  $j$  in the sublattice B. The graphene Hamiltonian can be written in the following second quantization

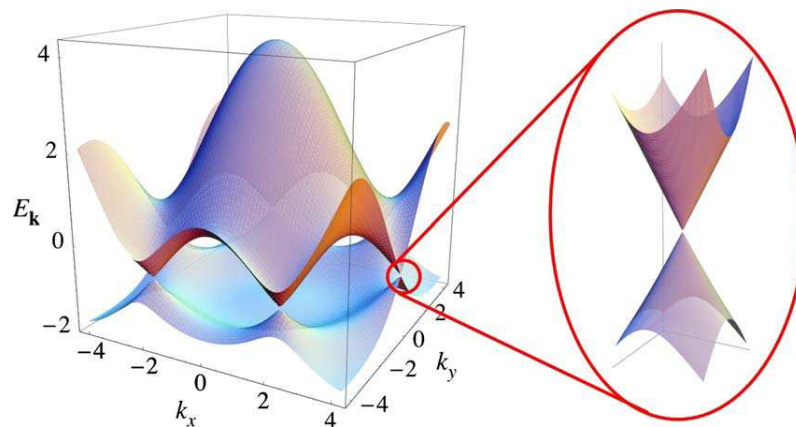


Figure 1.8: Electronic dispersion in the honeycomb lattice (in units of the NN hopping  $t$ ) for finite values of  $t_0$  and  $t_1$ , with  $t_0=2.7$  eV and  $t_1=0.2t$ . Right: zoom in of the energy bands close to one of the Dirac points. Figure taken from [33].



form (using the units with  $\hbar = 1$ ) [46, 48, 45, 20, 33]:

$$\hat{H} = - \sum_{\langle ij \rangle} t_{0ij} (\mathbf{a}_i^\dagger \mathbf{b}_j + \mathbf{h.c.}) + t_{1ij} (\mathbf{a}_i^\dagger \mathbf{a}_j + \mathbf{b}_i^\dagger \mathbf{b}_j + \mathbf{h.c.}). \quad (1.31)$$

Here  $t_{0ij} (\approx 2.8\text{eV})$  is the NN hopping energy given in Equation (1.21), and in graphene it is the hopping energy between different sublattices  $A$  and  $B$ . Also  $t_{1ij} (\approx 0.1\text{eV})$  is the NNN hopping energy which in graphene is the hopping in the same sublattice [33, 49, 47]. Figure 1.8 shows the effect of the  $t_{1ij}$  NNN hopping energy on the electronic energy dispersion in the honeycomb lattice, which includes removing the symmetry around zero energy.

Equation (1.31) will be used through the next chapters for our studies of the effects of impurities on the electronic excitations in graphene nano-ribbons.

### 1.3 Magnetic properties of 2D stripe systems

While pure graphene itself is not a ferromagnetic, there are some interesting formal similarities between theories for graphene ribbons and for ferromagnetic stripes, since both are 2D systems with short-range interactions and their Hamiltonians in second quantization have an analogous form. Therefore it is appropriate to discuss also the topic of ferromagnetic stripes in this thesis. The magnetic properties of 2D stripe systems, especially their spin fluctuations, are very important for example in understanding high temperature superconductors [50, 51, 9, 10, 11, 52, 53], for applications like magnetic storage and switching devices, and for the new promising field of spintronics [54, 55, 56, 57, 58, 59].

The electron spin is an intrinsic angular momentum and an important intrinsic degree of

freedom. It is a fundamental property of an electron like its mass and charge, and experiments show that there are only two allowed projections of the electron spin [44, 60] with the values

$$\pm \frac{1}{2}\hbar. \quad (1.32)$$

The electron spin has an important effect on the electron's wavefunction. Elementary particles with half-integer spin like electrons are called fermions, and they follow the Pauli exclusion principle, which is the quantum mechanical principle that no two identical fermions may occupy the same quantum state simultaneously. This is a basic principle behind understanding the periodic table of chemical elements [44, 60].

The total electron spin angular momentum vector, which is quantized, is calculated using the spin operator  $\hat{S}$ , where  $(\hat{S})^2$  satisfies [60]

$$\hat{S}^2|S m_s\rangle = \hbar^2 S(S + 1)|S m_s\rangle \quad (1.33)$$

and  $S = 1/2$  is the spin quantum number for electrons. The Cartesian components of spin  $\hat{S}_i$  at site  $i$  and spin  $\hat{S}_j$  at site  $j$ , being angular momentum components, obey the following commutation rules

$$[\hat{S}_i^l, \hat{S}_j^m] = i\delta_{ij} \epsilon^{lmn} \hat{S}_j^n, \quad (1.34)$$

where  $l, m, n$  denote Cartesian components,  $\delta_{ij}$  is the Kronecker delta equal to 1 if  $i = j$  and 0 otherwise, and the LeviCivita symbol  $\epsilon^{lmn}$  is 1 if  $(l, m, n)$  is an even permutation of  $(x, y, z)$ , -1 if it is an odd permutation, and 0 if any index is repeated [46, 60].

Related to its spin an electron also has a magnetic dipole moment [60] given by

$$\mu = -\frac{g\mu_B}{\hbar}\mathbf{S}, \quad (1.35)$$

where the spin  $\mathbf{S}$  and magnetic moment  $\mu$  of an electron are antialigned due to the negative charge of the electron. Here  $\mu_B$  is the Bohr magneton, and  $g$  ( $=2$  for a free electron) is called the Landé  $g$ -factor.

To calculate the spin excitations it is usually satisfactory to consider the motion and the charge of the particles as being frozen, and we focus on the spin properties. In this section a discussion of the spin excitations will be given treating for simplicity the 1D case. This will be a preparation for our calculations for 2D systems in chapter 2. The spin excitations can be calculated in principle by solving Schrödinger's Equation (1.7) for the electrons/ions in a spin lattice. Since in this case the motion and the charge of the spin lattice are frozen, the kinetic energy term in Schrödinger's equation will be neglected and the Hamiltonian will be dominated by the potential energy terms for spins interactions in the lattice. Our calculations will be concerned primarily with Heisenberg NN exchange interactions, the Zeeman energy, and the magnetic anisotropy [54, 46, 61, 43, 62], as described below.

### 1.3.1 Heisenberg exchange Hamiltonian

To understand the origin of the exchange interaction in a spin lattice, let us initially consider just two electrons located at neighboring sites in a spin lattice or, for simplicity, a 1D chain. This total two-electron wavefunction may be constructed from the individual electronic wavefunctions, which consist of a spin wavefunction part and an orbital wavefunction part. The

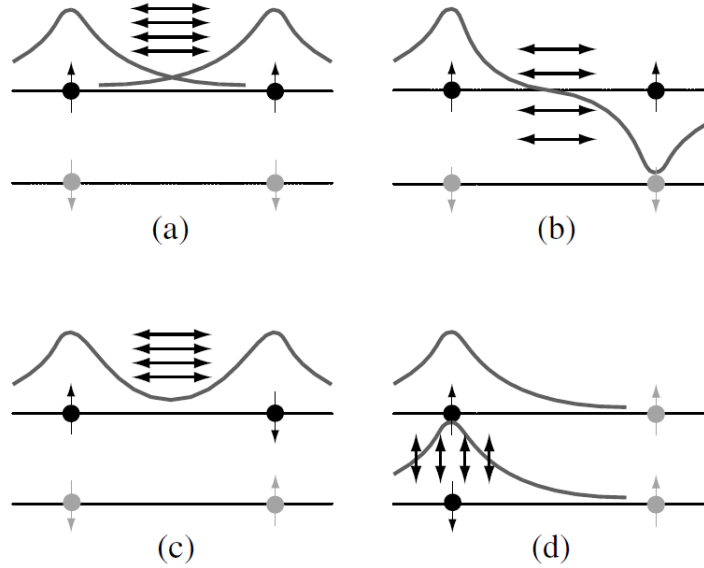


Figure 1.9: Possible configurations due to Coulomb interaction between two electrons at neighboring sites in a spin lattice. The curves show the two-electron wavefunction envelopes: (a) parallel alignment of spins, (b) anti-symmetry of the spatial wave function, (c) anti-parallel spin configurations, (d) Coulomb interaction between electrons with opposite spin populating the same site. Figure taken from [46].

antisymmetric requirement of the Pauli exclusion principle is then satisfied if the antisymmetric orbital wavefunction is multiplied with a symmetric spin wavefunction, or vice versa. The competition between the electrostatic Coulomb repulsion interaction for two electrons in a spin lattice and possible combinations for the ground state (see Figure 1.9) makes the energy of interaction between the two spins  $\mathbf{S}_i$  and  $\mathbf{S}_j$  depend on their relative orientation, which is usually expressed in terms of their dot product. The Hamiltonian of the system is then given by following Heisenberg exchange term:

$$\hat{H}_{\text{Heisenberg}} = -\frac{1}{2} \sum_{i,j} J_{i,j} \mathbf{S}_i \cdot \mathbf{S}_j, \quad (1.36)$$

where  $J_{i,j}$  is known as the exchange coupling constant between the two NN spins at sites  $i$  and  $j$ . The value of  $J_{i,j}$  could be calculated using first principle arguments, but usually its value is

obtained from experiments. Essentially, it depends on the degree of overlap of the electronic wavefunctions, and so is short range. When  $J_{i,j}$  is greater than zero, the spins in the lattice are preferentially aligned parallel which is the ferromagnetic configuration, while when  $J_{i,j}$  is less than zero, the spins in the lattice prefer the antiparallel or antiferromagnetic configuration. The Heisenberg Hamiltonian is formally similar in some respect to the tight binding Hamiltonian, as both are dominated by NN interactions [55, 58, 59, 54, 63].

Since the electron has a magnetic moment  $\mu$  given in Equation 1.35, when it is subject to an external magnetic field  $\mathbf{H}_0$  its potential energy  $U$  due to the field is

$$U = -\mu \cdot H_0. \quad (1.37)$$

The presence of a magnetic field displaces the energy of the electron by an amount proportional to the component of the spin angular momentum in the  $\hat{\mathbf{z}}$  direction along the magnetic field. This is called the Zeeman effect [44], and its contribution to the total Hamiltonian is

$$\hat{H}_{\text{Zeeman}} = -g\mu_B H_0 \sum_i S_i^Z. \quad (1.38)$$

If the orbital of an electron is not spherically symmetric, the energy of the electron state will depend on the direction of the orbital with respect to the surrounding ions in the crystal. The interaction between the spin and orbital magnetic moments will cause the energy of the net moment to depend on its orientation with respect to the axes of the lattice. This orientation-dependent contribution to the total energy is called the magnetocrystalline anisotropy energy [54]. In cases where a single axis corresponds to either a maximum or minimum of potential

energy, the lattice anisotropy is called uniaxial anisotropy. For example, if this axis is in the  $z$  direction, its potential energy contribution to the total Hamiltonian [54] is

$$\hat{H}_{\text{Uniaxial}} = - \sum_i D_i (S_i^Z)^2, \quad (1.39)$$

where  $D_i$  is uniaxial anisotropy term [64]. For  $D_i > 0$  the minimum energy configuration is obtained when the spins are aligned along the  $z$ -axis.

To summarize, the total Hamiltonian for the spin lattice includes the Heisenberg NN exchange term, the Zeeman energy term, and a uniaxial anisotropy term and may be written as follows:

$$\hat{H}_{\text{Total}} = -\frac{1}{2} \sum_{i,j} J_{i,j} \mathbf{S}_i \cdot \mathbf{S}_j - g\mu_B H_0 \sum_i S_i^Z - \sum_i D_i (S_i^Z)^2. \quad (1.40)$$

### 1.3.2 Spin waves in ferromagnets

In the ground state of a simple ferromagnet all the spins will be parallel to each other as the temperature goes to zero. A possible excitation from the ground state, could be just reversing one particular spin. However, the energy cost of reversing one particular spin is high, and so Bloch [65] proposed that excitations could be formed with a much lower energy if all the spins share the reversal. The excitations are small-amplitude oscillations in the relative orientations of spins on the ferromagnetic lattice (see Figure 1.10). At low temperatures  $T \ll T_c$  (where  $T_c$  is the Curie temperature) there is a simplification in which the Hamiltonian can be approximated in terms of quasiparticles called magnons, which are quantized. The following steps show how to get to that approximated Hamiltonian, starting from Equation (1.40), and

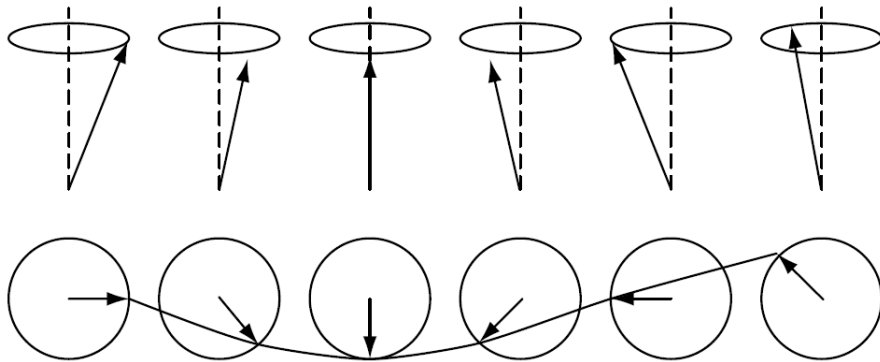


Figure 1.10: Spin-wave excitation (magnon) from the spin ground state of a ferromagnet. Figure taken from [46].

expressing it in terms of spin raising and lowering  $\hat{S}_j^\pm$  operators [44, 60]:

$$\hat{S}_j^\pm = S_j^x \pm iS_j^y \Rightarrow S_j^y = \frac{1}{2i} [\hat{S}_j^+ - \hat{S}_j^-], \quad S_j^x = \frac{1}{2} [\hat{S}_j^+ + \hat{S}_j^-]$$

The dot product  $\mathbf{S}_i \cdot \mathbf{S}_j = (S_i^x S_j^x + S_i^y S_j^y + S_i^z S_j^z)$  can be rewritten in terms of  $\hat{S}_j^\pm$  operators using

$$S_i^x S_j^x + S_i^y S_j^y = \frac{1}{2} (\hat{S}_i^+ \hat{S}_j^- + \hat{S}_i^- \hat{S}_j^+). \quad (1.41)$$

To change the above formulation to one based on second quantization operators [43], we can make use of the Holstein-Primakoff (HP) transformation [66]. This replaces the ladder operators  $\hat{S}_j^\pm$  by creation and annihilation boson operators  $b_j^\dagger$  and  $b_j$  according to

$$\begin{aligned} \hat{S}_j^- &= (2S)^{1/2} b_j^\dagger \left( 1 - \frac{b_j^\dagger b_j}{2S} \right)^{1/2}, \\ \hat{S}_j^+ &= (2S)^{1/2} \left( 1 - \frac{b_j^\dagger b_j}{2S} \right)^{1/2} b_j, \\ \hat{S}_j^Z &= S - b_j^\dagger b_j, \end{aligned} \quad (1.42)$$

where  $b_i^\dagger$  and  $b_j$  obey the usual boson commutation relations:

$$[b_i, b_j^\dagger] = \delta_{ij}, \quad [b_j^\dagger, b_i] = -\delta_{ij}, \quad [b_i, b_j] = [b_j^\dagger, b_i^\dagger] = 0. \quad (1.43)$$

At low temperatures  $T \ll T_c$  the spins are nearly aligned such that  $S^z \sim S$  for each spin, implying that  $b_j^\dagger b_j \ll S$ . This allows us to expand the square roots in the HP transformation as follows:

$$\left(1 - \frac{b_j^\dagger b_j}{2S}\right)^{1/2} \approx 1 - \frac{b_j^\dagger b_j}{4S} + \dots \quad (1.44)$$

If we neglect operator products that are cubic or higher, the simplified form of Equation (1.42) becomes

$$\hat{S}_j^- \approx \sqrt{2S} b_j^\dagger, \quad \hat{S}_j^+ \approx \sqrt{2S} b_j, \quad \hat{S}_j^z = S - b_j^\dagger b_j \quad (1.45)$$

Using the above approximation and doing some algebra, the Hamiltonian in Equation (1.24) becomes approximately

$$\begin{aligned} \hat{H} = & S^2 \left( -\frac{1}{2} \sum_{i,j} J_{i,j} - \sum_i D_i \right) - g\mu_B H_0 \sum_i S - \frac{1}{2} S \sum_{i,j} J_{i,j} (b_i b_j^\dagger + b_i^\dagger b_j - b_j^\dagger b_j - b_i^\dagger b_i) \\ & + \sum_i [g\mu_B H_0 + (2S - 1)D_i] b_i^\dagger b_i. \end{aligned}$$

The result can be rewritten in the form

$$\hat{H}_{\text{Total}} = E_0 + \hat{H}_s \quad (1.46)$$



where  $E_0$  is the energy of the ground state for the ferromagnetic system given by

$$E_0 = S^2 \left( -\frac{1}{2} \sum_{i,j} J_{i,j} - \sum_i D_i \right) - g\mu_B H_0 \sum_i S, \quad (1.47)$$

and  $\hat{H}_s$  has the following operator form:

$$\hat{H}_s = -\frac{1}{2} S \sum_{i,j} J_{i,j} (b_i b_j^\dagger + b_i^\dagger b_j - b_j^\dagger b_i - b_i^\dagger b_i) + \sum_i [g\mu_B H_0 + (2S - 1)D_i] b_i^\dagger b_i. \quad (1.48)$$

Equation (1.48) mixes terms at different sites  $i$  and  $j$ , and usually it is convenient to make a

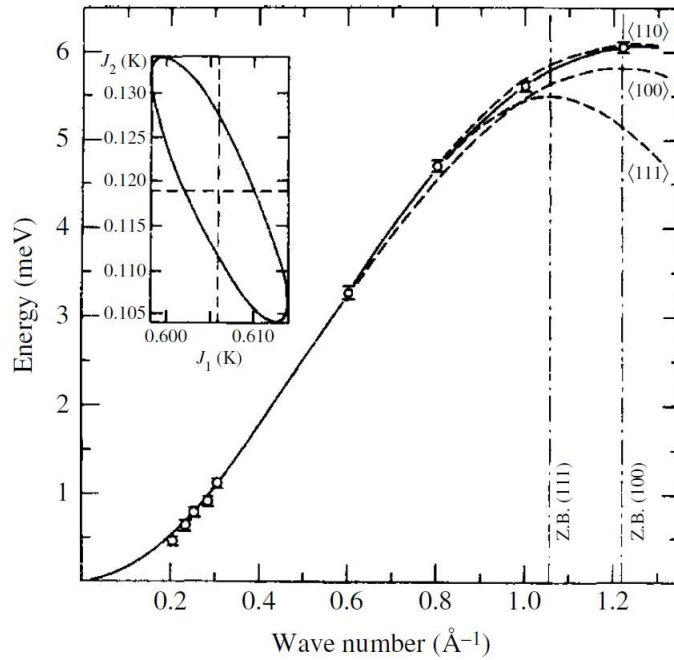


Figure 1.11: Spin-wave spectrum of europium oxide as measured by inelastic neutron scattering at a reference temperature of 5.5 K. Figure taken from [67].

transformation to diagonalize the Hamiltonian. The basis states that diagonalize this Hamiltonian should involve collective excitations of all the spins. A Fourier transformation for the operators to a wavevector representation can be used to transform the above Hamiltonian to

the collective excitations [54, 46, 61, 43, 62]. Let us introduce the operators  $b_{\mathbf{q}}$  and  $b_{\mathbf{q}}^\dagger$  which annihilate and create magnons of wavevector  $\mathbf{q}$ , respectively:

$$\begin{aligned} b_{\mathbf{q}} &= \frac{1}{\sqrt{N}} \sum_j e^{i\mathbf{q}\cdot\mathbf{r}_j} b_j, \\ b_{\mathbf{q}}^\dagger &= \frac{1}{\sqrt{N}} \sum_j e^{-i\mathbf{q}\cdot\mathbf{r}_j} b_j^\dagger, \end{aligned} \quad (1.49)$$

and we define the exchange sum:

$$\gamma_k = \frac{1}{\nu} \sum_{\langle ij \rangle} J_{i,j} e^{i\mathbf{q}\cdot(\mathbf{r}_i - \mathbf{r}_j)}. \quad (1.50)$$

Here  $N$  is the total number of magnetic sites in the lattice, and  $\mathbf{r}_i$  is the position vector of any magnetic site  $i$ . The sum for the exchange terms  $J_{i,j}$  is taken to be over all  $\nu$  NNs in the lattice. With these transformations and ignoring the higher order terms, the diagonalized Hamiltonian eventually takes the form

$$\hat{H}_{\text{Total}} = E_0 + \sum_{\mathbf{q}} \hbar\omega(\mathbf{q}) b_{\mathbf{q}}^\dagger b_{\mathbf{q}}, \quad (1.51)$$

where  $\omega(\mathbf{q})$  is the frequency of the spin wave (magnon), and it depends on the structure of the spin lattice, as well as on the strength of the applied external magnetic field  $H_0$  (see Figure 1.11). Examples will be given later. In the above text  $b_{\mathbf{q}}^\dagger b_{\mathbf{q}}$  is interpreted as the boson number operator for magnons [54, 46, 61, 43, 62].

Equation (1.48) will be used through the next chapters for our studies of the effect of impurities on the spin wave excitations of 2D magnetic stripe systems. By comparing the tight-binding Hamiltonian (1.31) for graphene, and the magnetic Hamiltonian (1.48), it is seen that both Hamiltonians contains only quadratic products of fermion or boson operators, respec-

tively.

Due to this formal similarity, the magnetic 2D stripes and graphene 2D nanoribbons can be usefully studied in the same context and by similar mathematical techniques, as will be clear from this thesis.

## 1.4 Thesis outline

The motivation for this thesis is to investigate the effects of the 2D lattice structures, the range of the interaction (NN and NNN), the presence of impurities, and the formation of bilayer systems. This is carried out for the electronic and the magnetic excitations in 2D materials represented by zigzag and armchair graphene nanoribbons and ferromagnetic stripes.

The method used throughout this thesis is a microscopic theory based on the above second quantization forms for both the tight-binding Hamiltonian (1.31) for graphene and the Heisenberg Hamiltonian (1.48) for magnetic systems, but taking into account the spatial quantization effects arising due to the finite ribbon (stripe) width.

In chapter 2 the theoretical calculations are presented using the above Heisenberg Hamiltonian (1.48) to study the allowed area and edge spin waves for a 2D ferromagnetic square lattice stripe. In particular, a clear distinction is made between area and edge spin wave modes. The corresponding frequencies are derived and the effects of the stripe width on them are studied with the help of the tridiagonal matrix method.

Next, in chapter 3 the second quantization form of the same Heisenberg Hamiltonian (1.48) is used to study the allowed spin waves in a ferromagnetic stripe with a more complicated lattice structure. This is for a 2D honeycomb lattice (like in graphene) which could be grown

artificially in terms of an array of magnetic nanodots. A modified matrix technique is employed in which an interaction matrix for the finite-width stripe is formed and then diagonalized to obtain the spin wave frequencies from the eigenvalues. The cases of armchair and zigzag edges are included, and the method is used to study the effects of the edge exchange, the edge uniaxial anisotropy, and impurities on the allowed spin waves.

In chapter 4 the tight-binding Hamiltonian (1.31) for graphene, along with the tridiagonal matrix method, is used to investigate the properties of area and edge modes for a semi-infinite zigzag honeycomb sheet. This, together with a thorough analysis of the density-of-states effects, allows us to study for first time the effect of edge and impurity parameters (both separately and in combination) on the localized states of a semi-infinite zigzag honeycomb sheet of graphene.

In chapter 5 the tight-binding Hamiltonian (1.31) for graphene is used to study the effect of introducing NNN hopping on the 2D dispersion relations. The obtained results are applied to armchair and zigzag graphene nanoribbons, as well as being compared briefly to magnetic 2D square lattice stripes.

In chapter 6 the tight-binding Hamiltonian (1.31) and the previous theoretical techniques are extended to study bilayer systems by taking AA-stacking bilayer graphene nanoribbons. The obtained results are applied to armchair and zigzag AA-stacking bilayer graphenes nanoribbons. Impurity effects are included, as well as a brief comparison with magnetic 2D square lattice bilayer stripes.

Finally, in chapter 7 we present the conclusions and we make some suggestions for future work.

# Chapter 2

## Spin Waves in Ferromagnetic Stripes

### 2.1 Introduction

Spin waves in 2D magnetic systems are very interesting both experimentally [68, 69, 70, 71, 72] and theoretically [73, 74, 75, 76, 77, 78, 79]. For example, these systems are relevant to our understanding of high temperature superconductors [50, 51, 9, 10, 11, 52, 53], and are the basis of many technological applications of ultrathin ferromagnetic films (e.g., magnetic memory and storage devices, switches, giant magnetoresistance, etc). In addition, 2D spin waves are important in the new promising fields of spintronics mentioned in Chapter 1 and magnonics (see [54, 55, 56, 57, 58, 59, 80]).

Many theoretical techniques have been used to study spin waves (SWs) in 2D and 3D Heisenberg magnets [76]. Some examples are the Holstein-Primakoff (HP) method using boson operators as already introduced in Chapter 1, the “boson mean-field theory” [73, 74] where Schwinger bosons are used to represent the spin operators, and the “modified spin-wave theory” [77] where the Dyson-Maleev transformation is used to represent the spin operators. Additionally, the semi-classical approaches [61, 62] are widely employed for SWs at long wavelengths (or small wavevectors). In recent years, ultra-thin magnetic nanostructures have been fabri-

cated and studied extensively [63, 55, 81, 82, 83], for their SW dynamics. It is often useful to distinguish between the propagating SW modes and the localized SW modes. In a film geometry these are usually referred to as "volume" (or "bulk") modes and "surface" modes respectively. Thus, new theoretical studies are needed where the surfaces (and/or interfaces) are important and where the localized SW modes are considered in detail.

In this chapter our aim is to study SW modes at low temperatures (compared to the Curie temperature  $T_c$ ). We do this for ultra-thin ferromagnets with typically one atom thickness, specifically a 2D stripe with a finite number of atomic rows (a nanoribbon). We employ the Heisenberg model discussed in Chapter 1 and initially assume, for simplicity, a square lattice. We study both the "area" SWs (that propagate across the stripe width) and localized "edge" SWs. This work is very interesting for its expected novel fundamental physics and promising application in magnetic devices.

An operator equation-of-motion technique known as the tridiagonal matrix method [84, 85, 86, 87] will be conveniently employed here to calculate the SW spectra and, in particular, to distinguish between the edge modes and area modes of the ferromagnetic square lattice nanoribbons. The results of the tridiagonal matrix method will also be supplemented and compared with the results obtained by a so-called direct diagonalization method discussed in more detail in next chapter. We assume a total Hamiltonian as introduced in Equation (1.40) in Chapter 1.

## 2.2 Theoretical model

The system initially under study is a 2D Heisenberg ferromagnetic stripe (or nanoribbon) in the  $xy$ -plane. We assume a square lattice with lattice constant  $a$  and we take the average spin alignment of the magnetic sites to be in the  $z$  direction, which is also the direction of the applied magnetic field. The nanoribbon is of finite width in the  $y$  direction with  $N$  atomic rows (labeled as  $n = 1, \dots, N$ ) and it is infinite in the  $x$  direction ( $-\infty \leftrightarrow \infty$ ). The position vector for each site is given by  $\mathbf{r} = a(m, n, 0)$ , where  $m$  is an integer from  $-\infty$  to  $\infty$ , and  $n$  is the row number with  $n = 1, 2, \dots, N$  (see Figure 2.1).

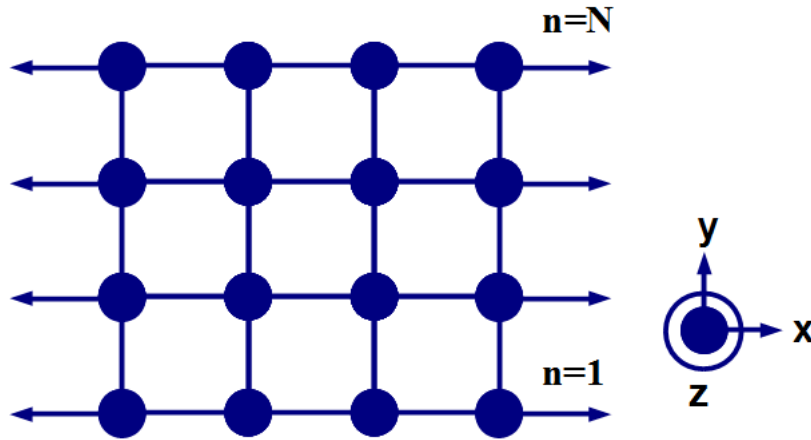


Figure 2.1: Geometry of a 2D Heisenberg ferromagnetic square lattice nanoribbon. The spins are in the  $xy$ -plane and the average spin alignment is in the  $z$  direction. The nanoribbon is finite in the  $y$  direction with  $N$  atomic rows ( $n = 1, \dots, N$ ).

The total Hamiltonian of the system is given by Equation (1.40) and we continue to employ the same notation. The first term is the Heisenberg NN exchange term, the second term is the Zeeman energy term due to an applied field  $H_0$ , and the third term represents the uniaxial anisotropy. The summations over  $i$  and  $j$  run over all the sites, where the NN exchange  $J_{ij}$  has the “bulk” value  $J$  when either  $i$  and  $j$  are in the interior of the nanoribbon, and a modified value  $J_e$  when  $i$  and  $j$  are both at the edge of the nanoribbon (i.e., in row  $n = 1$  or  $n = N$ ).

Similarly, for the uniaxial anisotropy term, we assume a value  $D$  when the site  $i$  is inside the nanoribbon, and a modified value  $D_e$  for sites at the edge of the nanoribbon.

To calculate the SWs for this system at low temperatures  $T \ll T_c$  where the spins are well aligned such that the thermal average of  $S^z \simeq S$  for each spin, we use the Holstein-Primakoff (HP) transformation and follow similar procedures to Chapter 1 to express the total Hamiltonian in terms of boson operators. We arrive at a similar expression to Equation (1.46), where the constant term  $E_0$  is the energy of the ground state for the ferromagnetic system given by Equation (1.47) and the operator term  $\hat{H}_s$  has the following quadratic form

$$\hat{H}_s = -\frac{1}{2}S \sum_{i,j} J_{i,j} (b_i b_j^\dagger + b_i^\dagger b_j - b_j^\dagger b_j - b_i^\dagger b_i) + \sum_i [g\mu_B H_0 + (2S - 1)D_i] b_i^\dagger b_i \quad (2.1)$$

where  $b_j^\dagger$  and  $b_j$  are the creation and the annihilation boson operators.

In order to diagonalize  $\hat{H}_s$  and obtain the SW frequencies, we may consider the time evolution of the creation and the annihilation operators  $b_j^\dagger$  and  $b_j$ , as calculated in the Heisenberg picture in quantum mechanics. In this case, the equation of motion [44, 60, 37, 43, 48] (using units with  $\hbar = 1$ ) for the annihilation operator  $b_j$  is

$$\begin{aligned} \frac{db_j(t)}{dt} &= i [H, b_j(t)] \\ &= (g\mu_B H_0 + (2S - 1)D_j) b_j(t) - \frac{1}{2}S \sum_{i,j} J_{i,j} (b_i(t) - b_j(t)) \end{aligned} \quad (2.2)$$

where the commutation relation between  $b_i^\dagger$  and  $b_j$  in Equation (1.43) was used, as well as the operator identity  $[AB, C] = A[B, C] + [A, C]B$ .

The equation of motion for the creation operator  $b_j^\dagger$  is easily obtained by taking the Hermi-



tion conjugation of Equation (2.2), giving

$$i \frac{db_j^\dagger(t)}{dt} = -(g\mu_B H_0 + (2S - 1)D_j)b_j^\dagger(t) + \frac{1}{2}S \sum_{i,j} J_{i,j} (b_i^\dagger(t) - b_j^\dagger(t)). \quad (2.3)$$

The dispersion relations of the SWs (i.e., the energy or frequency versus wavevector) can now be obtained by solving the above operator equations of motion. The SW energy is related to the SW frequency using  $E = \hbar\omega$ , and a Fourier transform for the operators from the time representation to the frequency representation is made:

$$\begin{aligned} b_j(x, t) &= \int_{-\infty}^{\infty} b_j(x, \omega) e^{-i\omega t} d\omega, \\ b_j^\dagger(x, t) &= \int_{-\infty}^{\infty} b_j^\dagger(x, \omega) e^{-i\omega t} d\omega. \end{aligned} \quad (2.4)$$

On substituting Equation (2.4) in Equations 2.2 and 2.3, we get

$$\begin{aligned} \left( \omega - (g\mu_B H_0 + (2S - 1)D_j) - \frac{1}{2}S \sum_i J_{i,j} \right) b_j(\omega) + \frac{1}{2}S \sum_i J_{i,j} b_i(\omega) &= 0, \\ \left( \omega + (g\mu_B H_0 + (2S - 1)D_j) + \frac{1}{2}S \sum_i J_{i,j} \right) b_j^\dagger(\omega) - \frac{1}{2}S \sum_i J_{i,j} b_i^\dagger(\omega) &= 0. \end{aligned} \quad (2.5)$$

Since the nanoribbon extends to  $\pm\infty$  in the  $x$  direction, we may introduce a 1D Fourier transform to wavevector  $q_x$  along the  $x$  direction for the boson operators  $b_j^\dagger$  and  $b_j$  as follows:

$$\begin{aligned} b_j(x, \omega) &= \frac{1}{\sqrt{N_0}} \sum_{q_x} b_n(q_x, \omega) e^{iq_x m a}, \\ b_j^\dagger(x, \omega) &= \frac{1}{\sqrt{N_0}} \sum_{q'_x} b_n^\dagger(q'_x, \omega) e^{iq'_x m' a}, \end{aligned} \quad (2.6)$$

where  $N_0$  is the (macroscopically large) number of spin sites in any row. The transformed

operators obey the following commutation relations:

$$\left[ b_n(q_x, \omega), b_n^\dagger(q'_x, \omega) \right] = \delta_{q_x q'_x}. \quad (2.7)$$

By substituting Equation (2.6) into Equation (2.5) and rewriting the summations, we get the following set of coupled equations:

$$\begin{aligned} & \left( \omega - (g\mu_B H_0 + (2S - 1)D_s) - \frac{1}{2}S(2J_e + J) + \frac{1}{2}S J_e \gamma(q_x) \right) b_N(q_x, \omega) \\ & \quad + \frac{1}{2}S J b_{N-1}(q_x, \omega) = 0 \quad \text{for } n = N \\ & \left( \omega - (g\mu_B H_0 + (2S - 1)D) - \frac{1}{2}S(4J) + \frac{1}{2}S J \gamma(q_x) \right) b_n(q_x, \omega) \\ & \quad + \frac{1}{2}S J (b_{n+1}(q_x, \omega) + b_{n-1}(q_x, \omega)) = 0 \quad \text{for } N > n > 1 \\ & \left( \omega - (g\mu_B H_0 + (2S - 1)D_{s'}) - \frac{1}{2}S(2J_{s'} + J) + \frac{1}{2}S J_{s'} \gamma(q_x) \right) b_1(q_x, \omega) \\ & \quad + \frac{1}{2}S J b_2(q_x, \omega) = 0 \quad \text{for } n = 1. \end{aligned} \quad (2.8)$$

The first and the third equations refer to the edges  $n = N$  and  $n = 1$  for the nanoribbon system, and we have defined  $\gamma(q_x) = 2 \cos(q_x a)$ . Similar results can be found for the equations involving the creation operator  $b_j^\dagger$ .

The above coupled equations can conveniently be written in matrix form as

$$\begin{aligned} (-\Omega I + A)b &= 0, \\ (\Omega I + A)b^\dagger &= 0, \end{aligned} \quad (2.9)$$

where  $b$  and  $b^\dagger$  are  $N \times 1$  column matrices whose elements are the boson operators  $b_n(q_x, \omega)$



$$A' = \begin{pmatrix} a'_s & -1 & 0 & 0 & \cdots & & & \\ -1 & a' & -1 & 0 & \cdots & & & \\ 0 & -1 & a' & -1 & \cdots & & & \\ \vdots & \vdots & \vdots & \vdots & & \cdots & \cdots & \cdots \\ & & & & & \cdots & a' & -1 & 0 \\ & & & & & \cdots & -1 & a' & -1 \\ & & & & & \cdots & 0 & -1 & a'_s \end{pmatrix}, \quad (2.12)$$

where

$$a'_s = \frac{-\omega + 2(g\mu_B H_0 + (2S - 1)D_e) - S(2J_e + J) + S J_e \gamma(q_x)}{S J},$$

$$a' = \frac{-\omega + 2(g\mu_B H_0 + (2S - 1)D) - S(4J) + S J \gamma(q_x)}{S J}. \quad (2.13)$$

The new tridiagonal matrix  $A'$  may be separated into two terms, following the approach in [87, 86, 88], as

$$A' = A_0 + \Delta, \quad (2.14)$$

where

$$A_0 = \begin{pmatrix} a' & -1 & 0 & 0 & \cdots & & & & \\ -1 & a' & -1 & 0 & \cdots & & & & \\ 0 & -1 & a' & -1 & \cdots & & & & \\ \vdots & \vdots & \vdots & \vdots & & \cdots & \cdots & \cdots & \\ & & & & & \cdots & a' & -1 & 0 \\ & & & & & \cdots & -1 & a' & -1 \\ & & & & & \cdots & 0 & -1 & a' \end{pmatrix}, \quad (2.15)$$

$$\Delta = \begin{pmatrix} \Delta & 0 & 0 & 0 & \cdots & & & & \\ 0 & 0 & 0 & 0 & \cdots & & & & \\ 0 & 0 & 0 & 0 & \cdots & & & & \\ \vdots & \vdots & \vdots & \vdots & & \cdots & \cdots & \cdots & \\ & & & & & \cdots & 0 & 0 & 0 \\ & & & & & \cdots & 0 & 0 & 0 \\ & & & & & \cdots & 0 & 0 & \Delta \end{pmatrix}, \quad (2.16)$$

and the element  $\Delta = a'_s - a'$ . In this way all the edge properties have been separated into the matrix  $\Delta$ . The inverse of a finite-dimensional tridiagonal matrix with constant diagonal elements such as  $A_0$  is well known [85, 87] and can be expressed as

$$(A_0^{-1})_{ij} = \frac{x^{i+j} - x^{|i-j|} + x^{2N+2-(i+j)} - x^{2N+2-|i-j|}}{(1 - x^{2N+2})(x - x^{-1})}. \quad (2.17)$$

Here  $x$  is a complex variable defined such that  $|x| \leq 1$  and  $x + x^{-1} = a'$ .

On noting that  $A' = (A_0 + \Delta) = A_0(1 + A_0^{-1}\Delta)$ , the dispersion relations are obtained by the

condition [62, 88] that  $\det A' = 0$ , which implies

$$\det(I + A_0^{-1}\Delta) = 0. \quad (2.18)$$

Using the previous equations, the matrix  $M = (I + A_0^{-1}\Delta)$  can next be written in a partitioned form [89]:

$$M = \left( \begin{array}{c|c|c} M_{1,1} & 0 & M_{1,N} \\ \hline M_{2,1} & & M_{2,N} \\ \vdots & I & \vdots \\ \hline M_{N-1,1} & & M_{N-1,N} \\ \hline M_{N,1} & 0 & M_{N,N} \end{array} \right), \quad (2.19)$$

where the nonzero elements of  $M$  can be written as

$$M_{i,j} = \delta_{i,j} + \delta_{1,j}(A_0^{-1})_{1,j}\Delta + \delta_{N,j}(A_0^{-1})_{i,N}\Delta, \quad (2.20)$$

and the determinant of  $M$ , which is required for Equation (2.18), can be calculated to give

$$\begin{aligned} \det(M) &= (M_{1,1})^2 - (M_{1,N})^2 \\ &= \left( 1 + \frac{x^2 + x^{2N} - x^{2N+2} - 1}{(1 - x^{2N+2})(x - x^{-1})} \Delta \right)^2 \\ &\quad - \left( \frac{2x^{N+1} - x^{N-1} - x^{N+3}}{(1 - x^{2N+2})(x - x^{-1})} \Delta \right)^2. \end{aligned} \quad (2.21)$$

After some more algebraic steps the condition for  $\det(M) = 0$  can be factorized as two terms

and then written as

$$\begin{aligned} & \left[ (1 - x^{2N+2})(x - x^{-1}) + (x^2 + x^{2N} - x^{2N+2} - 1)\Delta \right] \\ & + \eta(2x^{N+1} - x^{N-1} - x^{N+3})\Delta = 0, \end{aligned} \quad (2.22)$$

where  $\eta = \pm 1$ . This result is formally similar to an expression obtained in the study of finite thickness ferromagnetic slabs [85]. Also, it follows by analogy with previous work [86, 85] that the solutions with  $|x| = 1$  correspond here to the area modes (those propagating across the width of the stripe) while those with  $|x| < 1$  correspond in the present context to the localized edge modes, if any exist.

Before presenting a general analysis of Equation (2.22) for the SW frequencies in Section 2.3, we next examine some special cases.

### 2.2.1 Special case of $N \rightarrow \infty$

It is of interest to study the behavior of the model in the special case when the ribbon (or stripe) becomes very wide. This is the limit of  $N \rightarrow \infty$  in Equation (2.22). Since  $|x| < 1$  for edge modes, the terms of order  $x^N \rightarrow 0$  as  $N \rightarrow \infty$ , giving for these modes

$$(1 + x\Delta) = 0 \quad \Rightarrow \quad x = -\frac{1}{\Delta}. \quad (2.23)$$

This is the same formal expression as obtained in the case of a semi-infinite Heisenberg ferromagnet [86, 85] when  $N \rightarrow \infty$ .

For the edge mode localization condition  $|x| < 1$  to be satisfied in this special case, Equation 2.23 implies  $|\Delta| > 1$ , which gives two possibilities. The first one is  $\Delta > 1$  and the second one

is  $\Delta < -1$ . From the definitions of  $a'_s$  and  $a'$  we have

$$\Delta = \frac{2(2S - 1)(D_e - D) - S(2J_e - 3J) + S(J_e - J)\gamma(q_x)}{SJ},$$

which depends on the physical parameters  $D_e$ ,  $D$ ,  $S$ ,  $J_e$  and  $J$  of the ferromagnetic stripe and on the wavevector component  $q_x$ . Since  $\gamma(q_x) = 2 \cos(q_x a)$  has its maximum when  $\cos(q_x a) = 1$  and its minimum when  $\cos(q_x a) = -1$ , it follows that the minimum value  $\Delta_{min}$  and the maximum value  $\Delta_{max}$  for  $\Delta$  correspond to

$$\Delta_{max/min} = \frac{2(2S - 1)(D_e - D) - S(2J_e - 3J) \pm 2S(J_e - J)}{SJ}$$

In simple cases we might have  $D_e = D$ , i.e., the edge perturbation to the anisotropy is negligible. Then, denoting the ratio between the edge exchange and area exchange by  $r = J_e/J > 0$ , we have

$$\Delta_{max} = 1 \quad \Delta_{min} = -4r + 5.$$

The two cases  $\Delta > 1$  and  $\Delta < -1$  give the following ranges for  $r$ :

$$r < \frac{5}{4} \quad r > \frac{6}{4}. \quad (2.24)$$

These are the ranges of the ratio exchange  $r = J_e/J$  for which the edge modes exist at some  $q_x$  value in this special case ( $N \rightarrow \infty$ ) for the square lattice.

The conditions are modified if edge perturbations in the anisotropy are included.



### 2.2.2 Case of large finite $N$

Another interesting case is when  $N$  becomes sufficiently large that the two solution  $x^+$  and  $x^-$  for  $\eta = \pm 1$  of Equations (2.22) can be obtained by an iterative approach used in reference [85]. Since  $|x| < 1$  for edge modes, all terms of order  $x^N$  in Equations (2.22) are small for sufficiently large  $N$  and the two solution  $x^+$  and  $x^-$  become closer to the solution  $x_0 = -\Delta^{-1}$  for the special case of  $N \rightarrow \infty$ .

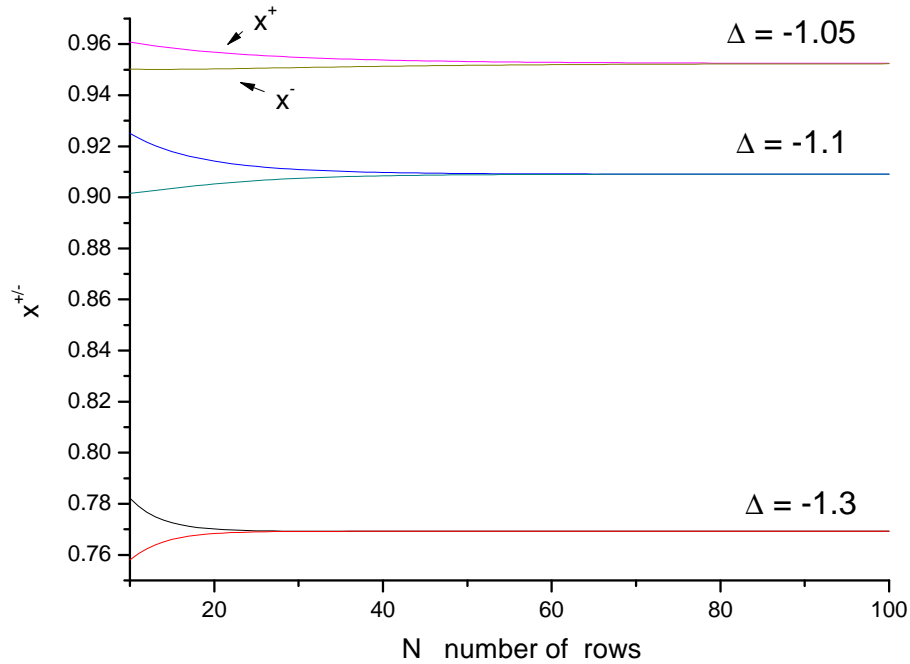


Figure 2.2: Calculated values of  $x^+$  and  $x^-$  for several values of  $\Delta < -1$  and for  $N$  from 10 to 100.

To use a first order iteration for Equations (2.22) we must rewrite them in the forms  $x^\pm = F^\pm(x_0)$ , which leads to the following two approximate solutions

$$x^\pm = \frac{-1}{x_{ap/am}}. \quad (2.25)$$

Here  $x_{ap}$  is equal to

$$x_0^{2N+3} + \Delta x_0^{2N+2} - x_0^{2N+1} - \Delta x_0^{2N} + \Delta x_0^{N+3} - 2\Delta x_0^{N+1} + \Delta x_0^{N-1} + \Delta$$

and  $x_{am}$  is equal to

$$x_0^{2N+3} + \Delta x_0^{2N+2} - x_0^{2N+1} - \Delta x_0^{2N} - \Delta x_0^{N+3} + 2\Delta x_0^{N+1} - \Delta x_0^{N-1} + \Delta.$$

This approximation is valid provided  $|\Delta| > 1$ . Figure 2.2 shows the calculated values of  $x^+$  and  $x^-$  using illustrative values of  $\Delta$  chosen as  $-1.05$ ,  $-1.1$  and  $-1.3$  when  $N$  has values from 10 to 100. The iterative approach is found to work well for  $N > 10$  in this case. Also the convergence to the infinite  $N$  limit is seen.

## 2.3 Numerical calculations

More generally, the dispersion relations can be obtained by solving Equation (2.22) using a numerical calculation for any finite  $N$ . The number of rows  $N$  and the value of  $\Delta$  are first substituted in the Equations (2.22), and then the polynomial equations are solved for  $x$  which can be used to obtain the dispersion relations. Since the solutions for  $x$  may have complex roots, one of the ways to solve such equations is to use Laguerre's method for finding the

roots[90, 91] of polynomials. By rearranging Equations (2.22) we have:

First polynomial

$$\begin{aligned} x^{2N+4} + \Delta x^{2N+3} - x^{2N+2} - \Delta x^{2N+1} - \Delta x^{N+4} + 2\Delta x^{N+2} - \Delta x^N \\ - \Delta x^3 - x^2 + \Delta x + 1 = 0 \end{aligned} \quad (2.26)$$

Second polynomial

$$\begin{aligned} x^{2N+4} + \Delta x^{2N+3} - x^{2N+2} - \Delta x^{2N+1} + \Delta x^{N+4} - 2\Delta x^{N+2} + \Delta x^N \\ - \Delta x^3 - x^2 + \Delta x + 1 = 0 \end{aligned} \quad (2.27)$$

Both polynomials are of degree  $2N + 4$ , and they are applicable for all  $N$  equal to 3 and above. We note that there is a special case when  $N = 3$ , since the two power indices  $2N + 1$  and  $N + 4$  become equal to 7. The obtained values for  $x$  must satisfy the conditions for physical SW modes as mentioned earlier. The edge SW modes are localized on one of the edges and their amplitudes decay exponentially inside the nanoribbon. This requires that  $x$  must be real and have magnitude less than 1 for edge modes. The area modes are oscillating waves with distance inside the nanoribbon, and so

$$\begin{aligned} x \in R \text{ and } |x| < 1 \text{ for edge modes} \\ x = e^{iq_y m} \text{ and } |x| \leq 1 \text{ for area modes} \end{aligned} \quad (2.28)$$

In the previous section the ranges of  $r$  values of edge modes to exist were obtained algebraically for the special cases  $N \rightarrow \infty$  and large  $N$ . We can use numerical calculations to obtain the ranges of  $\Delta$  for smaller  $N$  that satisfies the conditions for which both edge modes

and area modes exist. For that purpose, a Fortran program was written with the algorithm described in Appendix A.1 to solve the two polynomials using Laguerre's method where two subroutines `zroots` and `laguer` are adapted from [90]. The values for minimum positive (P) and maximum negative (N) of  $\Delta$  for even (E) and odd (O) rows number  $N$  that satisfy (2.28) are computed from the first polynomial (F) (2.26) and from the second polynomial (S) (2.27). It is mainly relevant to do this for the edge modes, since their localization depends sensitively on  $\Delta$ .

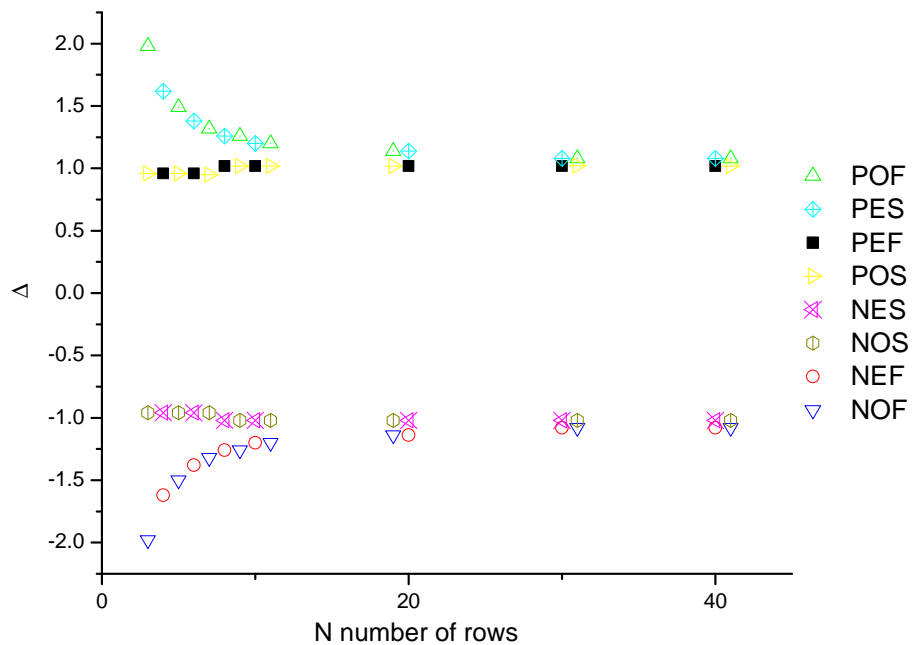


Figure 2.3: The values for minimum positive (P) and maximum negative (N) of  $\Delta$  for even (E) and odd (O) number  $N$  that satisfy the edge modes condition (2.28), are computed from the first polynomial (F) (2.26) and from the second polynomial (S) (2.27).

Figure 2.3 shows the behavior of the minimum positive value for  $\Delta$  that satisfies the conditions (2.28) for the existence of edge modes. It is clear from the figure that, in the range of  $N \leq 20$ , the minimum positive values for odd  $N$  for the polynomial (2.26) and for even  $N$  for the second polynomial (2.27) are approximately the same and they exponentially decay to a nearly constant value of 1.02. In the same range of  $N$ , the minimum positive values for even  $N$  for the

first polynomial (2.26) and for odd  $N$  for the second polynomial (2.27) are nearly constant and equal to 0.95. After  $N$  equal to 20, the minimum positive of both polynomials is independent of the stripe (ribbon) width, and it is also independent of rows number parity, whether even or odd. As the  $N$  increases, the minimum positive is convergent to an approximate constant value of 1.02.

The same Figure 2.3 displays the analogous behavior of the maximum negative of  $\Delta$  for first polynomial (2.26) and second polynomial 2.27. The overall conclusion from Figure 2.3 is that edge modes, in small rows number  $N \leq 20$ , are dependent on both the stripe width and the rows number parity. This is a consequence of the interaction between the two edges in the small range of  $N$ . As  $N$  increases above 20, the edge modes become independent of both the stripe width and the parity. This is an indication of minimal effects of the interaction between the two edges after  $N = 20$ . That behavior agrees with our previous results for the special case of  $N$  becoming large, as discussed above. Also, it is noted in the range of  $N$  larger than 20, that the difference between minimum positive and maximum negative is nearly constant and independent of the stripe width and rows number parity, as expected.

## 2.4 SW dispersion relations

To obtain the dispersion relations for the above system, a Fortran program was first written with the algorithm A.2 for solving the first polynomial (2.26) and the second polynomial (2.27) by Laguerre's method using two subroutines `zroots` and `laguer` adapted from [90], which were used before. The values of physical parameters for calculating these dispersion relations are chosen as follow:  $S = 1$ ,  $J = 1$ ,  $D = D_e = 0$  and  $g\mu_B H_0 = 0.3J$ . The chosen value for the ratio

between the edge exchange and area exchange is  $r = J_e/J = 0.04$ , which satisfies the existence condition 2.24 for edge mode. The chosen values of  $q_x a$  run from 0 to  $\pi$  corresponding to the first Brillouin zone center and boundary respectively.

### 2.4.1 Tridiagonal matrix method results

The numerical results for calculating the SW dispersion relations in the case of a 2D square lattice using the tridiagonal matrix (TM) method with the above algorithm and physical parameters are displayed in Figures 2.4-2.7. These figures show plots of the SW frequency in terms of the dimensionless quantity  $\omega/SJ$  as a function of the dimensionless wavevector  $q_x a$  for various values of  $N$ . The two polynomials (2.26) and (2.27) lead to the area and edge modes being symmetric about  $\omega/SJ = 0$ . As a result, we have chosen to show only the physically-relevant positive frequency branches. It is known that the total number of SW modes (made up of area modes and edge modes) must be equal to  $N$  for all values of the wavevector. This is because they are the normal modes of a  $N$ -layer system.

All the figures display similar general features for the ferromagnetic 2D stripes when  $N$  is relatively small. Here, for simplicity, we focus on the localized edge modes, which occur outside the range of frequencies of the area modes. These area modes are upper bounded by the frequency obtained when the value of  $x$  is equal to 1, and lower bounded by the frequency obtained when the value of  $x$  is equal to  $-1$ , as shown in the Figures 2.4-2.7. The figures show that in all cases that there are two edge modes appearing above the area modes region. However, they occur in only part of the Brillouin zone (above a certain threshold wave vector) because of the need to satisfy the localization requirements. As  $N$  increases, it is seen that the frequency difference between the two edge modes decreases, which is a consequence of

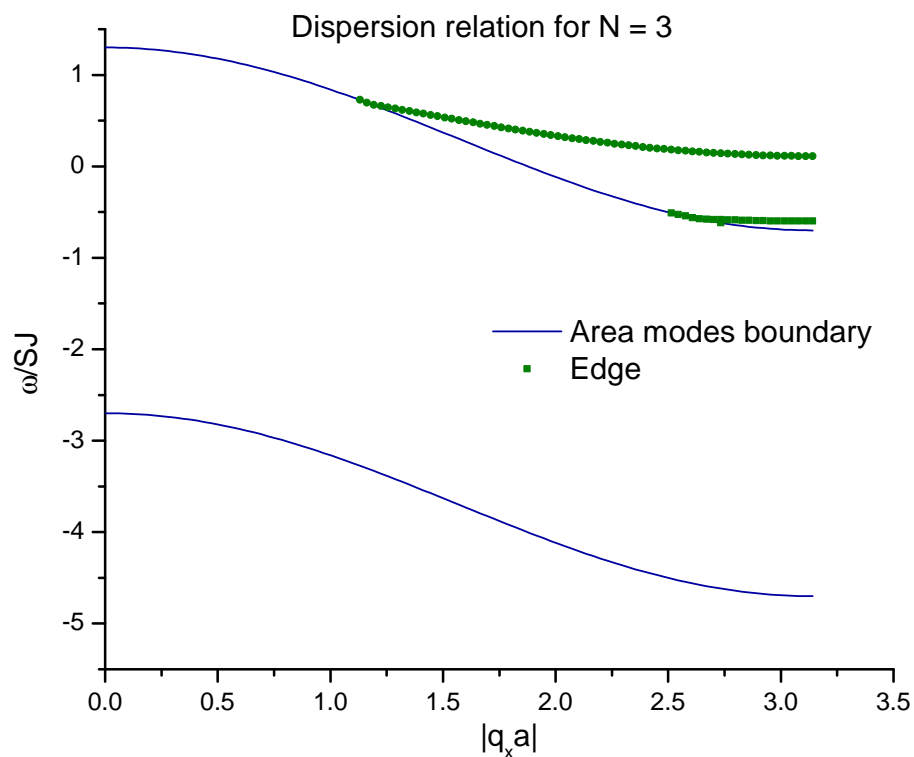


Figure 2.4: Frequencies of the edge SW modes (in units of  $SJ$ ) plotted against the wavevector  $q_x a$  for stripe with width  $N = 3$ , where the lines corresponding to  $x = 1$  and  $x = -1$  are the upper and lower boundary for the area modes.

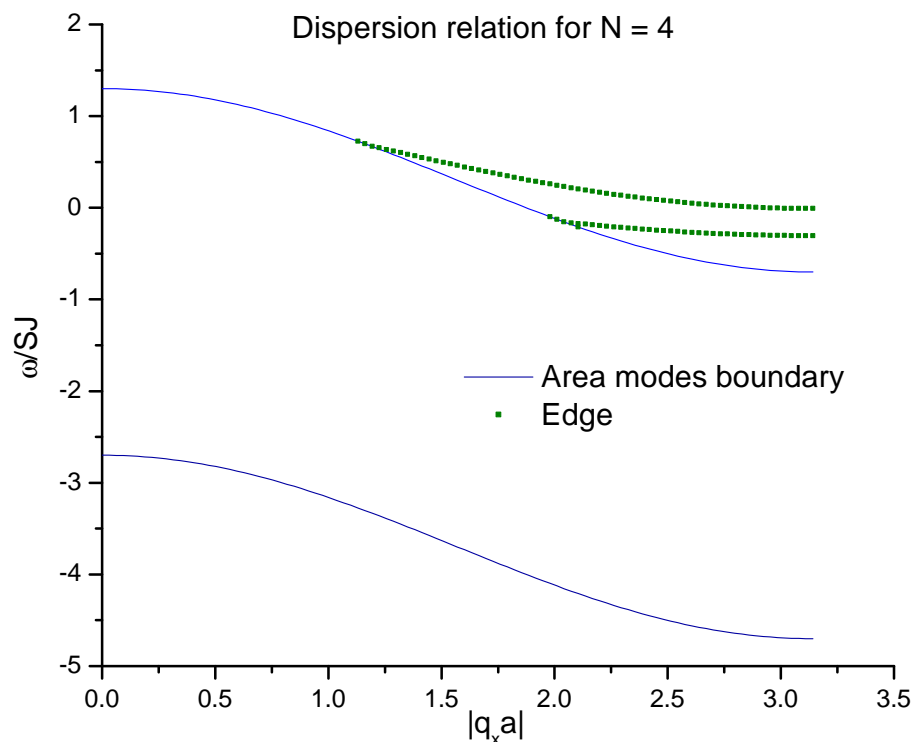


Figure 2.5: Frequencies of the edge SW modes (in units of  $SJ$ ) plotted against the wavevector  $q_x a$  for stripe with width  $N = 4$ , where the lines corresponding to  $x = 1$  and  $x = -1$  are the upper and lower boundary for the area modes.

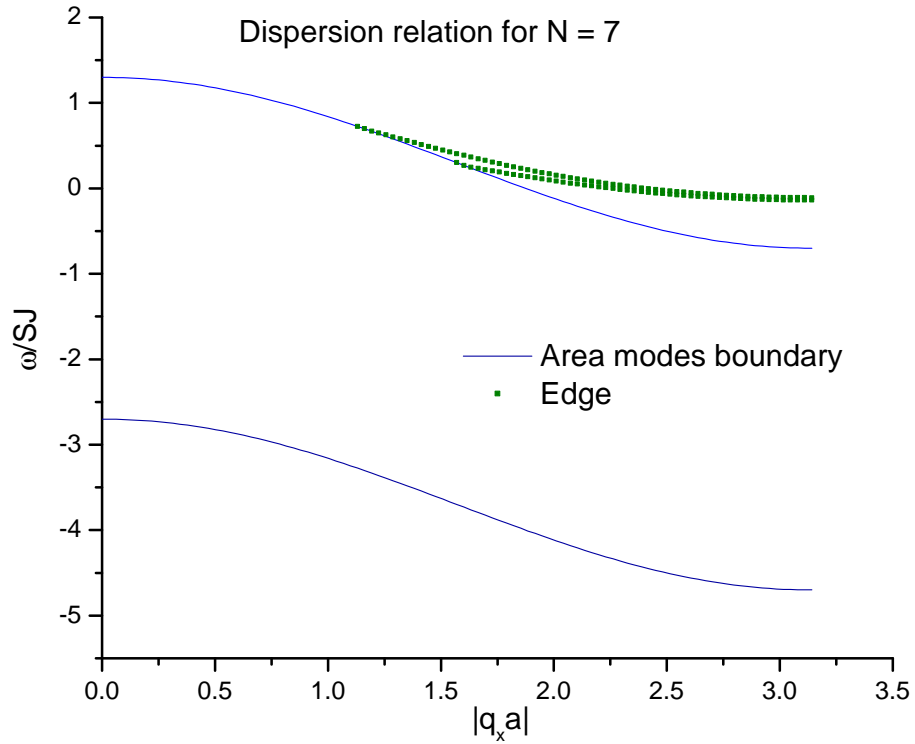


Figure 2.6: Frequencies of the edge SW modes (in units of  $SJ$ ) plotted against the wavevector  $q_x a$  for stripe with width  $N = 7$ , where the lines corresponding to  $x = 1$  and  $x = -1$  are the upper and lower boundary for the area modes.

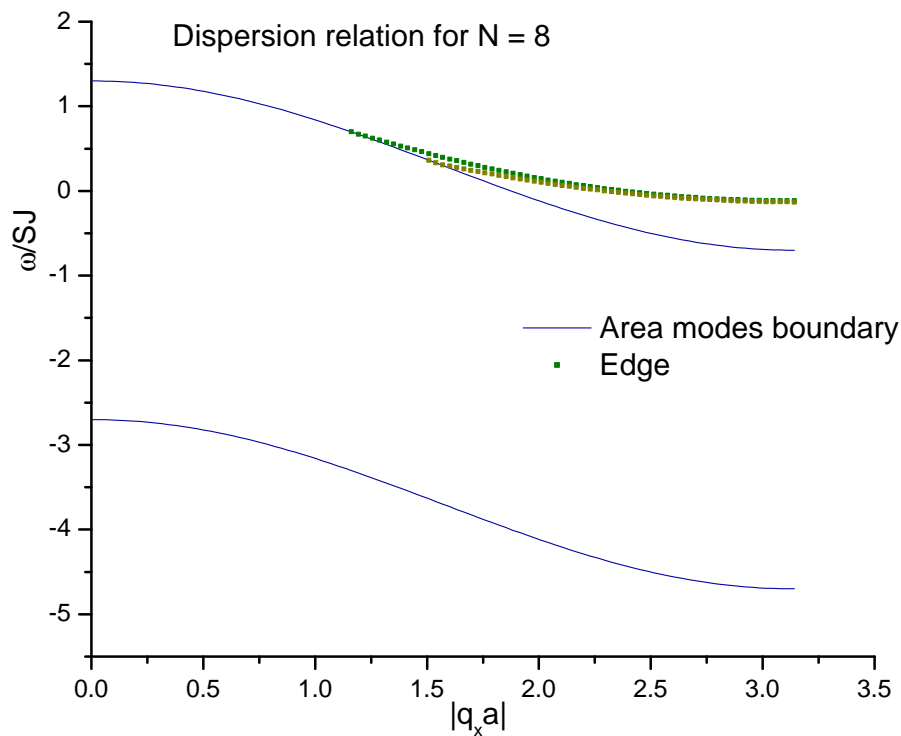


Figure 2.7: Frequencies of the edge SW modes (in units of  $SJ$ ) plotted against the wavevector  $q_x a$  for stripe with width  $N = 8$ , where the lines corresponding to  $x = 1$  and  $x = -1$  are the upper and lower boundary for the area modes.



the stripe width becoming larger than the exponential decay length of the localized modes (as discussed in Section 2.3). We reserve discussion of the area modes until the next subsection.

### 2.4.2 Direct diagonalization method results

Another way to calculate the SW dispersion relations for the 2D square lattice is the direct diagonalization (DD) method (or exchange matrix method) [92]. The DD method is discussed more extensively in Chapter 3 in the context of other lattice structures. It is a convenient alternative to the previous TM method, because it easily allows for calculations of all (edge and area) SW modes, but it lacks the physical insights provided by the TM method. In the DD method the SW dispersion relations are the eigenvalues of an exchange matrix  $\mathbf{E}$ , which is defined as explained below (see also Chapter 3).

In the present case, the DD method consists of writing down the coupled equations of motion for a transverse spin component in each row of the stripe, as was done in Eqs. (2.8) and (2.9). It then follows that the eigenvalues of the  $N \times N$  matrix  $A$ , which was defined in Eq. (2.10) will provide the  $N$  physical SW frequencies. Hence matrix  $A$  is the same as the so-called “exchange matrix” in the square-lattice geometry considered here [92]. Hence the required  $E$  matrix has two matrix components: The first component can be written as  $\alpha I_N$  represents the insite energy value in the lattice where  $\alpha$  is defined by

$$\alpha = (g\mu_B H_0 + (2S - 1)D_n) \delta_{mn}. \quad (2.29)$$

The second component which we will denote as  $T(q_x)$  represents the effect of lattice geometry in the particles exchange “flow” (or propagation) inside the lattice under NN exchange. Its

elements are derived from the following exchange sum

$$\gamma(q_x) = \frac{1}{2}S \sum_{\nu} J_{i,j} e^{-iq_x \cdot (\mathbf{r}_i - \mathbf{r}_j)}. \quad (2.30)$$

The sum for the exchange terms  $J_{i,j}$  is taken to be over all  $\nu$  NNs in the lattice. Using figure 2.1 to identify the NN connections for a site in the 2D square lattice we may apply it to the definition of the exchange sum (2.30). The obtained exchange matrix for the 2D square lattice is given in Table 2.1, which is a real matrix as expected from the square lattice geometry. The matrix elements consists of three types: the diagonal element  $\varepsilon$  representing the NN exchange between sites that both lie in the same line along the direction of translational symmetry of the stripe, the off-diagonal element  $\beta$  representing the NN exchange between the sites at a given line and sites in the previous line, and the off-diagonal element  $\gamma$  representing the NN exchange between the sites at a given line and sites in the next line.

Table 2.1: Nearest neighbor exchange matrix elements for 2D square lattice

Parameter	Square lattice
$\beta$	$\frac{SJ}{2}$
$\varepsilon$	$\frac{SJ}{2}(2 \cos(q_x a))$
$\gamma$	$\frac{SJ}{2}$

Since the 2D square lattice is a Bravais lattice the  $\mathbf{E}$  matrix size is  $N \times N$  and it is equal to the sum of the insite energy matrix and the exchange matrix, i.e.  $\mathbf{E} = \alpha I_N + T(q_x)$ . As mentioned, it turns out that  $\mathbf{E}$  is identical to the matrix  $A$  (2.10) obtained before in the tridiagonal matrix method. Following the numerical calculations (see also the next chapter for details), the following results are obtained.

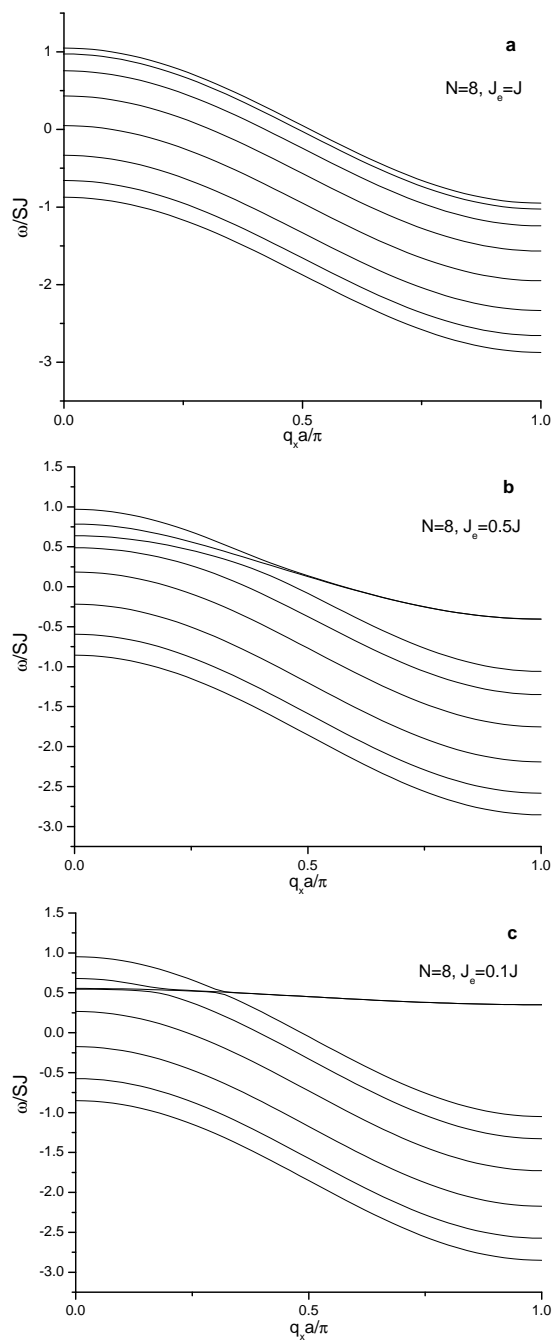


Figure 2.8: SW dispersion relations for area and edge modes for pure material ferromagnetic 2D square lattice stripes for  $N = 8$  where  $D = D_e = D_l = 1.0$  and  $\alpha = -0.95$  (a)  $J_e = J$  (b)  $J_e = 0.5J$  (c)  $J_e = 0.1J$ .

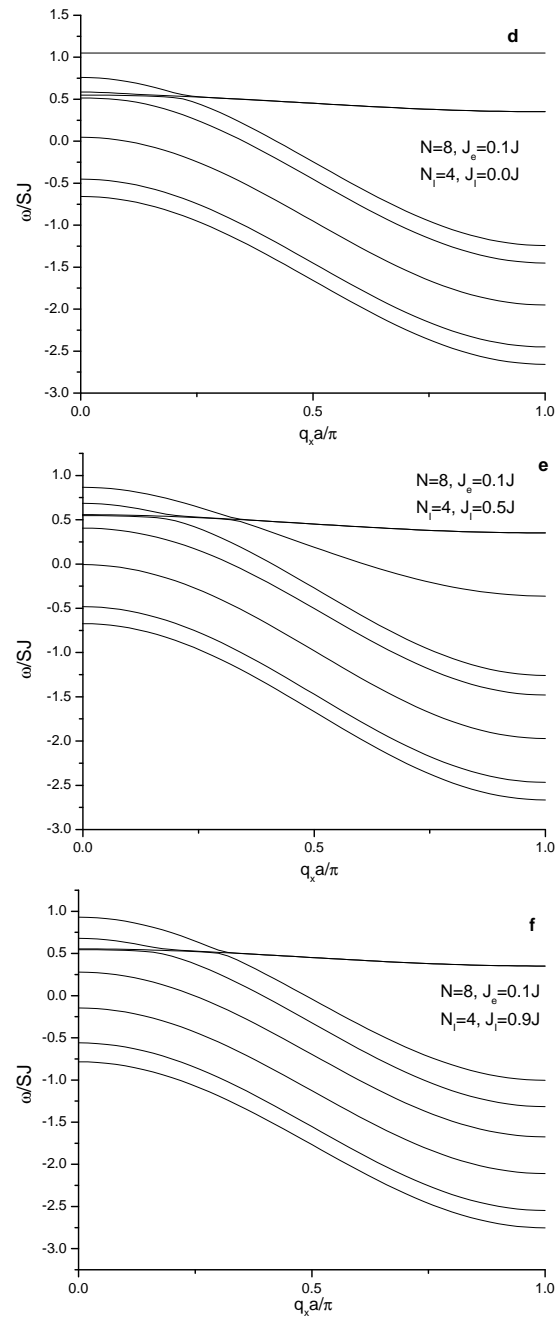


Figure 2.9: SW dispersion relations for area and edge modes for material with an impurity ferromagnetic 2D square lattice stripes for  $N = 8$  where  $D = D_e = D_I = 1.0$  and with adding an impurity line at line number 4 for  $J_e = 0.1J$  with (d)  $J_I = 0.0J$  (e)  $J_I = 0.5J$  (f)  $J_I = 0.9J$ .

Figures 2.8 and 2.9 show the obtained SW dispersions for a ferromagnetic 2D square lattice stripe with width  $N = 8$ , taking different values of the exchange and anisotropy parameters including the effects of impurities. Figures 2.8 describes a magnetic stripe without impurities and with different edge exchange while Figures 2.9 describe a magnetic stripe with an impurity line at line number 4 and with different impurity exchange (compared to the bulk value  $J$ ). The figures confirm the feature of ferromagnetic 2D square lattice stripes that the area and edge SW consist of 8 branches in total. The results are consistent with those as seen before in the tridiagonal matrix method, except that we now show the dispersion of both area and edge modes.

Figure 2.8a shows the dispersion when the two edge exchange parameters are equal to the bulk exchange, which for the given material properties leads to an absence of edge modes for the 2D square lattice, as expected from the conditions deduced in Eq.(2.24) (and its generalization to finite  $N$ ).

Figure 2.8b shows the effect of reducing the edge exchange to half the value of the bulk exchange. In this case there is a tendency for two of the modes to become localized as edge modes when  $q_x$  is sufficiently large (see the two highest-frequency branches). The effect is analogous to examples shown earlier in Fig 2.5 where there were also two edge SW branches.

Figure 2.8c shows the effect of a further reduction of the edge exchange to  $0.1J$ . The localization of two of the SW branches as (almost degenerate) edge modes at larger wave vectors is now more pronounced. Also at smaller wave vectors these same modes have “resonances” (with mode repulsion and splitting effects) with the other area modes.

The plots in Figure 2.9 show the modified dispersion relations due to the effect of introducing substitutionally a line of magnetic impurities at row 4. This has the effect of splitting

the stripe into two narrower interacting substripes with 3 lines and 4 lines. The strength of the interaction between the two substripes depends on the value of the impurities exchange value  $J_I$ . The top panel (labelled d) in Figure 2.9 shows the case when  $J_I = 0$ , leading to the appearance of a flat localized state above the the area modes. Those localized states are understood as accumulation sites for magnons in the interface created by the tunneling between the two substripes through the impurities line.

Figures 2.9 e and f show the modified dispersion relations due to increasing the impurity line exchange from zero to 0.5 and 0.9, respectively, of the bulk exchange value. Progressively the localization of the impurity modes becomes less evident (as expected).

## 2.5 Discussion

The dispersions relations of the area and edge SWs, and the effect of the stripe width on them for 2D ferromagnetic square lattice stripes, have been studied using both the tridiagonal matrix (TM) method and the direct diagonalization (DD) method, which lead to consistent results. The results obtained analytically and numerically for the area and edge SWs are broadly analogous to the behavior also seen for 2D Heisenberg antiferromagnetic square lattices, experimentally and theoretically [93, 94, 95], in film geometries.

Despite the fact that the DD method gives a very reasonable physical explanation for the 2D square lattice SW modes, the TM method has an advantage in studies of the edge effects and its energy states due to the clear distinction made between edges modes and area modes.

A general conclusion regarding the unusual behavior of spin waves in the 2D square lattice (along with the results for the edge and impurity SW modes) is that the present work may

be of interest in seeking an explanation for HTS. Since it is known that HTS is linked to the properties of the 2D square antiferromagnetic lattice, there could be a role for SW to mediate the electrons for the formation of a Cooper pair with much less energy than the Cooper pair created by phonon-mediated electrons [96, 97, 98, 99, 51, 100].

# Chapter 3

## Spin Waves in Ferromagnetic Stripes with a Honeycomb Lattice

### 3.1 Introduction

The superior physical properties of graphene with its promising applications are mainly attributed to its crystal structure with a 2D honeycomb lattice and its short range interactions. While graphene itself is not a strongly magnetic material, many experimental and theoretical studies have been carried out for related magnetic properties and proposed designs of graphene-based spintronic devices [101, 102]. Graphene is formed due to the natural bonding stability of carbon atoms, as discussed in Chapter 1, but there are no examples of natural atomic elements able to form a stable planar ferromagnetic 2D honeycomb lattice. In this case, however, arrays of ferromagnetic nanodots can be used as magnetic artificial atoms [103] with the ability to display the magnetic properties in the same way as the quantum dots nanostructures are used as artificial atoms with the ability to design tunable electronic properties not found in naturally existing atomic elements [104, 105, 106, 107]. A question of interest from the physics and



the technology point of view and from advances in the material science fabrication techniques is whether we can fabricate stripes of ferromagnetic dots with a 2D honeycomb lattice as already done for other magnetic structures [108, 109, 110]. In this case, the ferromagnetic dots arranged as 2D honeycomb lattice stripes would share both crystal structure and short range interaction with graphene. The expected physical properties of these honeycomb stripes might lead to a new technology, e.g., in the field of spintronic devices. A theoretical study is therefore needed to predict the similarities and differences between magnetic and electronic short range interactions in the 2D honeycomb lattice.

Many studies have been conducted for the thermodynamic properties of hexagonal and honeycomb atomic spin lattices [111, 112, 113, 114]. Many of these studies are for 3D systems and reveal low-dimensional magnetic behavior with predominantly antiferromagnetic behavior like  $\beta$ - $\text{Cu}_2\text{V}_2\text{O}_7$  [115], or hexagonal spin lattices with ferromagnetic and antiferromagnetic interactions [116]. Some studies have been conducted on the SW excitations in ferromagnetic nanostructure arrays [55, 63] but there are no known studies for ferromagnetic stripes of nanodots arranged in 2D honeycomb lattices.

In this chapter, we will study the SWs of 2D ferromagnetic stripes with a honeycomb lattice for two different geometric orientations corresponding to zigzag and armchair edges. We will employ the direct diagonalization (DD) method with the same Hamiltonian used in the case of the 2D square lattice in Chapter 2. The new results will give us a better understanding of how the lattice geometry affects on the SW properties of 2D materials. As well as presenting results for the SW dispersion relations, we will calculate some related density of states (DOS) functions.

## 3.2 Theoretical model

The systems under study here are 2D Heisenberg ferromagnetic stripes (or nanoribbons) formed from arrays of dots in the  $xy$ -plane with either armchair or zigzag edges. We assume a honeycomb (graphene like) lattice with the crystallographic description given in Section 1.1, and shown in Figure 1.5. The average spin alignment of the magnetic sites is taken to be in the  $z$  direction, which is also the direction of the applied magnetic field. The nanoribbon is of finite width in the  $y$  direction with  $N$  rows (labeled as  $n = 1, \dots, N$ ) and it is infinite in  $x$  direction ( $-\infty \Leftrightarrow \infty$ )(see Figure 3.1).

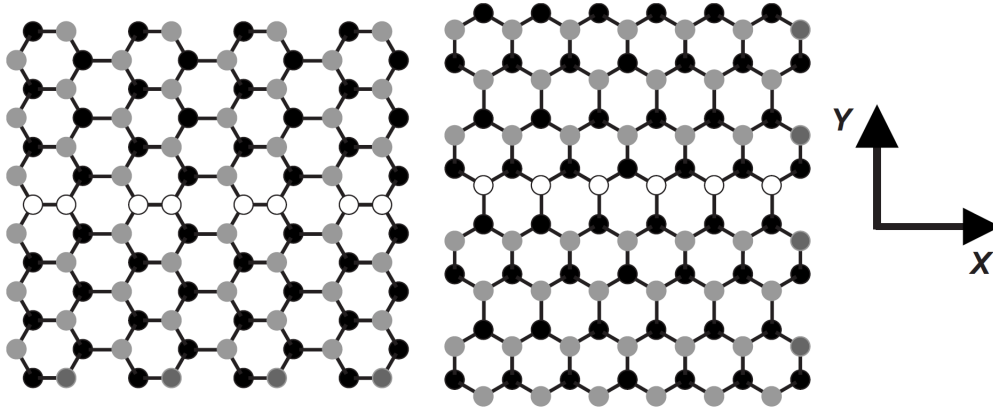


Figure 3.1: Armchair (left) and zigzag (right) edges for 2D Heisenberg ferromagnetic dots forming honeycomb stripes in the  $xy$ -plane. The black (gray) dots refer to the sublattice A(B) with the additional possibility of a line of impurities (white dots) in the middle of the sheet. The stripes are finite in the  $y$  direction with  $N$  rows ( $n = 1, \dots, N$ ) and they are infinite in the  $x$  direction.

The total Hamiltonian of the system is given by Equation (1.40). The notation is defined in Chapter 1, where the first term is the Heisenberg NN exchange term, the second term is the Zeeman energy term due to an applied field  $H_0$ , and the third term is the uniaxial anisotropy term. The summations over  $i$  and  $j$  run over all the sites where  $i$  and  $j$  always belong to different sublattices. This is because in the honeycomb lattice, the NNs of the  $A$  sites are always  $B$  sites

and vice versa (see Section 1.1). The NN exchange  $J_{ij}$  has a constant “bulk” value  $J$  when either  $i$  and  $j$  are in the interior of the nanoribbons, and another constant value  $J_e$  when  $i$  and  $j$  are both at the edge of the nanoribbon (i.e., in row  $n = 1$  or  $n = N$ ). Similarly, for the site-dependent uniaxial anisotropy term  $D_i$ , we assume that it has a constant value  $D$  when the site  $i$  is inside the nanoribbon, and it is equal to  $D_e$  for sites at the edge of the nanoribbon.

To calculate the SWs for this system at low temperatures  $T \ll T_c$  where  $S^z \simeq S$  for each spin, we again use the Holstein-Primakoff (HP) transformation and follow the procedures of Chapter 1 to express the total Hamiltonian in terms of boson operators for the two sublattices A and B. We arrive at a similar equation to Equation (1.46), where the constant term  $E_0$  is the energy of the ground state for the ferromagnetic system given by Equation (1.47) and the operator term  $\hat{H}_s$  has the following form

$$\begin{aligned} H_s = & -\frac{1}{2}S \sum_{i,j} J_{i,j} (a_i b_j^\dagger + a_i^\dagger b_j - b_j^\dagger b_j - a_i^\dagger a_i) \\ & + \sum_i [g\mu_B H_0 + (2S - 1)D_k] a_i^\dagger a_i + \sum_j [g\mu_B H_0 + (2S - 1)D_k] b_j^\dagger b_j, \end{aligned} \quad (3.1)$$

where  $a_i^\dagger$  ( $a_i$ ) and  $b_j^\dagger$  ( $b_j$ ) are the creation and the annihilation boson operators for sublattices A and B respectively.

Since the nanoribbon extends to  $\pm\infty$  in the  $x$  direction, we may introduce a 1D Fourier transform to wavevector  $q_x$  along the  $x$  direction for the boson operators  $a_i^\dagger$  ( $a_i$ ) and  $b_j^\dagger$  ( $b_j$ ) as follows:

$$\begin{aligned} b_j(x) &= \frac{1}{\sqrt{N_0}} \sum_n b_n(q_x) e^{-i\mathbf{q}_x \cdot \mathbf{r}_j}, & b_j^\dagger(x) &= \frac{1}{\sqrt{N_0}} \sum_n b_n^\dagger(q_x) e^{i\mathbf{q}_x \cdot \mathbf{r}_j}, \\ a_i(x) &= \frac{1}{\sqrt{N_0}} \sum_n a_n(q_x) e^{-i\mathbf{q}_x \cdot \mathbf{r}_i}, & a_i^\dagger(x) &= \frac{1}{\sqrt{N_0}} \sum_n a_n^\dagger(q_x) e^{i\mathbf{q}_x \cdot \mathbf{r}_i}. \end{aligned} \quad (3.2)$$

Here  $N_0$  is the (macroscopically large) number of spin sites in any row,  $\mathbf{q}_x$  is a wavevector in the first Brillouin zone of the reciprocal lattice and  $\mathbf{r}_i$  and  $\mathbf{r}_j$  are the position vectors of any magnetic sites  $i$  and  $j$ . The new operators obey the following commutation relations:

$$\left[ a_n(q_x), a_n^\dagger(q'_x) \right] = \delta_{q_x q'_x}, \quad \left[ b_n(q_x), b_n^\dagger(q'_x) \right] = \delta_{q_x q'_x}. \quad (3.3)$$

Also, we define the exchange sum:

$$\gamma(q_x) = \frac{1}{2} S \sum_{\nu} J_{i,j} e^{-i\mathbf{q}_x \cdot (\mathbf{r}_i - \mathbf{r}_j)}. \quad (3.4)$$

The sum for the exchange terms  $J_{i,j}$  is taken to be over all  $\nu$  NNs in the lattice which depends on whether the edge configuration is zigzag or armchair. For the armchair configuration, the exchange sum gives the following amplitude factors  $\gamma_{m'm'}(q_x)$

$$\gamma_{m'm'}(q_x) = \frac{1}{2} S J \left[ \exp(iq_x a) \delta_{n',n} + \exp\left(i\frac{1}{2}q_x a\right) \delta_{n',n\pm 1} \right], \quad (3.5)$$

while for the zigzag case it gives

$$\gamma_{m'm'}(q_x) = \frac{1}{2} S J \left[ 2 \cos\left(\frac{\sqrt{3}}{2}q_x a\right) \delta_{n',n\pm 1} + \delta_{n',n\mp 1} \right]. \quad (3.6)$$

The  $\pm$  sign depends on the sublattice since the sites alternate from A and B.

Substituting Equations (3.2) and (3.4) into Equation (3.1), and rewriting the summations, we have

$$H_s = \sum_{q_x, m'm'} \left\{ \alpha \left( a_n^\dagger a_{n'} + b_n^\dagger b_{n'} \right) + \left( \gamma(q_x) a_n b_{n'}^\dagger + \gamma(-q_x) a_n^\dagger b_{n'} \right) \right\}. \quad (3.7)$$

Here the second term describes the coupling between the sublattices, and  $\alpha$  is defined by

$$\alpha = (g\mu_B H_0 + (2S - 1)D_n) \delta_{nn'}. \quad (3.8)$$

In order to diagonalize  $\hat{H}_s$  and obtain the SW frequencies using this direct diagonalization (DD) method, we may consider the time evolution of the creation and the annihilation operators  $a_i^\dagger$  ( $a_i$ ) and  $b_j^\dagger$  ( $b_j$ ), as calculated in the Heisenberg picture. This represents a generalization of the DD method in Chapter 2 because we now have two sublattices (and therefore two sets of operators). The equations of motion (using units with  $\hbar = 1$ ) for the annihilation operators  $a_i$  ( $b_j$ ) are as follows [44, 60, 37, 43, 48]:

$$\begin{aligned} \frac{da_n}{dt} &= i[H, a_n] \\ &= i \sum_{q_x, nn'} -\alpha a_{n'} - \gamma(-q_x) b_{n'} \end{aligned} \quad (3.9)$$

and

$$\begin{aligned} \frac{db_n}{dt} &= i[H, b_n] \\ &= i \sum_{q_x, nn'} -\alpha b_{n'} - \gamma(q_x) a_{n'} \end{aligned} \quad (3.10)$$

where the commutation relation in Equation (3.3) was used, as well as the operator identity  $[AB, C] = A[B, C] + [A, C]B$ .

The dispersion relations of the SWs (i.e., their energy or frequency versus wavevector) can now be obtained by solving the above operator equations of motion. The SW energy can be expressed in terms of the SW frequency using the relation  $E = \hbar\omega$ , and assuming that SW

modes behave like  $\exp[-i\omega(q_x)t]$ . We get the following sets of coupled equations:

$$\omega(q_x)a_n = \sum_{q_x, nn'} \alpha a_{n'} + \gamma(-q_x)b_{n'}, \quad (3.11)$$

$$\omega(q_x)b_n = \sum_{q_x, nn'} \gamma(q_x)a_{n'} + \alpha b_{n'}. \quad (3.12)$$

The above equations can be written in matrix form as follows

$$\omega(q_x) \begin{bmatrix} a_n \\ b_n \end{bmatrix} = \begin{bmatrix} \alpha I_N & T(q_x) \\ T^*(q_x) & \alpha I_N \end{bmatrix} \begin{bmatrix} a_n \\ b_n \end{bmatrix}, \quad (3.13)$$

where the solution of this matrix equation is given by the condition

$$\det \begin{bmatrix} -(\omega(q_x) - \alpha)I_N & T(q_x) \\ T^*(q_x) & -(\omega(q_x) - \alpha)I_N \end{bmatrix} = 0. \quad (3.14)$$

Here,  $T(q_x)$  is the exchange matrix, which depends on the orientation of the ribbon, and  $\omega(q_x)$  are the required SW frequencies. The matrix  $T(q_x)$  is given by

$$\begin{pmatrix} \varepsilon & \beta & 0 & 0 & \cdots \\ \beta & \varepsilon & \gamma & 0 & \cdots \\ 0 & \gamma & \varepsilon & \beta & \cdots \\ 0 & 0 & \beta & \varepsilon & \cdots \\ \vdots & \vdots & \vdots & \vdots & \ddots \end{pmatrix}, \quad (3.15)$$

where the parameters  $\varepsilon$ ,  $\gamma$ , and  $\beta$  depend on the stripe edge geometry as given in Table 3.1.

Equation (3.14) is similar to the one obtained for electronic excitations in graphene ribbons in reference [39], where the tight binding model was employed with the Hamiltonian given in Equation (1.31). If the NNN hopping is neglected, the only essential difference between the Heisenberg model and the tight binding model results is the existence of the  $\alpha$  term in the Heisenberg model. This extra term is in the diagonal of the Hamiltonian matrix and so it will shift the total SW energy by an amount related to the in-site Zeeman energy term and the uniaxial anisotropy energy term. This similarity between graphene and ferromagnetic stripes emphasizes that formally the Heisenberg and tight binding model are closely-related models with the NN interactions represented respectively by  $t_{ij}$  and  $J_{ij}$ .

Table 3.1: Nearest neighbor exchange matrix elements for a 2D magnetic honeycomb lattice

Parameter	Zigzag	Armchair
$\varepsilon$	0	$\frac{SJ}{2}e^{-iq_x a}$
$\beta$	$SJ \cos(\sqrt{3}q_x a/2)$	$\frac{SJ}{2}e^{iq_x a/2}$
$\gamma$	$\frac{SJ}{2}$	$\frac{SJ}{2}e^{iq_x a/2}$

### 3.3 Method for numerical calculations

The dispersion relations for the above 2D Heisenberg ferromagnetic stripes are obtained numerically as the eigenvalues [89, 90] arising from the matrix condition given by Equation (3.13). The first step in solving this eigenvalue problem, for any given value of the wavevector  $q_x$ , is to construct the matrix

$$\mathbf{E} = \begin{bmatrix} \alpha I_N & T(q_x) \\ T^*(q_x) & \alpha I_N \end{bmatrix}, \quad (3.16)$$

which is  $2N \times 2N$  since both  $I_N$  and  $T(q_x)$  are  $N \times N$  for the number  $N$  of rows in the stripe.

First, the matrix  $\alpha I_N$  is independent of the value of the wavevector  $q_x$  and it is simply constructed using the material parameters of the stripe to evaluate the  $\alpha$  values as defined in Equation (3.8). Second, the matrices  $T(q_x)$  and conjugate  $T^*(q_x)$  depend on the value of the wavevector  $q_x$ , the material parameters of the stripe in terms of  $SJ$ , and the stripe edge geometry as zigzag or armchair (see Table 3.1). For the zigzag case the elements of the exchange matrix  $T(q_x)$  are real (see Table 3.1). Consequently  $T(q_x) = T^*(q_x)$ , and therefore the matrix  $\mathbf{E}$  is real too. A standard procedure, following reference [90], to obtain the eigenvalues for a real matrix is to follow the steps below:

First, balance the real matrix  $\mathbf{E}$  by using similarity transformations in order to have comparable norms for the corresponding rows and columns of the matrix, reducing the sensitivity of the eigenvalues to rounding errors. It is done here using the subroutine `balanc` [90]. Second, reduce the matrix  $\mathbf{E}$  to a matrix that has zeros everywhere below the diagonal except for the first subdiagonal row, i.e., to upper Hessenberg form. It is done here using the subroutine `elmhes` [90]. Third, find all the eigenvalues of the matrix  $\mathbf{E}$  in the upper Hessenberg form. It is done here using the subroutine `hqr` [90]. Fourth, sort the obtained eigenvalues of the matrix  $\mathbf{E}$  (done here using the subroutine `picksrt` [90]) and plot the dispersion relations for the given stripe.

For the armchair case, the elements of the exchange matrix  $T(q_x)$  are complex (see Table 3.1), and  $T(q_x)$  is the Hermitian conjugate to  $T^*(q_x)$ , so consequently  $\mathbf{E}$  is a Hermitian matrix. One way to obtain the eigenvalues of a Hermitian complex matrix like  $\mathbf{E}$  is to convert it to an equivalent real matrix [90], and then use the above standard procedures to obtain the eigenvalues for a real matrix.

The conversion to a real matrix is done as follows. First the Hermitian complex matrix  $\mathbf{E}$



can be written in terms of its real and imaginary parts as

$$\mathbf{E} = \mathbf{Re}(q_x) + i\mathbf{Im}(q_x) \quad (3.17)$$

where  $\mathbf{Re}(q_x)$  and  $\mathbf{Im}(q_x)$  are  $2N \times 2N$  real matrices. Then, using the above representation of  $\mathbf{E}$  in the Equation (3.13), we get the following  $2N \times 2N$  complex eigenvalue problem

$$\omega(q_x)(\mathbf{u}_n + i\mathbf{v}_n) = (\mathbf{Re}(q_x) + i\mathbf{Im}(q_x)) \cdot (\mathbf{u}_n + i\mathbf{v}_n) \quad (3.18)$$

where  $\mathbf{u}_n$  and  $\mathbf{v}_n$  represent column vectors of the operators. The above Equation (3.18) is equivalent to solving the following  $4N \times 4N$  real eigenvalue problem

$$\omega(q_x) \begin{bmatrix} \mathbf{u} \\ \mathbf{v} \end{bmatrix} = \begin{bmatrix} \mathbf{Re}(q_x) & -\mathbf{Im}(q_x) \\ \mathbf{Im}(q_x) & \mathbf{Re}(q_x) \end{bmatrix} \begin{bmatrix} \mathbf{u} \\ \mathbf{v} \end{bmatrix}. \quad (3.19)$$

This can now be solved following the same procedure as outlined above.

The edge effects in the 2D magnetic stripes are very important, but they are found to be more significant in the case of a honeycomb lattice compared to the case of a square lattice in Chapter 2. They are introduced in this model numerically by using edges material properties in the elements (1, 1) and  $(N, N)$  in the  $\alpha I_N$  matrix, and the elements (1, 1), (1, 2) and (2, 1) for the lower edge and the elements  $(N, N)$ ,  $(N, N - 1)$  and  $(N - 1, N)$  for the upper edge in the matrixes  $T(q_x)$  and  $T^*(q_x)$ .

The pure 2D magnetic stripes offer very interesting dispersion relations, but to be suitable for technological devices applications one would also like the flexibility to engineer their properties. One way to do so is by the introduction of magnetic impurities lines substitutionally

into the stripe materials, which is very similar to suggested methods for engineering graphene materials [39]. The effects of one or two lines of impurities at any chosen row numbers  $n_0$  and  $n'_0$  in the stripe can readily be introduced in this model by using the magnetic impurities material properties in the elements  $(n_0, n_0)$  and  $(n'_0, n'_0)$  of the  $\alpha I_N$  matrix, and in the elements of the matrices  $T(q_x)$  and  $T^*(q_x)$  that express the interaction of the impurity line with itself in the diagonal element  $(n_0, n_0)$  for the first line and  $(n'_0, n'_0)$  for the second line, the interaction of the impurity line with the line before it in the stripe in the elements  $(n_0 - 1, n_0), (n_0, n_0 - 1)$  for the first line and  $(n'_0 - 1, n'_0), (n'_0, n'_0 - 1)$  for the second line, and the interaction of the impurity line with the line after it in the stripe in the elements  $(n_0, n_0 + 1), (n_0 + 1, n_0)$  for the first line and  $(n'_0, n'_0 + 1), (n'_0 + 1, n'_0)$  for the second line.

### 3.4 SW results for zigzag stripes

To compare our results for ferromagnetic stripes using the Heisenberg Hamiltonian with those of graphene nanoribbons using the tight-binding model with NN interactions, we choose our stripe sizes and physical parameters similar to those used in reference [39] for graphene.

#### 3.4.1 SW dispersion relations

Figure 3.2 shows the dispersion relation (with the frequency scaled by the factor  $SJ$ , as explained in Chapter 2) for a zigzag ferromagnetic honeycomb stripe with 20 lines in the absence of impurities, where the NN exchange has a constant value  $J$  through all the stripe including the edges. The same goes for the uniaxial anisotropy term  $D_i$ , which was chosen here to be zero. Hence  $\alpha$  is small and equal to 0.01. In this case, the obtained dispersion relation is very similar

to the dispersion relation for zigzag graphene ribbon with the same size [39]. As the uniaxial anisotropy term  $D_i$  increases to 1 the  $\alpha$  term increases to 1.01. In this case, all the dispersion curves are shifted (see Figure 3.3) as we discussed before. Figures 3.3 and 3.4 show that all modes have a degeneracy of degree two which reflects the symmetry between the parallel rows of the two sublattices  $A$  and  $B$  in the case of zigzag stripes. The dispersion relation for even  $N$  is different from the odd  $N$  case (see Figure 3.4). This is due to the fact that edge states depend on the exchange between a site in the edge and an interior site. The edge sites for even stripes have coordination number equal to 2 (see Figure 3.1). The situation is different for the case of odd stripes, as one set of edge sites has coordination number equal to 2, while the other edge sites have coordination number equal to 1.

Figures 3.5 and 3.6 show the modified dispersion relations due to the effect of introducing substitutionally a magnetic impurities line at row 11 of the zigzag stripes with 20 and 21 lines respectively. The new dispersions are analogous to the behavior seen in the same case for zigzag graphene [39], but shifted in the case of magnetic stripes due to the effect of  $\alpha$ . Introducing the impurities line has the effect of splitting the stripe effectively into two interacting stripes with different sizes. In the case of a 20 line stripe the new stripes are 10 lines and 9 lines, whereas in case of a 21 line stripe the new two stripes are each of 10 lines. The strength of the interaction between the two sub stripes depends on the value of the impurities exchange  $J_I$ , and here the figures show the case when  $J_I = 0$ .

As further examples, Figures 3.7 and 3.8 show the modified dispersion relations due to two magnetic impurity lines at rows 11 and 14 of the zigzag stripes with 20 and 21 lines. Again, the introduction of impurity lines has the effect of splitting the stripe, in this case into three interacting stripes with different sizes. In the case of the 20 line stripe the new stripes are 10

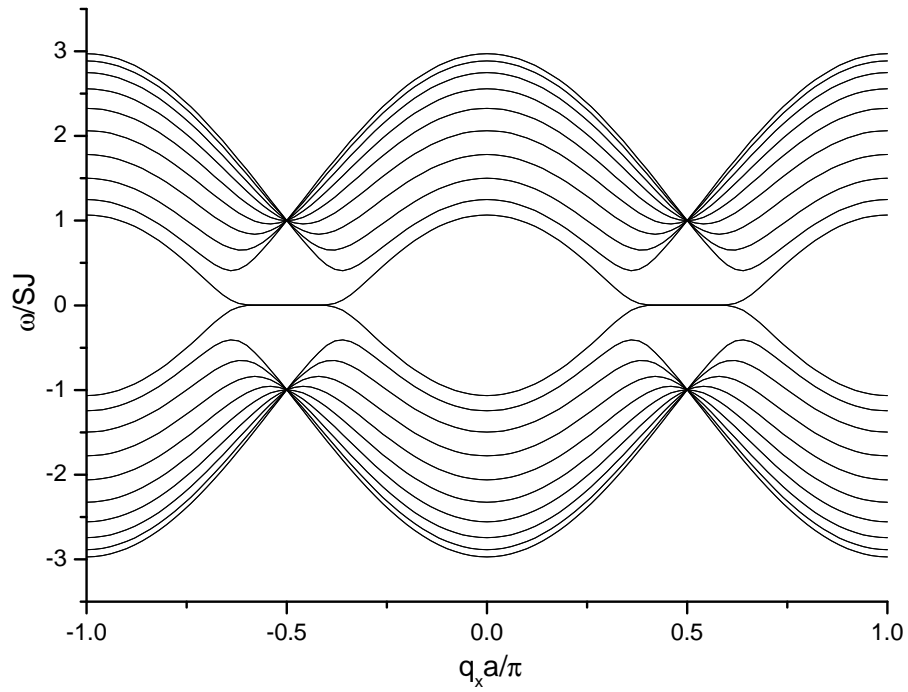


Figure 3.2: SW dispersion for zigzag ferromagnetic honeycomb stripes with  $N = 20$ ,  $J = J_e = 1$ ,  $D = D_e = 0$  and  $\alpha = 0.01$ .

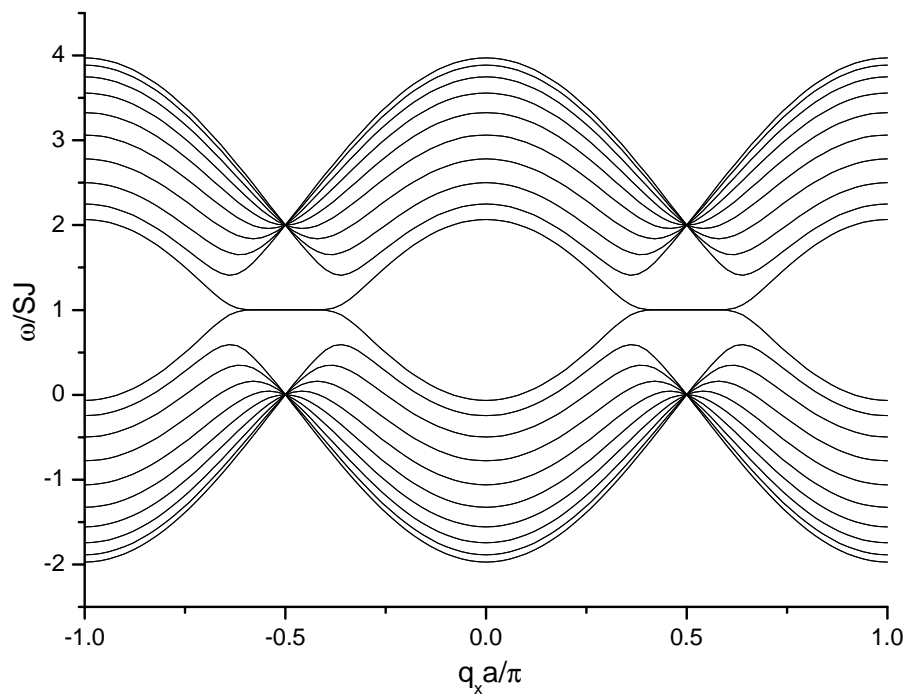


Figure 3.3: SW dispersion for zigzag ferromagnetic honeycomb stripes with  $N = 20$ ,  $J = J_e = 1$ ,  $D = D_e = 1.0$  and  $\alpha = 1.01$ .

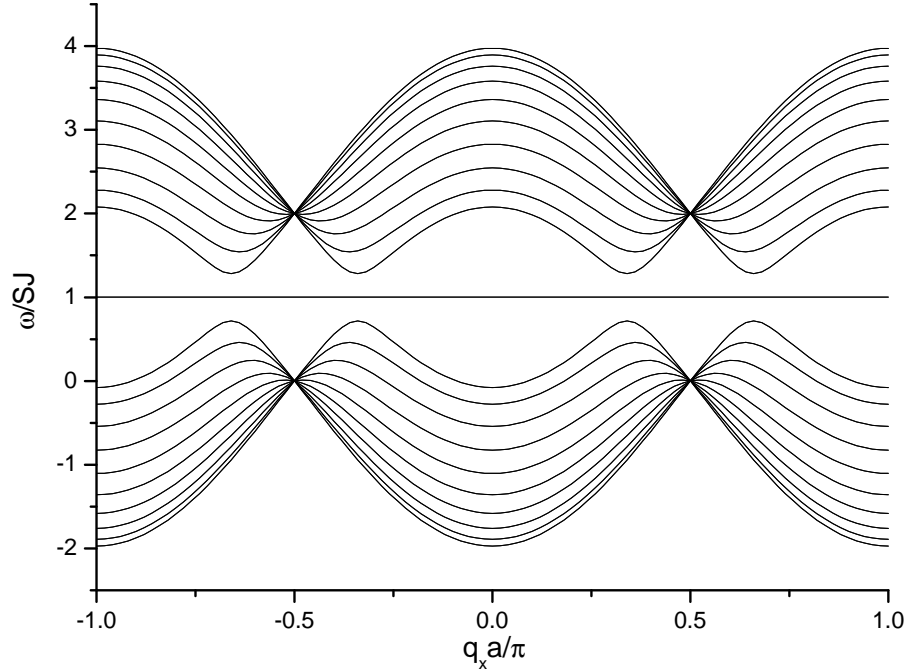


Figure 3.4: SW dispersion for zigzag ferromagnetic honeycomb stripes with  $N = 21$ ,  $J = J_e = 1$ ,  $D = D_e = 1$  and  $\alpha = 1.01$ .

lines, 2 lines and 6 lines, whereas for the 21 line stripe the new stripes are 10 lines, 2 lines and 7 lines.

### 3.4.2 Density of states

We see from above that the zigzag type stripes are gapless even when the lines of impurities are introduced. For analogous applications to zigzag graphene nanoribbons it has been found that the localized states at the Fermi level are very important [5, 33]. This motivated Nakada et al.[42] to use the density of states at the Fermi level and at the center band to study size effects in zigzag graphene ribbons. Here, we choose the following two quantities to study the effects of edges and impurities for zigzag stripes. The first is the relative density of states near the Fermi level (RDSFL), which computationally is calculated by finding the total number of

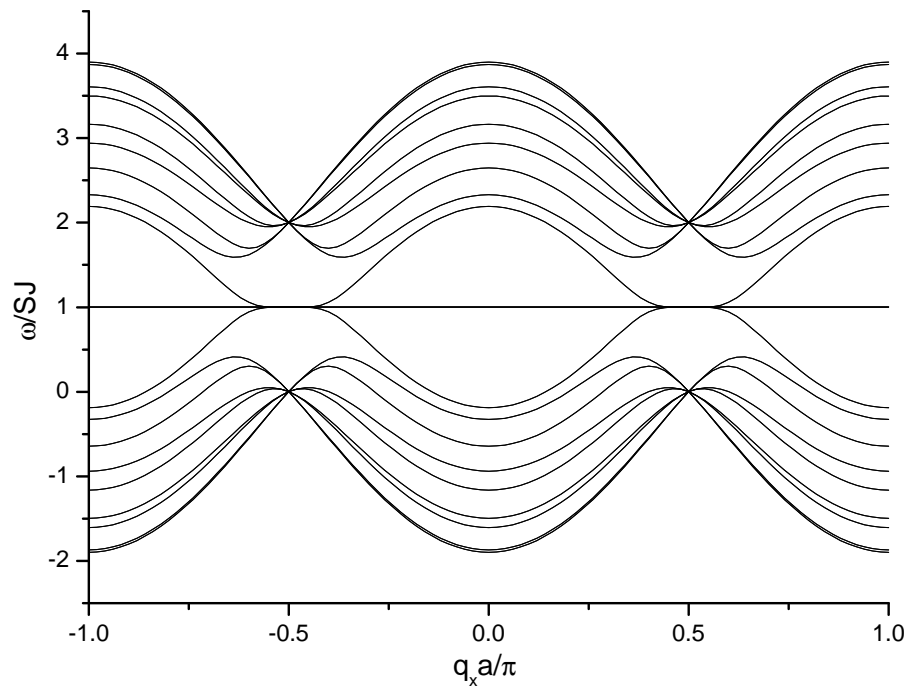


Figure 3.5: SW dispersion for zigzag ferromagnetic honeycomb stripes with an impurity line at line number 11, where  $N = 20$ ,  $J = J_e = 1$ ,  $J_l = 0.0J$ ,  $D = D_e = D_l = 1.0$  and  $\alpha = 1.01$ .

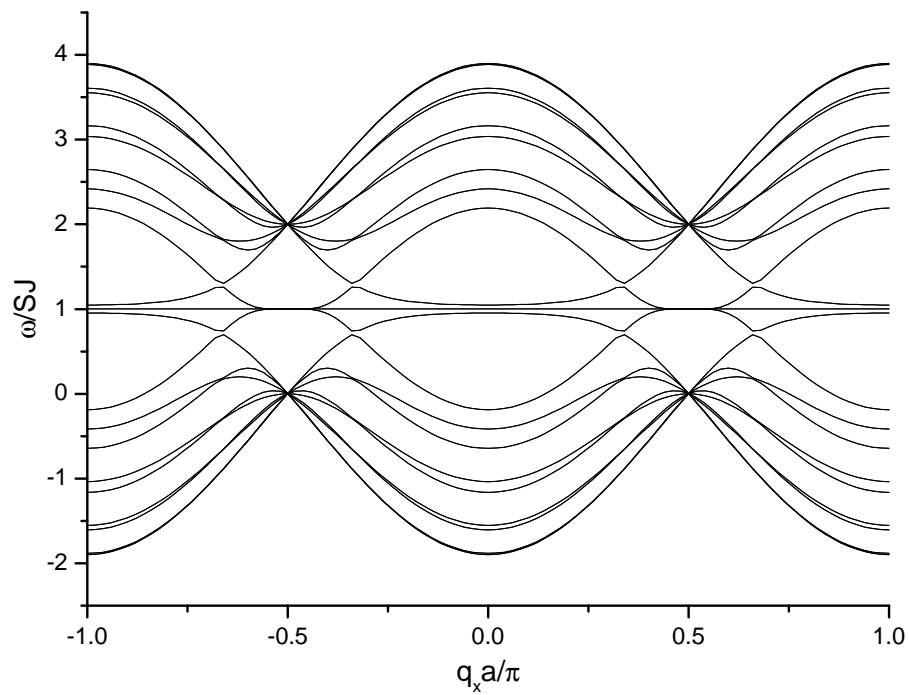


Figure 3.6: SW dispersion for zigzag ferromagnetic honeycomb stripes with an impurity line at line number 11, where  $N = 21$ ,  $J = J_e = 1$ ,  $J_l = 0.0J$ ,  $D = D_e = D_l = 1.0$  and  $\alpha = 1.01$ .

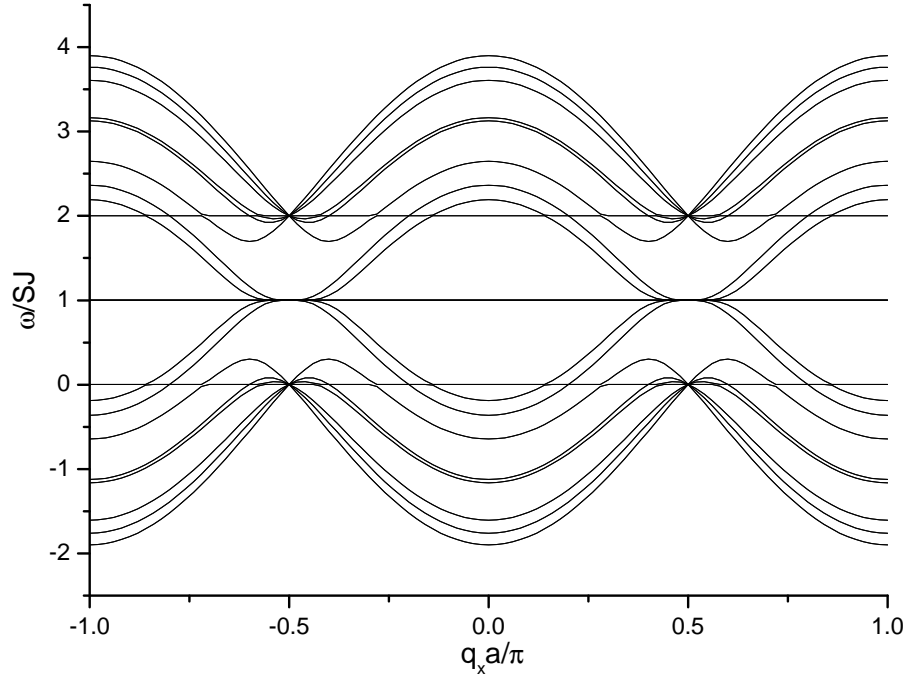


Figure 3.7: SW dispersion for zigzag ferromagnetic honeycomb stripes with two impurities lines at line number 11 and line number 14, where  $N = 20$ ,  $J = J_e = 1$ ,  $J_I = 0.0J$ ,  $J_{II} = 0.0J$ ,  $D = D_e = D_I = 1.0$  and  $\alpha = 1.01$ .

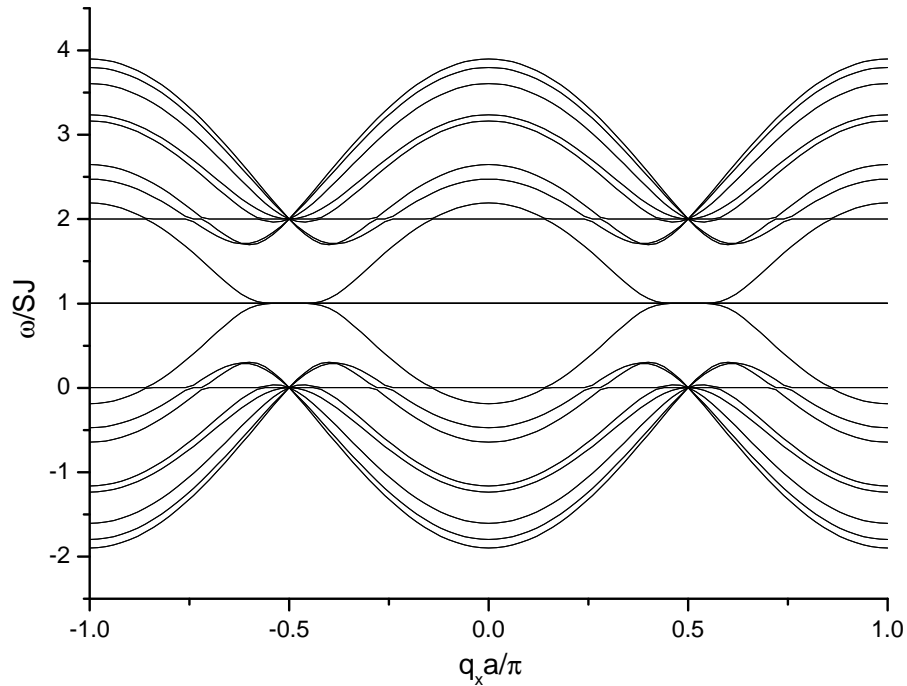


Figure 3.8: SW dispersion for zigzag ferromagnetic honeycomb stripes with two impurities lines at line number 11 and line number 14, where  $N = 21$ ,  $J = J_e = 1$ ,  $J_I = 0.0J$ ,  $J_{II} = 0.0J$ ,  $D = D_e = D_I = 1.0$  and  $\alpha = 1.01$ .

points in the dispersion relations for a very narrow range of values close to  $\alpha$ . Specifically, we find that choosing the range between  $\alpha - 0.0002$  and  $\alpha + 0.0002$  gives a good relative measure for the density of states at the Fermi level. The second quantity is the relative density of states of the center band (RDSCB), which computationally is calculated by the total number of points in the dispersion relations, again arbitrarily choosing a narrow range between  $\alpha - 1.0002$  and  $\alpha + 1.0002$ .

We start with the results in the absence of impurities. Figure 3.9 shows the effect of the

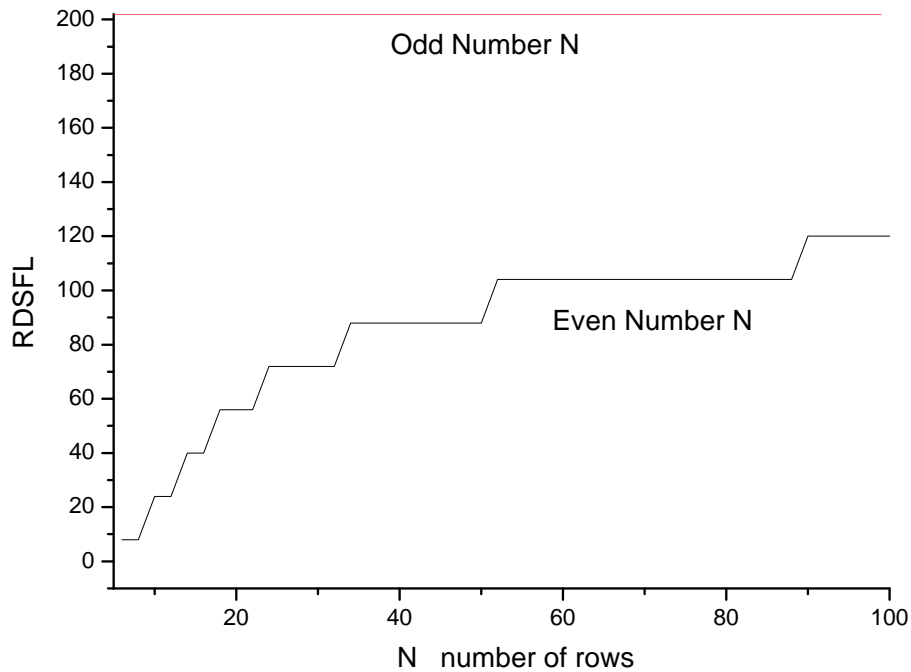


Figure 3.9: The effect of stripe width on the relative density of states near the Fermi level (RDSFL) in the zigzag case.

zigzag stripe width on RDSFL. In the case of odd  $N$ , the RDSFL is constant and independent of  $N$ . This is because of the large contributions of the localized edge states that extend over the entire Brillouin zone for edge sites with unit coordination number. For even  $N$  the RDSFL is dependent on the stripe width and increases stepwise with  $N$ . This behavior for even  $N$  is analogous to the results of Nakada et al.[42] for graphene zigzag ribbon.



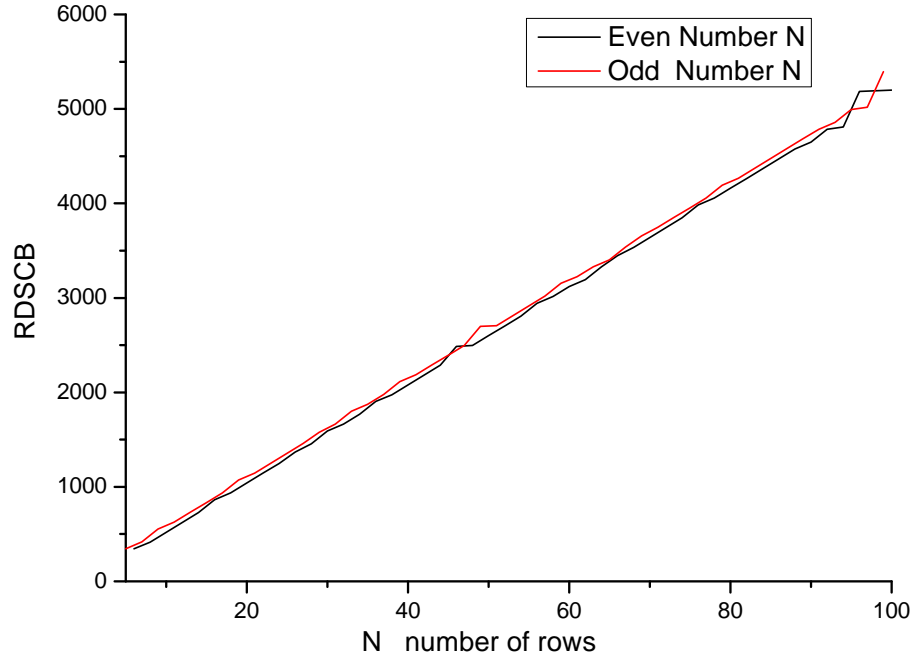


Figure 3.10: The effect of stripe width on the relative density of states of the center band (RDSCB) in the zigzag case.

Figure 3.10 shows the effect of zigzag stripe width on RDSCB. The odd RDSCB is almost equal to the even RDSCB, and it increases roughly linearly with the stripe width for both even and odd  $N$ .

While RDSFL typically becomes suppressed when we generalize to  $D_e \neq D$ , Figure 3.11 shows the color contour plot for the different effects of edge uniaxial anisotropy and zigzag stripe width on the RDSCB. The figure implies that RDSCB is independent of the change of edge uniaxial anisotropy. Also the RDSCB increases with increasing the stripe width like in Figure 3.10. Figure 3.12 shows the analogous color contour plot for the effects of edge exchange and zigzag stripe width on its RDSCB. It is clear that RDSCB decreases with an increase of the exchange. This decrease is particularly large in the edge exchange range from 0.5 to 1.0. Outside of the edge exchange range 0.5 to 1.0 the RDSCB depends mainly on the stripes width as reflected in parallel colored stripes.

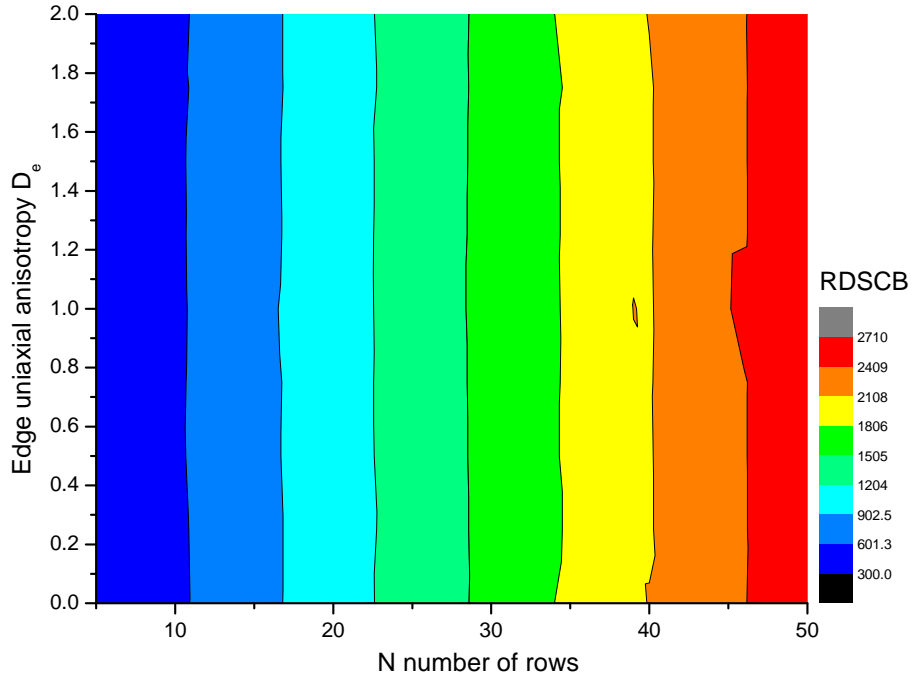


Figure 3.11: Contour plot for the effects of edge uniaxial anisotropy and zigzag stripe width on the RDSCB

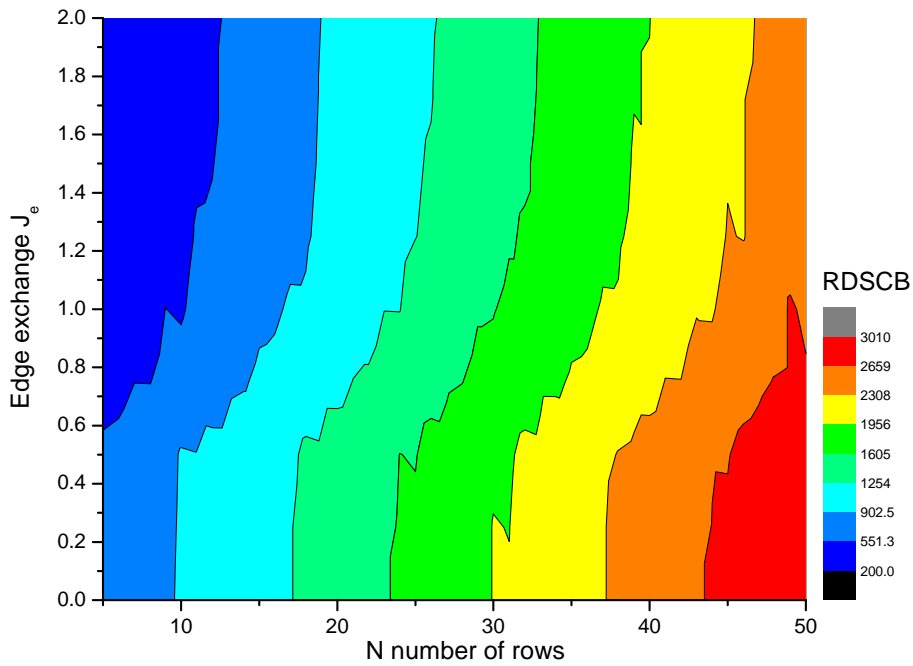


Figure 3.12: The effects of edge exchange and zigzag stripe width on the RDSCB

The study of magnetic impurity effects on zigzag stripes is important for applications. Here results are presented for the effects of introducing one and two lines of magnetic impurities on

zigzag 20 and 21 width stripes as regards their RDSFL and RDSCB. There are two parameters for the impurities. The first one is the strength of exchange  $J_I$  between the impurity line and the stripe material [39], and we take the range of values from 0 to 2 in units of  $J$ . The second parameter is the impurity line position, which can correspond to either even row number in sublattice B or odd row number in sublattice A (see Figure 3.1).

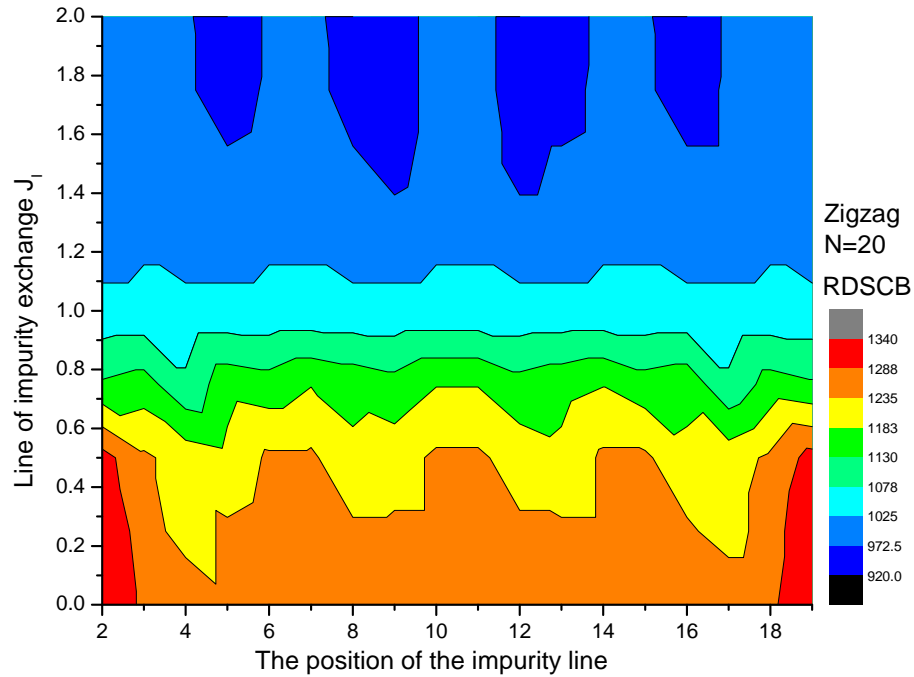


Figure 3.13: The effects of position and impurity exchange for  $N = 20$  zigzag stripe on the RDSCB in the case of one line of impurities.

The first case shown here is the introduction of one line of magnetic impurities on a zigzag 20 width stripe. The results show that RDSFL is nearly independent of the position of the impurity line and its exchange value except when  $J_I = 0$  which is similar to the edge exchange effect. Since edge localized states at the Fermi level depend mainly on the edge geometry and the width of the zigzag stripes, we may conclude that the above behavior is related to the geometries and the widths of the zigzag sub stripes and their interaction. Figure 3.13 shows the effects of one line of impurities for a  $N = 20$  zigzag stripe on the RDSCB, beginning from

impurities exchange with the value 1.0 and then larger. As the impurities exchange increases, the RDSCB decreases. As it reaches 1.4 the RDSCB decreases more at the line of impurities positions 9 and 12. For the impurities exchange between 1.6 to 2, the RDSCB decreases more at the line of impurities positions 5, 8, 9, 12, 13 and 16. As the impurities exchange decreases below 1.0, the RDSCB changes and shows features at particular lines.

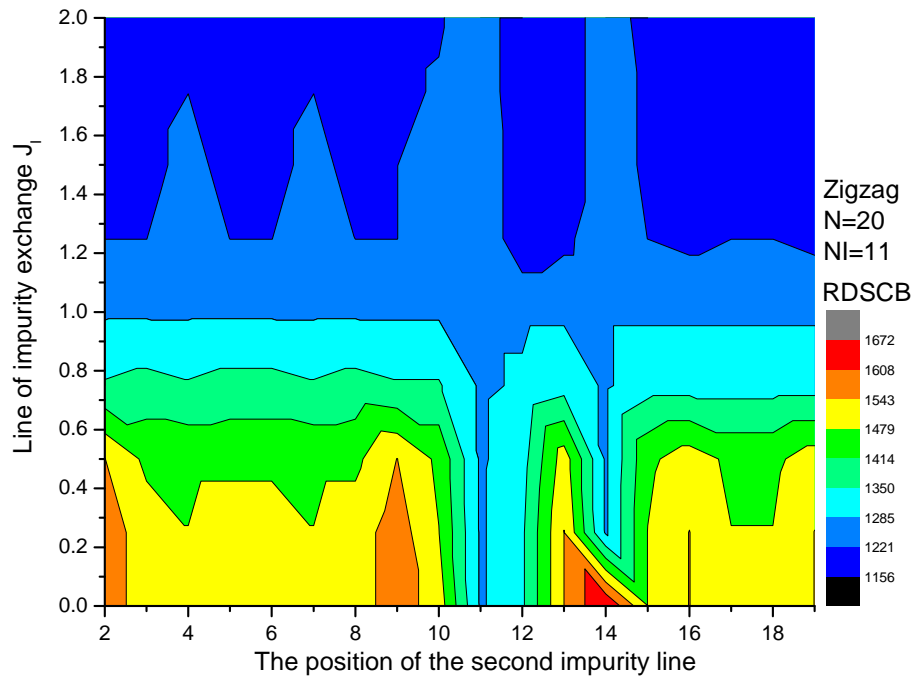


Figure 3.14: The effect of a second line of impurities position and impurities exchange on the RDSCB for a  $N = 20$  zigzag stripe. There is one line of impurities at  $N = 11$  with impurities exchange  $J_I = 0$ .

The addition of a second line of impurities to the zigzag stripe increases the possibility to tune the magnetic properties of the stripes to suit expected devices applications. Figure 3.14 shows the effects of a second line of impurities position and its impurities exchange on the RDSCB of a  $N = 20$  zigzag stripe. The results for the effects of a second impurities line show that RDSFL is nearly independent of the position of the second impurities line and its impurities exchange value except when  $J_{II} = 0$  which is similar to the cases of one impurities

line and the edge exchange.

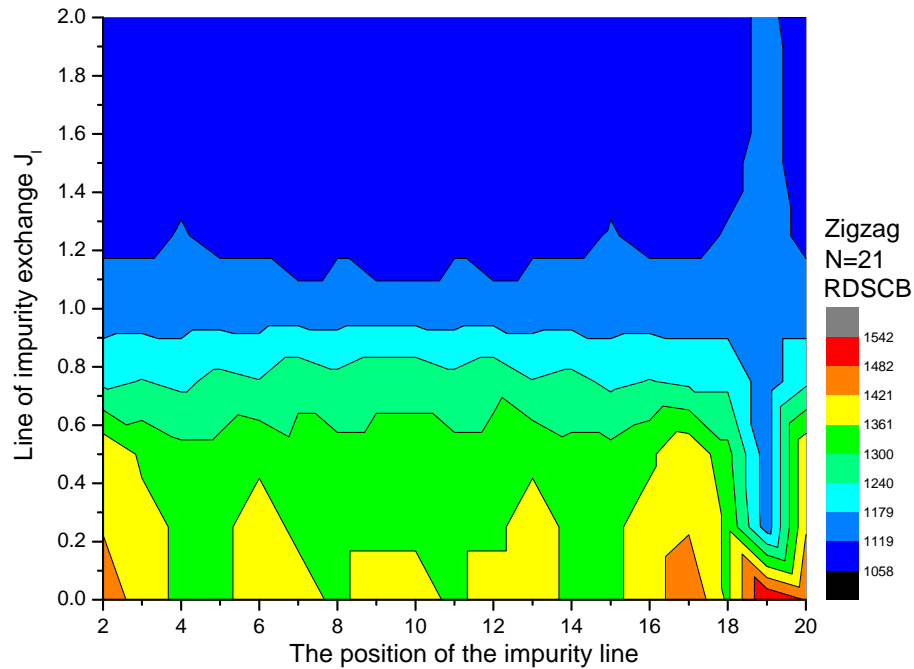


Figure 3.15: The effect of one line of impurities position and impurities exchange for a  $N = 21$  zigzag stripe on its RDSCB

The corresponding results for the effects of one impurities line for a  $N = 21$  zigzag stripe show that RDSFL is nearly independent of the position of the impurities line and its impurities exchange value except when  $J_I = 0$  which is similar to previous cases.

Figure 3.15 shows the effects of one line of impurities position and impurities exchange for a  $N = 21$  zigzag stripe on its RDSCB, beginning from impurities exchange with the value 1.0 which mean no impurities. As the impurities exchange increases the RDSCB mostly decreases until the impurities exchange reaches 1.2, except for a different behavior when the line of impurities is near the edge at position 19. As the impurities exchange decreases below 1.0, the RDSCB increases gradually in most cases. At impurities line positions 2 and 17 there are pronounced increases in RDSCB at very small impurities exchange. The line position 19 has a special RDSCB behavior due to the formation of a sub stripe with two lines. This creates two

localized states: one in the conduction band and the other in the valence band.

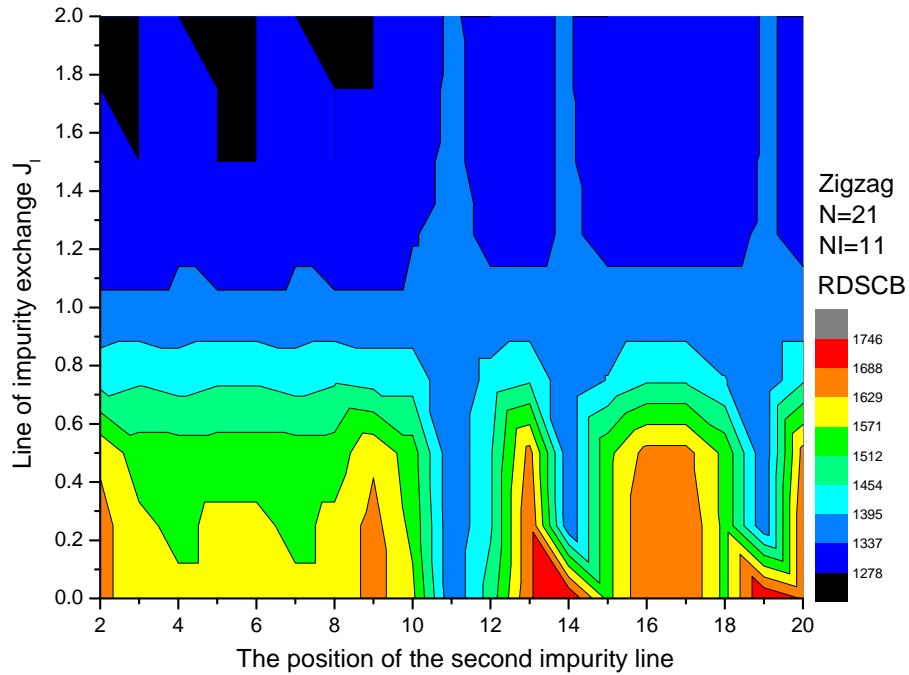


Figure 3.16: The effect of a second line of impurities position and impurities exchange for a  $N = 20$  zigzag stripe with one line of impurities at  $N = 11$  with impurities exchange  $J_I = 0$  on its RDSCB

The effects of a second impurities line in terms of its position and impurities exchange  $J_{II}$  were studied for  $N = 21$  zigzag stripe with the first line of impurities at position 11. The results show that RDSFL is nearly independent of the position of the second impurities line and its impurities exchange value except when  $J_{II} = 0$  which is similar to some cases before. Finally Figure 3.16 shows analogous effects of a second line of impurities on the RDSCB. As the impurities exchange of the second line is varied from 1.0 (either upwards or downwards), specific features appear that are associated with particular line positions, as seen in the Figure.

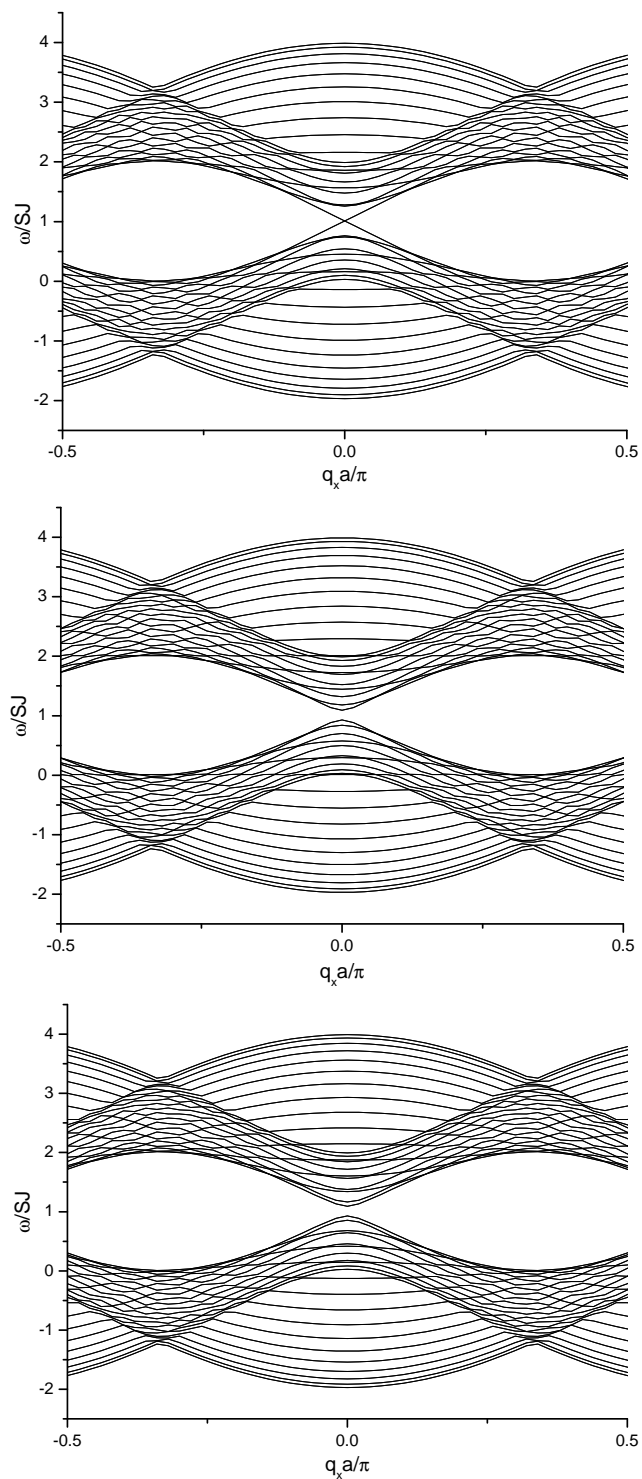


Figure 3.17: SW dispersion for armchair 2D Heisenberg ferromagnetic honeycomb stripes with  $J = J_e = 1.0$ ,  $D = D_e = 1.0$ , and  $\alpha = 1.01$  for  $N = 20, 21$  and  $22$  respectively.

## 3.5 SW results for armchair stripes

### 3.5.1 SW dispersion relations

Figures 3.17 show the dispersion relations for three armchair stripes with widths 20, 21, and 22. When the NN exchange has a constant value  $J$  through all the stripe including the stripe edges and likewise for the uniaxial anisotropy term, the obtained dispersion relation is very close to that for armchair graphene ribbons with the same size [39], except that the dispersion curves here are shifted due to the  $\alpha$  effect.

It is clear that the shape of the dispersion relations for armchair stripes depends on the stripe width. In general, the minimum of the conduction band and the maximum of valence band are located at  $q_x = 0$  for each stripe. In a 20 lines stripe they touch each other at the Dirac point, while for  $N = 21$  and 22 stripes they have different band gaps. This behavior is well known in the analogous graphene armchair ribbons [117, 39]. This repeated pattern of the dispersion relations for armchair stripes can be described mathematically in terms of periodic behavior in the number of lines as  $3i$  and  $3i + 1$  for stripes with band gaps while  $3i + 2$  corresponds to gapless stripes where  $i = 1, 2, 3, \dots$ . The origin of this behavior is understood as consequence of the topologically ladder system nature for armchair geometry, specifically cyclic chains with interchain hopping [42, 117, 118, 40, 119, 120, 121].

In the armchair geometry the sites from sublattice A are in the same line as sites from sublattice B, which is not the case in zigzag stripes. This affects the symmetry between lines and eliminates the degeneracy in armchair stripes without impurities [39]. There is no localized edge state found in armchair stripes without impurities which is similar to the case of graphene [40, 42, 39].



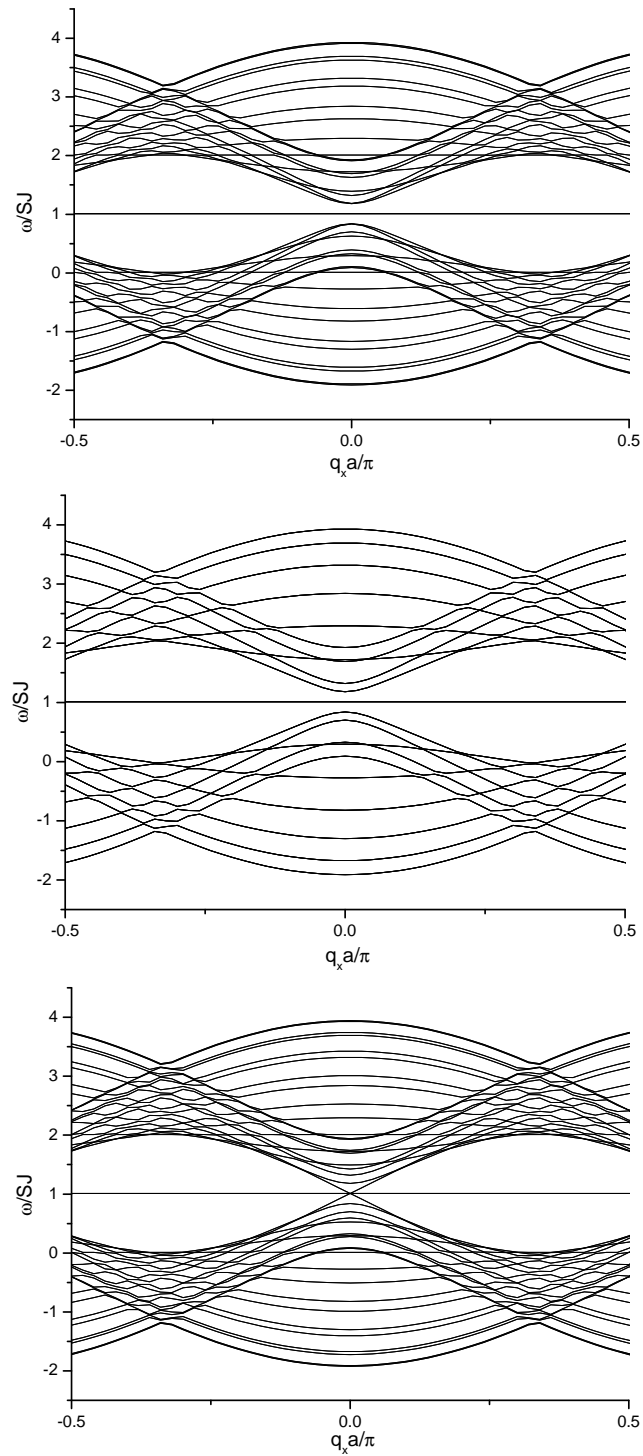


Figure 3.18: SW dispersion for armchair 2D Heisenberg ferromagnetic honeycomb stripes with an impurity line at line number 11, where  $J = J_e = 1$ ,  $J_l = 0.0J$ ,  $D = D_e = D_l = 1.0$  and  $\alpha = 1.01$  for  $N = 20, 21$  and  $22$  respectively.

Figures 3.18 show the modified dispersion relations due to the effect of introducing a magnetic impurities line at row 11 of the armchair stripes with 20, 21, and 22 lines. Again as in the case of magnetic zigzag stripes the new dispersions with impurities line for armchair magnetic stripes show the same behavior seen in the same case for armchair graphene ribbons [39], but shifted in the case of magnetic stripes due the  $\alpha$  effect. The introduction of the impurities line has the analogous effect as in the case of zigzag stripes which is splitting the stripe into two interacting stripes with different sizes. In the case of a 20 line stripe the new stripes are 10 lines and 9 lines, in the case of a 21 line stripe the new two stripes each 10 lines which lead to a completely degenerate dispersion, and finally in the case of a 22 line stripe the two new stripes are 10 lines and 11 lines. The strength of the interaction between the two sub stripes depends on the value of  $J_l$ . The figures here show the case when  $J_l = 0$ , for which the expanded edge localized states in the Fermi level are analogous to the case of zigzag stripes. Figures 3.19 show the modified dispersion relations due to the effect of introducing magnetic impurities lines at rows 11 and 14 of the armchair stripes with 20, 21 and 22 lines. Again, we see here the effect of splitting the stripe into three interacting stripes with different sizes.

### 3.5.2 Density of states

We see from the results above that armchair type stripes have band gaps while there are no intrinsic localized edge states, so the energy band gap is very important [5, 33, 39]. Therefore RDSCB and the change in the band gap are relevant parameters. Figure 3.20 shows the effect of the armchair stripe width on its RDSCB, which is highly dependent on the armchair stripe width type as  $3i$ ,  $3i+1$ , and  $3i+2$ . There is a repeated pattern between the stripe width  $N$  and their RDSCB in accordance with this sequence. Overall, the average value of the RDSCB

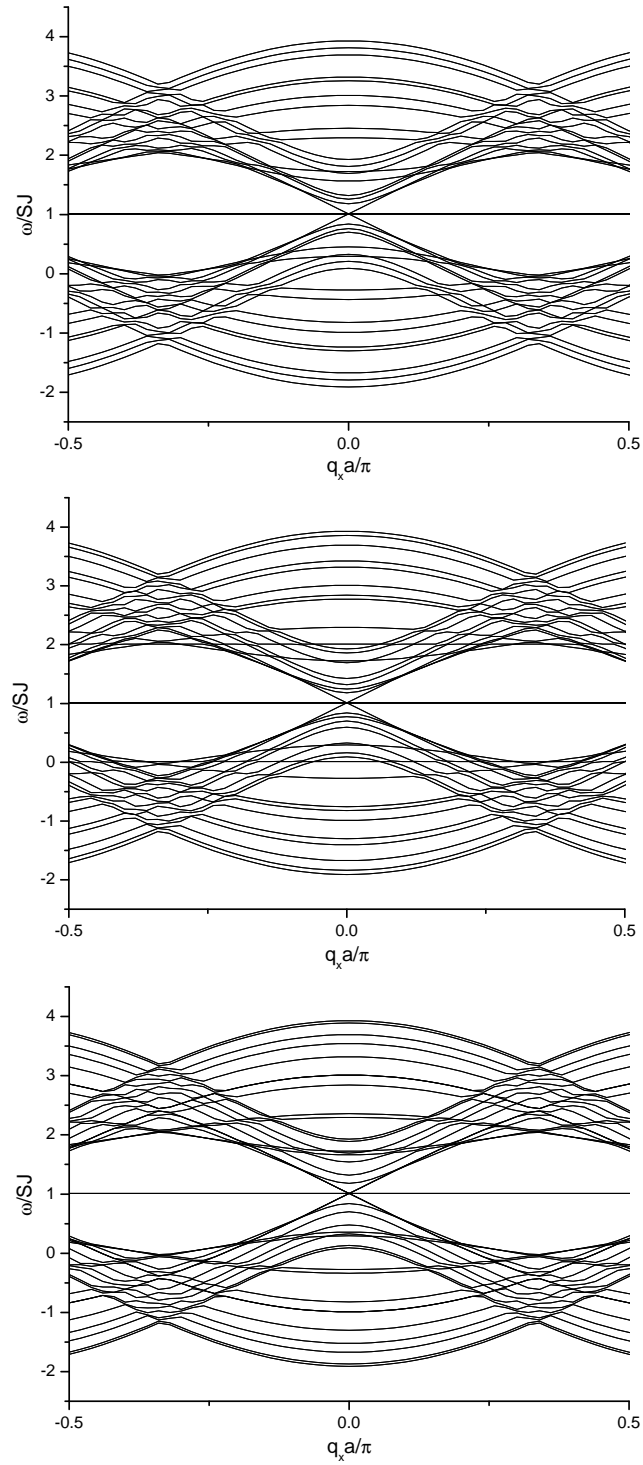


Figure 3.19: SW dispersion for armchair 2D Heisenberg ferromagnetic honeycomb stripes with an impurity lines at line number 11 and line number 14, where  $J = J_e = 1$ ,  $J_I = J_{II} = 0.0J$ ,  $D = D_e = D_I = 1.0$  and  $\alpha = 1.01$  for  $N = 20, 21$  and  $22$  respectively.

linearly increases with increasing stripe width.

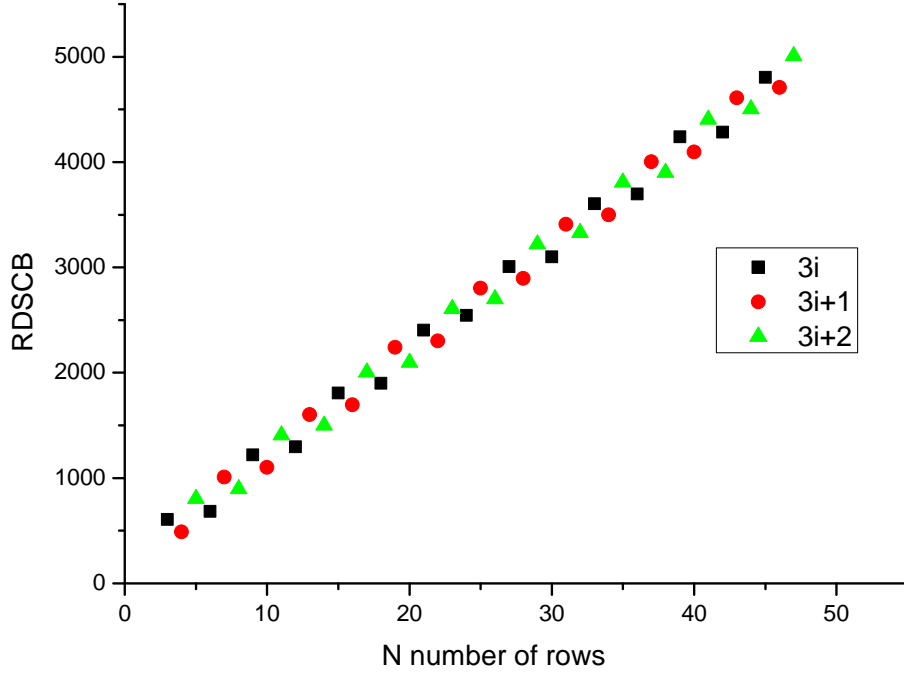


Figure 3.20: The effect of armchair stripe width for the three armchair types on the relative density of states of center band (RDSCB)

Figure 3.21 shows the color contour plot for the effects of edge uniaxial anisotropy and armchair stripe width on the RDSCB. The RDSCB is seen to be nearly independent of the edge uniaxial anisotropy except at  $D_e = D$  where there are certain stripe widths with higher values of RDSCB than that at the surrounding numbers, which is seen here for the first time in armchair stripes. In general, changing the edges insite energy breaks the symmetry of the dispersion relation and slightly moves the Fermi Level which also seen in graphene nanoribbons [118], while having almost no effect on the RDSCB value. It is clear that RDSCB increases with increasing the stripe width which agrees with Figure 3.20.

Figure 3.22 shows the color contour plot for the effects of edge exchange and zigzag stripe width on the RDSCB. It is clear that RDSCB is decreasing with the increasing of the edge exchange which gives rise to a curvature in the colored bands. The RDSCB increases with

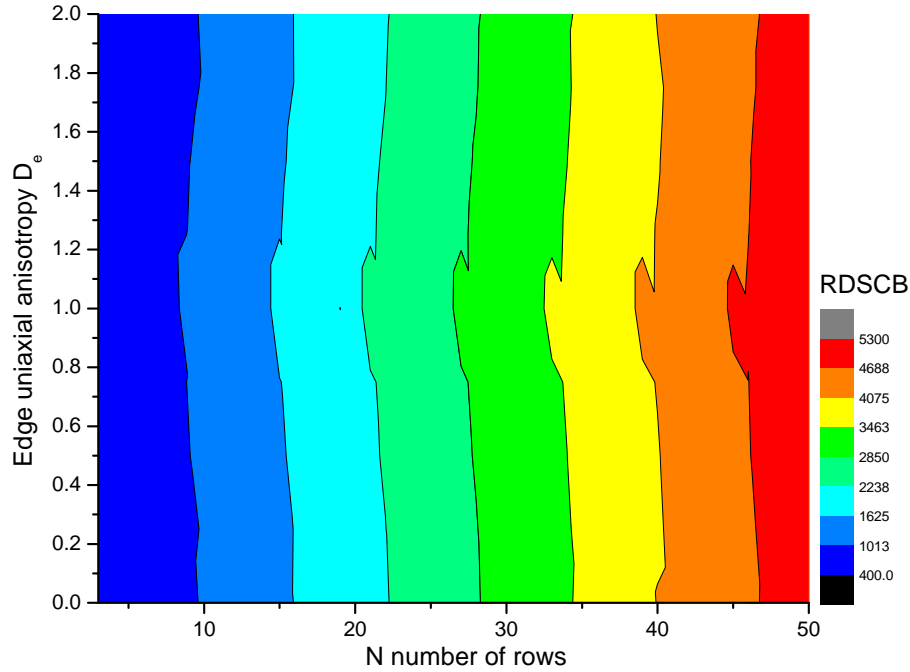


Figure 3.21: The effects of edge uniaxial anisotropy and armchair stripe width on its RDSCB

increasing the stripes width which agree with result in figure 3.20.

The study of magnetic impurities on armchair stripes is also important. As before, we consider introducing one and two lines of magnetic impurities on 20, 21 and 22 width stripes on their RDSCB. As in the zigzag case, there are the same two parameters for the impurities.

Figure 3.23 shows the effects of one line of impurities for  $N = 20$  and  $N = 22$  armchair stripes on their RDSCB. The figure shows that the behavior of the RDSCB is nearly the same for both even width stripes, beginning from the impurities exchange with value 1.0. Then as the impurities exchange increases the RDSCB decreases and it is independent on the impurity line position. As the impurities exchange decreases below 1.0, the RDSCB increases until the impurities exchange reaches zero and the RDSCB has maximum value irrespective of the impurity line position.

Figure 3.24 shows the effect on the RDSCB of a second impurities line position with im-

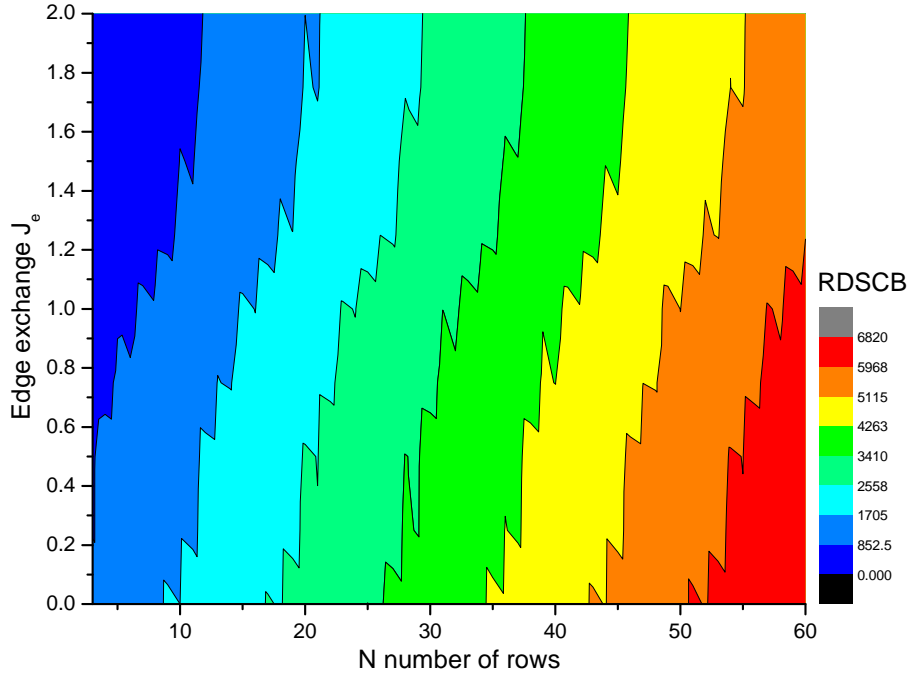


Figure 3.22: The effects of edge exchange and zigzag stripe width on its RDSCB

purities exchange  $J_{II}$  for  $N = 20$  and  $N = 22$  armchair stripes with one line of impurities fixed at  $N = 11$  and exchange  $J_I = 0$ . The behavior of the RDSCB is nearly the same for both even width stripes as the RDSCB is dependent on the position of a second impurities line with respect to the position of first impurities line. This can be understood in terms of the different ways in which two lines of impurities subdivide the full stripe width  $N$ .

The direct energy band gap seen above at  $q_x = 0$  in the armchair stripes is similar to the graphene armchair behavior and it is very important from the applications point of view [5, 33, 39]. The analogous relations between the graphene armchair nanoribbon types, the width and the band gap have been studied extensively both experimentally [122] and theoretically [123, 118, 41, 40, 42].

We have used our model to study the variation of bandgaps of the three types of magnetic armchair stripes as a function of width (number of rows) and some results are shown in Figure

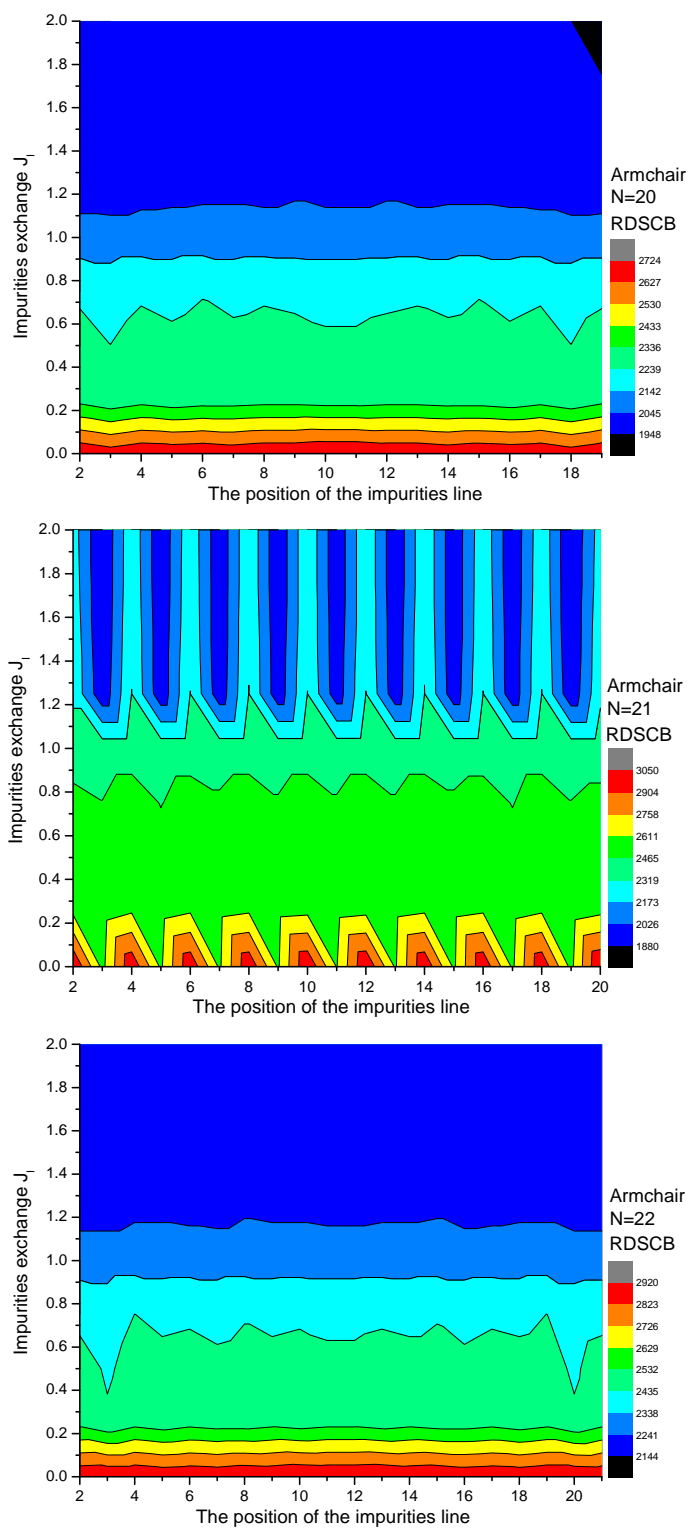


Figure 3.23: The effect of one line of impurities position and impurities exchange on the armchair stripe RDSCB for stripes width  $N = 20, 21$  and  $22$  respectively.

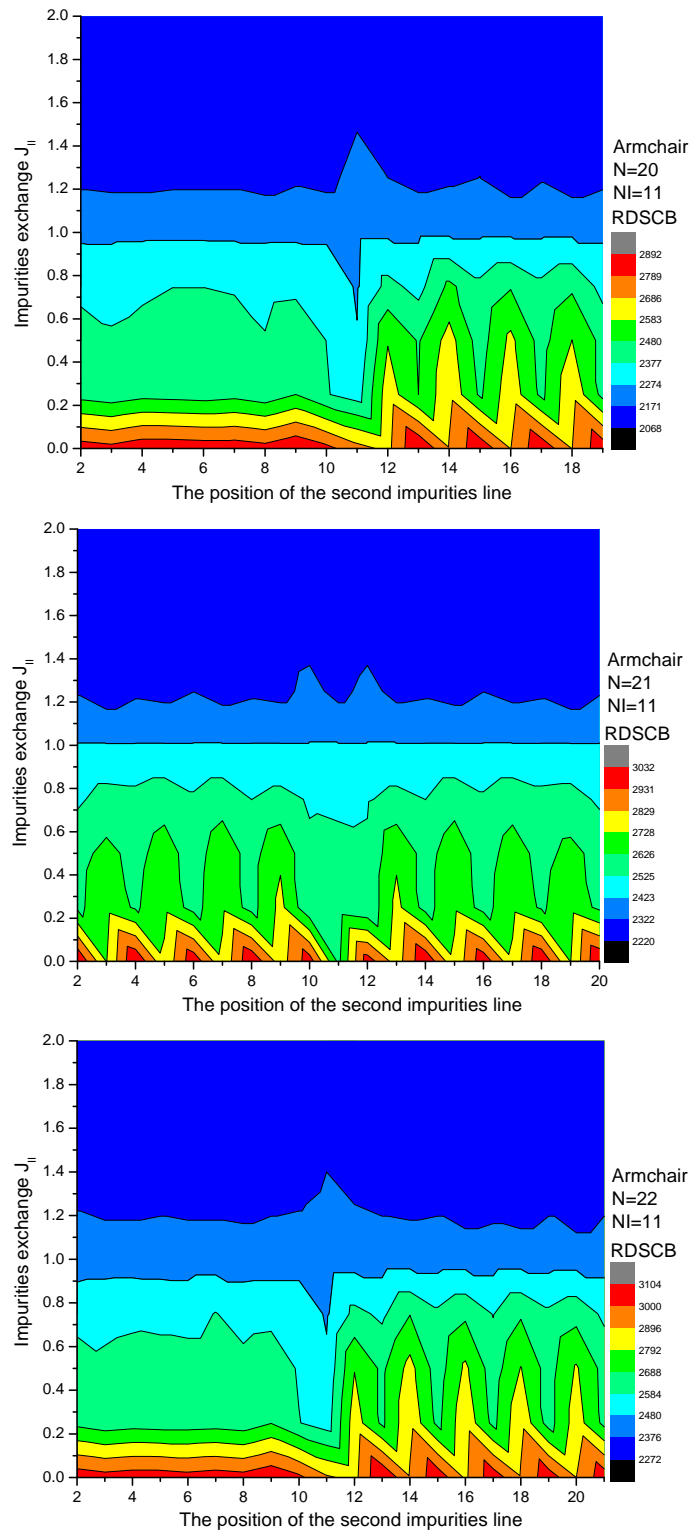


Figure 3.24: The effect of a second line of impurities position and impurities exchange on the armchair stripe RDSCB with one line of impurities at  $N = 11$  with impurities exchange  $J_I = 0$  for stripes width  $N = 20, 21$  and  $22$  respectively.



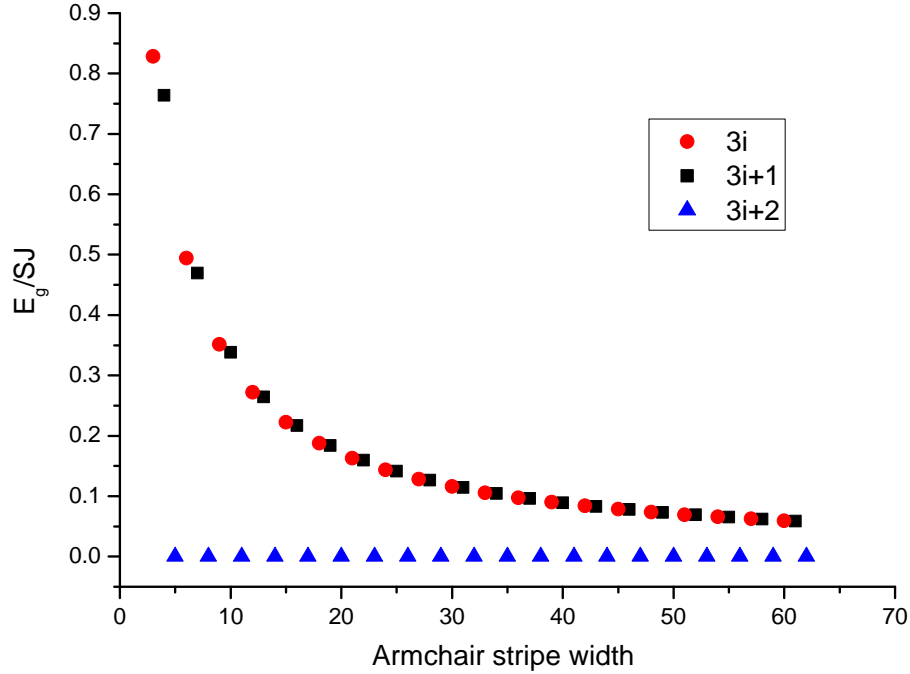


Figure 3.25: The variation of bandgaps of the three types of armchair stripes as a function of width (number of rows)  $W$

3.25, which shows that the energy band gap  $E_g$  for armchair types  $3i$  and  $3i+1$  have essentially the same width  $W$  dependence as seen in graphene armchair nanoribbons, i.e.  $E_g \sim W^{-1}$ .

In our study of width effect on the energy band gap of magnetic armchair stripes, we assumed for convenience that the edges sites have the same exchange as interior sites, i.e.  $J_e = J$ , but this is not always the case, as edges sites have different coordination number and symmetry. Consequently, just as it is found in the armchair graphene nanoribbons case that the edges play an important role in their energy band gap [123], the same is expected for magnetic stripes. Figure 3.26 shows the variation of the energy gap, which is the difference between the minimum conduction band mode and the maximum valence band mode in the stripe, against the strength of the edge exchange for  $N = 20, 21$  and  $22$  armchair stripes.

Introducing impurities in armchair stripes also modifies their energy bands. Figure 3.27 shows, as in the case of edge exchange, the variation of the energy gap versus the strength of

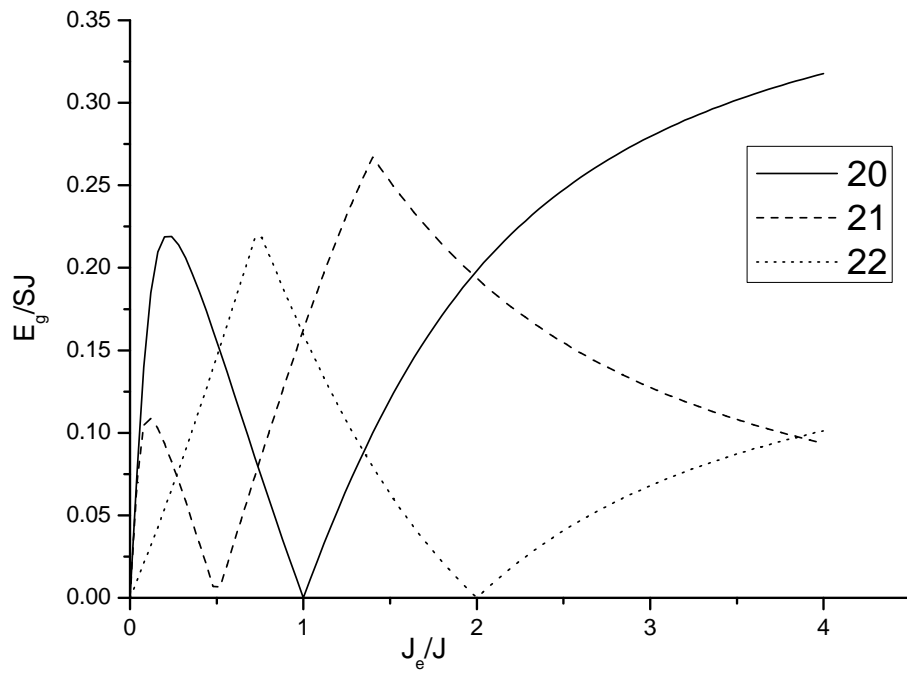


Figure 3.26: Variation of the energy gap versus the strength of the edge exchange for armchair stripes. The solid line is for a 20-line ribbon, dashed line for 21 lines, and dotted line for a stripe with 22 lines.

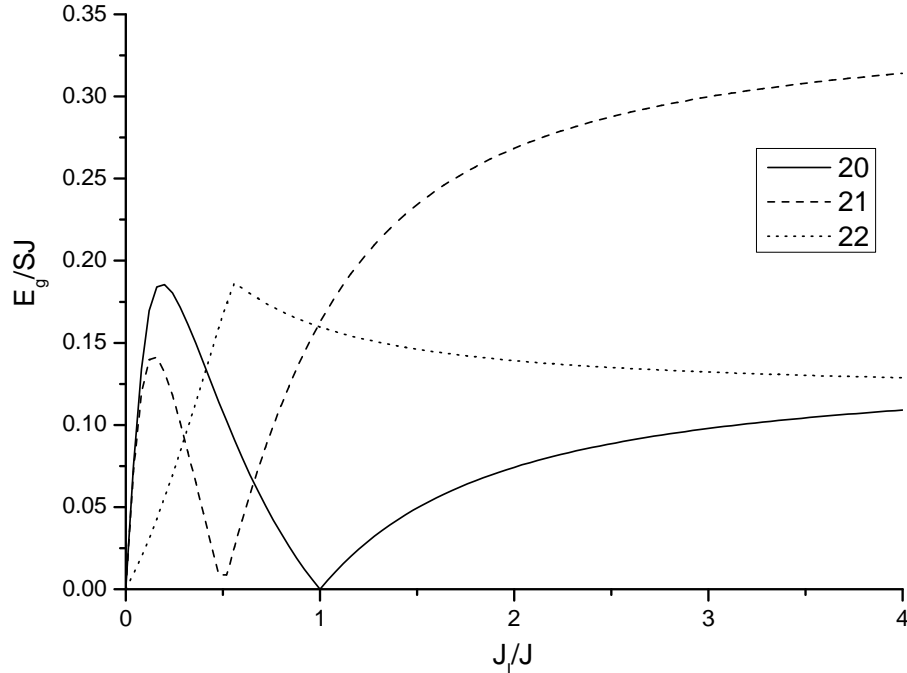


Figure 3.27: Variation of the energy gap versus the strength of the impurity exchange when the impurities line is in the 11th line of armchair stripes. The solid line is for a 20-line stripe, dashed line for 21 lines, and dotted line for a stripe with 22 lines.

the impurities exchange for  $N = 20, 21$  and  $22$  armchair stripes. The energy band gap in each case starts from zero and increases to reach a maximum, above which there is an oscillatory pattern of behavior (except in the case of  $N = 22$ ).

## 3.6 Discussion and Conclusions

In this chapter, the Heisenberg Hamiltonian with a ferromagnetic NN exchange was used to study the allowed SWs stripes with a 2D honeycomb lattice, generalizing results in Chapter 3 for 2D ferromagnets with a square lattice. The results of this study for the honeycomb lattice stripes show close parallels with the results of graphene nanoribbons described by a tight binding Hamiltonian for electronic short range interactions between carbons atoms represented by NN hopping. From a technological point of view, these results are very encouraging with regards fabricating a magnetic counterpart to graphene, which could lead to new advances especially in the field of spintronic devices and other magnetic applications.

We have found it convenient to utilize the direct diagonalization method which was discussed in Chapter 2 but is here extended to analyze the honeycomb lattice structure. The method has enabled us to highlight the strong differences between the cases of zigzag and armchair edges. Also we have presented results for the SW dispersion relations and associated density of states appropriate to the two edge geometries.

# Chapter 4

## Localized States in Semi-Infinite Zigzag Edged Graphene

### 4.1 Introduction

We saw in the previous chapter for magnetic materials that zigzag edged nanoribbons with a honeycomb lattice structure have characteristic flat localized edge states at the equivalent of the Fermi level. These types of edge states are known to be important for Zigzag Graphene Nanoribbons (ZGNR) [5, 33]. The edge localized states are, in general, dependent upon the ribbon size and purity of the sample [124] as we saw by analogous magnetic examples in Chapter 3. From a theoretical point of view, the edges states in graphene depend on the probability for an electron to hop from a site in the edge to a bulk site, or there may be hopping to an impurity site in the neighborhood. The edge atoms have a different coordination number from the bulk atoms, and this can lead to a different hopping parameter between the edge atoms and the bulk ones. Such a difference was not usually considered in previous calculations for ZGNR edge localized states with different approaches [42, 41, 40, 33], and these previous calculations typically show inconsistencies with experimental results for fabricated GNRs that exhibit semiconductor behavior [125, 5].

In Chapter 2 for square-lattice magnetic ribbons or stripes we found that the tridiagonal matrix method has an important advantage in studying the properties of the localized edge states due to its ability to distinguish clearly between the edge modes and area modes in the case of the 2D square lattice.

Therefore in this chapter, the tridiagonal matrix method will be extended to study the effect of edge sites on the localized edge states of semi-infinite zigzag 2D honeycomb sheets of graphene. Some formal similarity between semi-infinite ZGNR and semi-infinite antiferromagnetic materials, with both being two-sublattice structures, will guide us to follow the tridiagonal method as used previously in studying the surface modes of Heisenberg antiferromagnets [126, 127]. This matrix method also allows us to study the effect of impurities introduced substitutionally and we will show that this gives rise to additional localized states of the semi infinite ZGNR.

## 4.2 Theory for edge states and impurity states

The structure of semi-infinite ZGNR is a honeycomb lattice of carbon atoms with two sublattices denoted as  $A$  and  $B$ . The geometry of a graphene nanoribbon with zigzag edges is shown in Figure 4.1, where the system is infinite in the  $x$  direction whereas it has  $2N$  rows of carbon atoms in the  $y$  direction. To be considered as a ribbon,  $N$  is a finite integer but here we will extend the formalism of Chapter 2 to study the two-sublattice graphene structure for the semi-infinite case where  $N \rightarrow \infty$ . We are therefore considering fairly wide ribbons (e.g., with  $N$  greater than about 50 typically). The  $A(B)$  sublattice type lines are labeled with index  $n(n')$  where  $n(n') = 1, 2, 3, \dots$ . The edge of the semi-infinite structure corresponds to line index 1. The impurities (which may be silicon or boron, for example) are introduced substitutionally

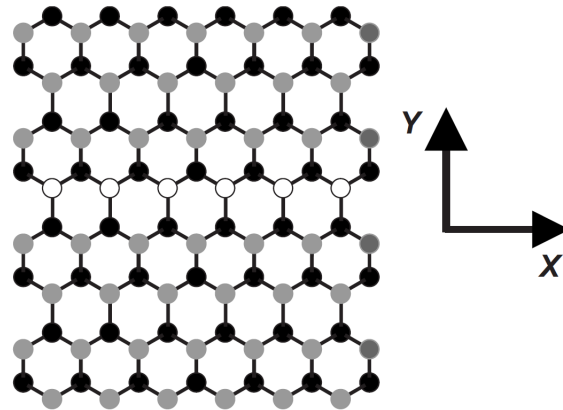


Figure 4.1: Geometry of a graphene ribbon with zigzag edges. The black (gray) dots are the sublattice  $A$  ( $B$ ) atoms, where  $A(B)$  sublattice type are labeled by index  $n(n')$  ( $= 1, 2, \dots, N$ ) and the white dots show a row of impurities. Figure taken from [39].

along one or two different rows of atoms parallel to the  $x$  axis, as required. The impurity lines, which preserve the translational symmetry in the  $x$  direction, may be any distance apart in the ribbon.

Table 4.1: NN hopping matrix elements for the zigzag graphene nanoribbon

Parameter	Zigzag
$\beta$	$2t \cos(\sqrt{3}q_x a/2)$
$\gamma$	$t$

Using a microscopic approach in terms of a tight binding model Hamiltonian (1.31) and neglecting NNN interactions at this stage, we follow the approach in some recent work for impurities in graphene ribbons [127]. The Hamiltonian becomes

$$H = - \sum_{i,j} t_{ij} (a_i^\dagger b_j + a_i b_j^\dagger) \quad (4.1)$$

where  $a_i^\dagger$  (or  $a_i$ ) creates (or annihilates) an electron on the sublattice  $A$  site, and  $b_j^\dagger$  (or  $b_j$ ) does the same for the sublattice  $B$  site, while  $t_{ij}$  is the NN hopping energy between sublattices. In the pure material the hopping energy is denoted by  $t$  and its value is known [33] to be  $\approx 2.8$  eV.

Taking into account the translational symmetry in the  $x$  direction, a Fourier transform is made to rewrite Equation (4.1) in a wavenumber representation  $q_x$  in the  $x$  direction, and the rows are labeled  $n$  and  $n'$ . The Hamiltonian becomes

$$H = \sum_{q_x, nn'} \left[ \tau_{nn'}(q_x) a_{q_x, n} b_{q_x, n'}^\dagger + \tau_{nn'}(-q_x) a_{q_x, n}^\dagger b_{q_x, n'} \right]. \quad (4.2)$$

The hopping amplitude factors  $\tau_{nn'}(q_x)$  for the zigzag structure have the form

$$\tau_{nn'}(q_x) = t \left[ 2 \cos \left( \frac{\sqrt{3}}{2} q_x a \right) \delta_{n', n} + \delta_{n', n \mp 1} \right], \quad (4.3)$$

or

$$\tau_{nn'}(q_x) = \beta \delta_{n', n} + \gamma \delta_{n', n \mp 1}, \quad (4.4)$$

where the assignment of upper or lower signs depends on the sublattice type sequence for rows  $n$  and  $n'$  (e.g., see Appendix B). The definitions of  $\beta$  and  $\gamma$  are given Table 4.1. Now we use the equation of motion  $i\hbar dX/dt = [X, H]$  for any operator  $X$  taking the creation and annihilation operators of each row. Taking  $\hbar = 1$  and assuming that the modes have a time dependence like  $\exp[-i\omega(q_x)t]$ , we obtain  $2N$  coupled equations:

$$\begin{aligned} \omega(q_x) a_{q_x, n} &= \sum_{q_x, n'} \tau_{nn'}(-q_x) b_{q_x, n'}, \\ \omega(q_x) b_{q_x, n'} &= \sum_{q_x, n} \tau_{n'n}(q_x) a_{q_x, n}. \end{aligned} \quad (4.5)$$

Expanding and rearranging the Equations (4.5) (see Appendix B for details) we obtain coupled equations between sublattice  $A$  and sublattice  $B$  operators which can eventually be

written in the following form

$$\begin{aligned}
- a_{q_x, n-1} + \frac{\{\omega^2(q_x) - (\beta^2 + \gamma^2)\}}{\beta\gamma} a_{q_x, n} - a_{q_x, n+1} &= 0 \\
b_{q_x, n'} - \frac{\gamma}{\omega(q_x)} a_{q_x, n} - \frac{\beta}{\omega(q_x)} a_{q_x, n+1} &= 0.
\end{aligned} \tag{4.6}$$

Equations (4.6) could conveniently be rewritten as in the following supermatrix equation [126]

$$\begin{pmatrix} A_N + \Delta A_N & O_N \\ B_N & I_N \end{pmatrix} \begin{pmatrix} a_N \\ b_N \end{pmatrix} = 0, \tag{4.7}$$

where  $O_N$  is the null matrix,  $I_N$  is the identity matrix,  $a_N(b_N)$  are operator column matrices, and

$$A_N = \begin{pmatrix} \zeta & -1 & 0 & 0 & 0 & \dots \\ -1 & \zeta & -1 & 0 & 0 & \dots \\ 0 & -1 & \zeta & -1 & 0 & \dots \\ 0 & 0 & -1 & \zeta & -1 & \dots \\ \vdots & \vdots & \vdots & \vdots & \vdots & \ddots \end{pmatrix} \tag{4.8}$$

and

$$B_N = \begin{pmatrix} \eta & 0 & 0 & 0 & 0 & \dots \\ \lambda & \eta & 0 & 0 & 0 & \dots \\ 0 & \lambda & \eta & 0 & 0 & \dots \\ 0 & 0 & \lambda & \eta & 0 & \dots \\ \vdots & \vdots & \vdots & \vdots & \vdots & \ddots \end{pmatrix}, \tag{4.9}$$

where the elements of above matrices are defined by

$$\zeta = \frac{\{\omega^2(q_x) - (\beta^2 + \gamma^2)\}}{\beta\gamma}, \quad \eta = \frac{-\gamma}{\omega(q_x)}, \quad \lambda = \frac{-\beta}{\omega(q_x)}. \tag{4.10}$$





where the elements of  $\Delta A_N$  matrix are defined by

$$\begin{aligned}
\Delta_e &= \zeta_e - \zeta, & \Delta_s &= \frac{\beta\gamma - \beta_e\tau_e}{\beta\gamma}, & \zeta_e &= \frac{\{\omega^2(q_x) - (\beta_e^2 + \tau_e^2)\}}{\beta\gamma}, \\
\Delta_{n_0} &= \zeta_{n_0} - \zeta, & \Delta_{In_0} &= \frac{\beta\gamma - \beta_I\tau_I}{\beta\gamma}, & \zeta_{n_0} &= \frac{\{\omega^2(q_x) - (\beta_{n_0}^2 + \tau_{n_0}^2)\}}{\beta\gamma}, \\
\Delta_{n'_0} &= \zeta_{n'_0} - \zeta, & \Delta_{In'_0} &= \frac{\beta\gamma - \beta_{In'_0}\tau_{In'_0}}{\beta\gamma}, & \zeta_{n'_0} &= \frac{\{\omega^2(q_x) - (\beta_{n'_0}^2 + \tau_{n'_0}^2)\}}{\beta\gamma},
\end{aligned} \tag{4.12}$$

and the edge hopping  $t_e$ , the first impurities line hopping  $t_{n_0}$ , and the second impurities line hopping  $t_{n'_0}$  replace the ZGNR interior area sites hopping term  $t$  in the definitions of  $\beta$  and  $\gamma$  in

Table 4.1 to obtain the edge and impurities counterparts.

Following the analogous formal steps as in the Heisenberg antiferromagnetic case [126] and using the algebra of block matrices [89], one may now define the supermatrix  $G$  as

$$G = \begin{pmatrix} A_N & O_N \\ B_N & I_N \end{pmatrix}^{-1} = \begin{pmatrix} (A_N)^{-1} & O_N \\ -B_N(A_N)^{-1} & I_N \end{pmatrix}. \tag{4.13}$$

Using Equations (4.13) and Equation(4.7), we get the following

$$\begin{aligned}
(I_N + (A_N)^{-1}\Delta A_N)a_N &= 0 \\
(-B_n(A_N)^{-1}\Delta A_N)a_N + b_N &= 0
\end{aligned} \tag{4.14}$$

It is useful to now define the following matrix

$$D_N = I_N + (A_N)^{-1}\Delta A_N \tag{4.15}$$

which can next be written in the following partitioned form (see Appendix C for details)

$$D_N = \left( \begin{array}{c|c} Q & O \\ \hline S & I \end{array} \right), \quad (4.16)$$

where  $O$  is a square null matrix,  $I$  a square identity matrix,  $S$  a square submatrix of  $D_N$ , and  $Q$  is a square submatrix of  $D_N$  with dimension of  $n'_0 + 1 \times n'_0 + 1$ .

The elements for the inverse of the tridgional matrix  $A_N$  [84, 85, 86, 126, 87] are now known to be (see also Chapter 2)

$$((A_N)^{-1})_{nm} = \frac{x^{n+m} - x^{|n-m|}}{x + x^{-1}}, \quad (4.17)$$

where  $x$  is a complex variable such that  $|x| \leq 1$  and  $x + x^{-1} = \zeta$ . As mentioned at the analogous step in Chapter 2, the values of  $x$  should satisfy the following boundary and physical conditions [62]. The area modes are oscillating waves inside the nanoribbon, which requires that  $x$  must be an imaginary exponential  $x = e^{iq_y a/2}$  with  $|x| = 1$ . From the definition of  $\zeta$  and  $x$  parameters, the dispersion relation for the band of area modes is given by

$$\begin{aligned} \zeta &= x + x^{-1} = e^{iq_y a/2} + e^{-iq_y a/2} = 2 \cos(q_y a/2) \\ &= \frac{\{\omega_B^2(q_x, q_y) - (\beta^2 + \gamma^2)\}}{\beta\gamma} \\ \omega_B(q_x, q_y) &= \pm t \sqrt{1 + 4 \cos^2\left(\frac{\sqrt{3}q_x a}{2}\right) + 4 \cos\left(\frac{q_y a}{2}\right) \cos\left(\frac{\sqrt{3}q_x a}{2}\right)} \end{aligned} \quad (4.18)$$

This latter expression for the 2D area band for the zigzag nanoribbons is formally very similar to the infinitely-extended graphene electronic dispersion relation given in Equation 1.29 and shown in Figure 1.7. Therefore this expression also shows the same general features of the graphene band structure as we discussed earlier.

By contrast, the localized edge modes decay exponentially with distance inside the nanoribbon, which requires that  $x$  must be real and less than 1 for edge modes. The edge modes are obtained here by requiring the determinant of the coefficients for the  $a_n$  operator column vector to vanish [126, 62, 88]:

$$|D_N| = \det \left[ \left( \begin{array}{c|c} Q & O \\ \hline S & I \end{array} \right) \right]. \quad (4.19)$$

Using the rules for obtaining the determinant of partitioned matrices [89], Equation (4.19) becomes

$$|D_N| = |Q||I - S Q^{-1} O| = |Q|. \quad (4.20)$$

Hence the localized edge and impurities dispersion relations for the semi-infinite zigzag ribbon are obtained by taking the limit of Equation (4.20) as  $N \rightarrow \infty$

$$\lim_{N \rightarrow \infty} |D_N| = \lim_{N \rightarrow \infty} |Q| = |Q|. \quad (4.21)$$

In the special case of taking only the edge localized states, and no impurities lines present inside the sheet, Equation (4.21) becomes

$$\det(Q) = \begin{vmatrix} A_{11}^{-1} \Delta_e + A_{12}^{-1} \Delta_s + 1 & A_{11}^{-1} \Delta_s \\ A_{21}^{-1} \Delta_e + A_{22}^{-1} \Delta_s & A_{21}^{-1} \Delta_s + 1 \end{vmatrix} = 0, \quad (4.22)$$

which gives

$$\Delta_s^2 x^5 - 2\Delta_s x^4 - (2\Delta_s^2 + \Delta_e) x^3 - (1 - 2\Delta_s) x^2 + (\Delta_s^2 + \Delta_e) x - 1 = 0. \quad (4.23)$$

In another special case where the interaction of the edge with the interior sites is not affected

by the edge sites properties, i.e., when  $\Delta_s = 0$ , Equation (4.21) becomes

$$\det(A) = \begin{vmatrix} A_{11}^{-1}\Delta_e + 1 & 0 \\ A_{21}^{-1}\Delta_e & 1 \end{vmatrix} = A_{11}^{-1}\Delta_e + 1 = 0 \quad (4.24)$$

which is formally similar to expressions obtained for Heisenberg antiferromagnetic structures [126].

Equations (4.22) - (4.24) are important new results for localized states (at edges and/or impurities) in graphene, and we next utilize them in numerical calculations

### 4.3 Numerical results

Figures 4.2 and 4.3 show dispersion relations for the edge localized states of semi-infinite zigzag graphene sheets for different edge hopping to area hopping ratios. They are calculated first with  $\Delta_s = 0$  using Equation 4.24 for Figure 4.2 and then with a nonzero value of  $\Delta_s = -2.61$  for  $t_s = 1.19$  and  $t = 1.0$  using Equation 4.22 for Figure 4.3. Both figures show that the dispersion of the edge localized states depends on both the edge sites hopping properties and their effect on the interaction with the interior sites in the zigzag sheet. The results begin with the edge hopping equal to zero, which could be realized by saturating the carbons atoms on the edge. With this hopping value both calculations (those with and without  $\Delta_s$ ) result in an extended flat localized edge state through the whole Brillouin zone at the Fermi level  $\omega_F/t = 0$ . This is due to the localized edge wave functions, e.g., as in the case of density-functional theory (DFT) calculations for finite ribbon [128].

As the edge hopping increases from zero, the dispersion of the edge localized state begins to have a part that corresponds to the Fermi level  $\omega_F = 0$ , and the remaining part behaves as a

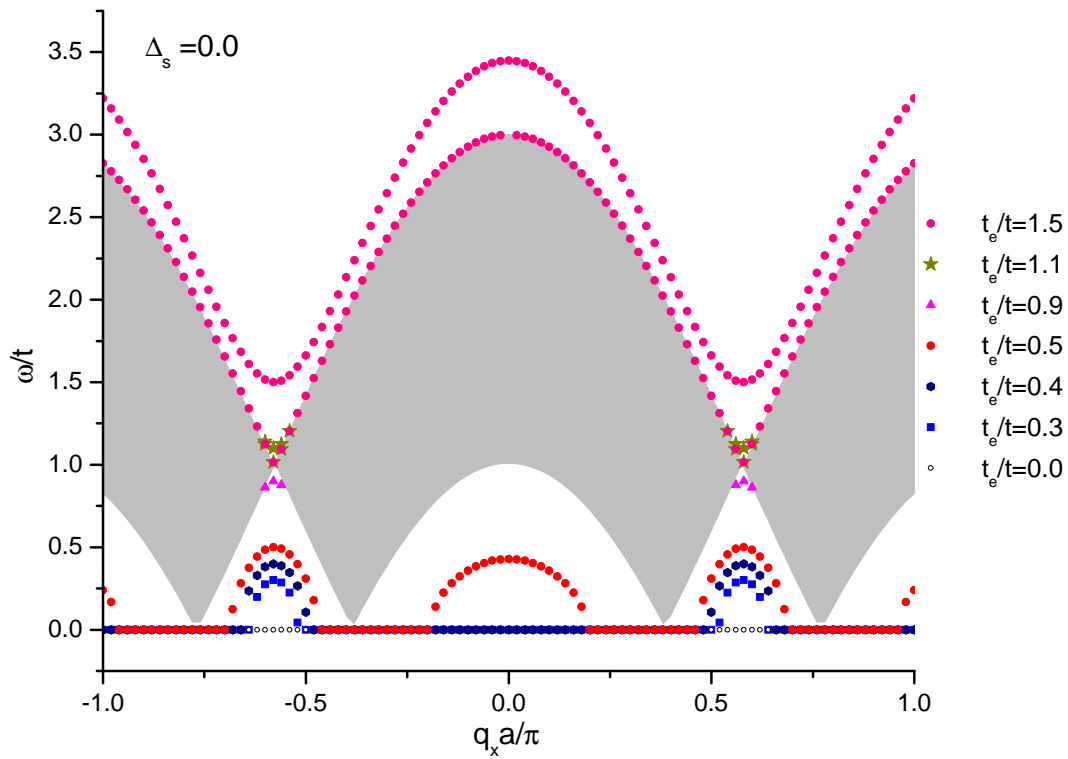


Figure 4.2: Edge localized states for different edge hopping calculated with  $\Delta_s = 0$ , where the shaded band represent the area modes continuum.

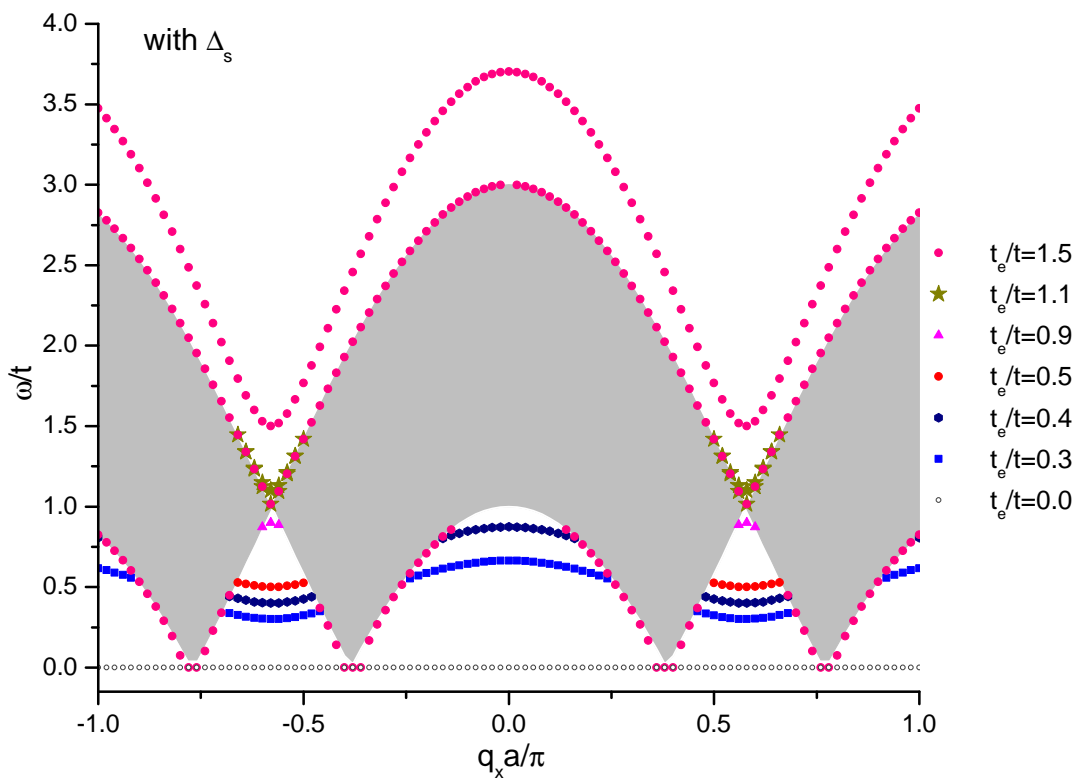


Figure 4.3: Edge localized states for different edge hopping calculated with a nonzero value of  $\Delta_s = -2.61$ , where the shaded band represent the area modes continuum.

liftoff from the Fermi level. The percentage of the edge dispersion that lies at the Fermi level is important for the electronic properties of the zigzag edged graphene nanoribbons.

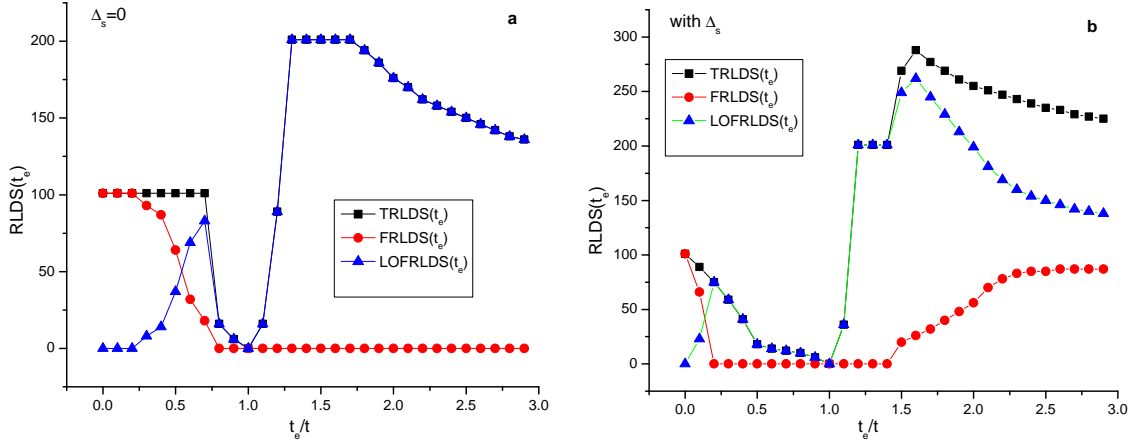


Figure 4.4: The variation of TRLDOS, FRLDOS, and LOFRLDOS as a function of edge hopping ratio from 0 to 2.9. (a) for  $\Delta_s = 0$  and (b) for  $\Delta_s = -2.61$ .

To study the variation of the edge dispersions percentage lying at the Fermi level with changes in the edge hopping and also to help with interpreting the data displayed in Figures 4.2 and 4.3, we define the following three density of states parameters which can be calculated for any given edge hopping value. The first one is the Relative Localized Density of States near Fermi level (FRLDOS), which is calculated computationally by counting the total number of points in the localized edge dispersion with  $\omega/t < 0.2$ . The second parameter is the Total Relative Localized Density of States (TRLDOS), which is calculated computationally by counting the total number of points in the localized edge dispersion, which is a relative measure of its total density of states. The third parameter is just the difference between FRLDOS and TRLDOS which is related to the liftoff percentage of the edge localized state dispersion from the Fermi level (LOFRLDOS).

Figure 4.4 shows the variation of TRLDOS, FRLDOS, and LOFRLDOS for the edge localized states as a function of edge to area hopping ratio ranging from 0 to 2.9 in increments of

0.1. Here panel (a) represents the calculation with  $\Delta_s = 0$ , while panel (b) represents the calculation with a nonzero value of  $\Delta_s = -2.61$ . By comparing Figure 4.4(a) with Figure 4.2 and similarly Figure 4.4(b) with Figure 4.3, the variations of the edge localized states dispersion with different edge hopping values can be interpreted as follows.

First, for the dispersion of the localized edge state calculated when  $\Delta_s = 0$  and starting with the edge hopping equal to zero, Figure 4.4(a) shows that FRLDOS is equal to TRLDOS which means that the edge localized state lies completely in the Fermi level while LOFRLDOS is zero. In Figure 4.2 it is shown as a flat localized edge state at the Fermi level  $\omega_F/t = 0$  extending through the whole Brillouin zone as mentioned above. For small increases in the edge hopping there is no change in the value of FRLDOS and it is still equal to TRLDOS with LOFRLDOS equal to zero. Beginning from the edge hopping equal to 0.3 the FRLDOS begins to decrease and the LOFRLDOS begins to increase while the TRLDOS remains roughly constant which means that some of dispersion has a lift off from the Fermi level as shown in Figure 4.2 near  $q_x a/\pi = \pm 0.5$ . There is a further evolution of this behavior, as seen from Figure 4.4(a), as the edge hopping is progressively increased. Eventually, when the edge hopping is equal to the interior hopping, the edge localized states completely disappear. Figure 4.4(a) shows that FRLDOS is essentially zero in the edge hopping range 0.9–2.9. As the edge hopping increases from around 1 up to 2.9, LOFRLDOS is equal to TRLDOS. The LOFRLDOS increases very quickly to large value with increase of the edge hopping from 1 to 1.3, and then it remains roughly constant in the edge hopping range 1.3 – 1.7, after which the LOFRLDOS decreases slowly. This behavior shows up in Figure 4.2 as an increase in the edge localized states above the band of area states.

The second case is for the dispersion of the localized edge state calculated when  $\Delta_s \neq 0$ .



Starting with edge hopping equal to zero Figure 4.4(b) shows that FRLDOS is equal to TRLDOS while LOFRLDOS is zero, which is similar to the first case just described. At the edge hopping equal to 0.1 the values of FRLDOS and TRLDOS begin to decrease and LOFRLDOS begins to increase which is qualitatively the same as before. In the edge hopping range from 0.2 to 1.4, the FRLDOS become zero and TRLDOS become equal to LOFRLDOS. In the edge hopping range 0.2 to 1, the LOFRLDOS decreases to a zero value, which is shown in Figure 4.3 as a decrease in the edge localized states dispersion, and at the same time the edge localized state shifts up in the energy. It is important to note that at the edge hopping 0.5, the edge localized states dispersion becomes very similar to the well-known characteristic edge localized state for graphene zigzag nanoribbons [42, 41, 40, 33] but here it is shifted from the Fermi level due to the edge hopping properties. When the edge hopping is equal to the interior hopping, the edge localized states completely disappear. The LOFRLDOS increases very quickly to a large value with further increase of edge hopping from 1 to 1.2, and then it remains constant in the edge hopping range 1.2 – 1.4. Above that range, the LOFRLDOS increases to a peak value at the edge hopping 1.6 and then slowly decrease until the edge hopping 2.9. Starting from the edge hopping 1.4, the LOFRLDOS begins to slowly increase until the edge hopping reaches 2.3, above which the LOFRLDOS converges to a nearly constant value. The TRLDOS increases to a peak at edge hopping 1.6 and it then begins to slowly decrease on further increasing the edge hopping. The behavior of the three parameters is reflected in Figure 4.2 as a change in the localized edge states around the band of area states.

The effects of both the impurities hopping and the impurities line position on the impurities localized states have been calculated using Equation 4.21 and the results are summarized in Figures 4.5 for four different geometries. This calculation was done considering the edge

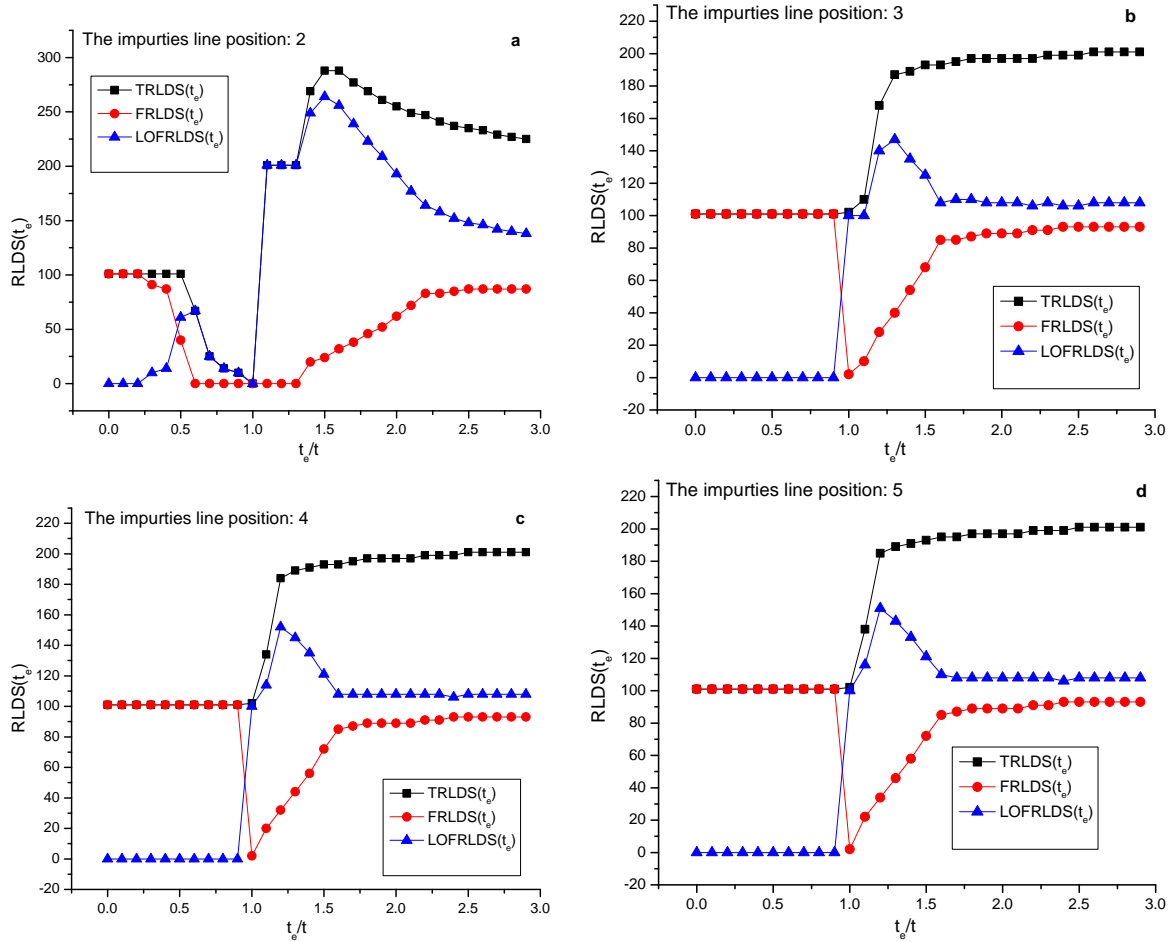


Figure 4.5: The variation of TRLDOS, FRLDOS, and LOFRLDOS as functions of the impurities hopping from 0 to 2.9 for the impurities line in sublattice  $A$  at positions (a) 2, (b) 3, (c) 4, and (d) 5.

hopping to be equal to 1 in our dimensionless units. The variation of TRLDOS, FRLDOS, and LOFRLDOS as a function of the impurities hopping from 0 to 2.9 are shown for the impurities line in sublattice  $A$  positioned at row numbers of (a) 2, (b) 3, (c) 4, and (d) 5. It is clear that the dispersion of the impurities localized states when the impurities line is located at the second row of the sublattice  $A$  is very similar to the dispersion of the edge localized states described above, as might be expected. However, beginning from position three in the sublattice  $A$ , the dispersion of the impurities localized states becomes quite different and remains approximately independent of the impurities line position in the sublattice  $A$ . Apart from this, the general

features of the different curves in Figure 4.5 (a)-(d) can be interpreted in a similar fashion to the preceding cases.

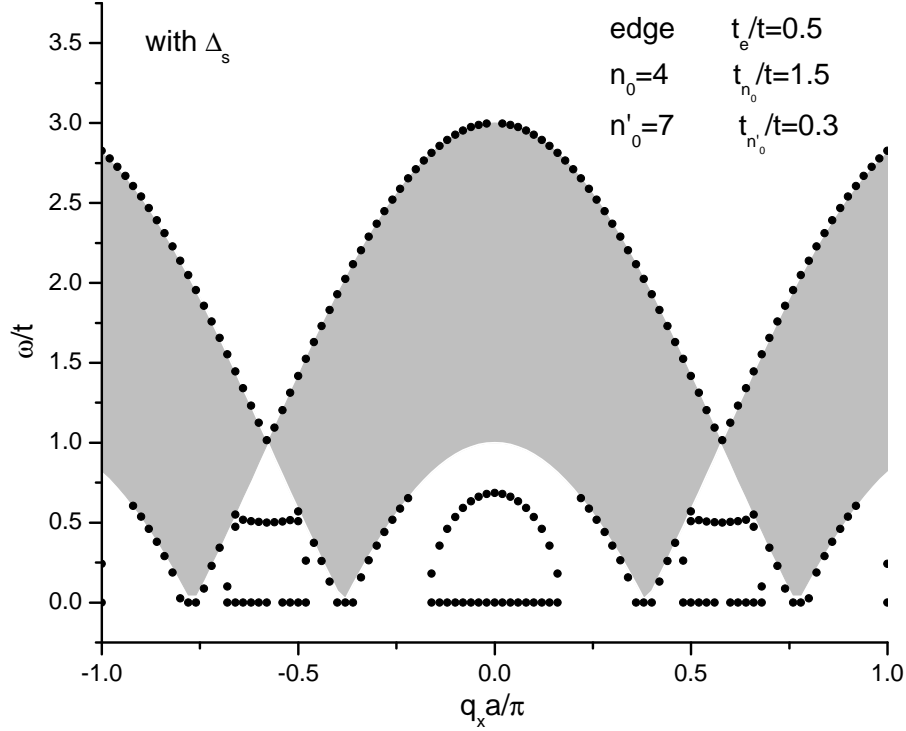


Figure 4.6: The localized edge and impurities states (indicated by black dots) plotted versus wavevector to illustrate the effects of an edge and two lines of impurities at sublattice A. The shaded band represents the area modes continuum. The edge hopping is  $t_e/t = 0.5$ , the first impurities line position is  $n_0 = 4$  with the impurities hopping  $t_{n_0}/t = 1.5$ , and the second impurities line position is  $n'_0 = 7$  with the impurities hopping  $t_{n'_0}/t = 0.3$ .

## 4.4 Discussion and Conclusions

In this chapter the tridiagonal matrix method was used to study the effect of edge and impurities sites on their localized states in semi-infinite zigzag edged 2D honeycomb graphene sheets. It was found that the tridiagonal method provides us with two somewhat different situations in studying the effect of the edge sites properties on their localized states. In the first one, the interaction of the edge with the interior sites is not directly affected by the edge site properties,

i.e., because parameter  $\Delta_s = 0$ , and in the second one the interaction of the edge with the interior sites is affected significantly by the edge sites properties, i.e., parameter  $\Delta_s \neq 0$ .

The results of the case  $\Delta_s = 0$  show that localized edge states dispersion has a  $q_x$  dependence characteristic of the hopping in a 1D chain (see Figure 1.11) at low edge hopping values, which reflects the effective isolation of edge hopping from the interior processes. This behavior with the strong edge effects indicates a departure from the usual 2D behavior found in the tight binding model for a graphene sheet. The results of the case when  $\Delta_s \neq 0$  show that the localized edge states dispersion has a  $q_x$  dependence characteristic of the hopping in a 2D honeycomb lattice but it is shifted in the energy due to the edge hopping properties. In particular, at the edge hopping 0.5, the localized edge states dispersion becomes very similar to that in previous work on the edge localized state for a graphene zigzag nanoribbon [42, 41, 40, 33] but here it is shifted in value. In this case the behavior is in closer correspondence with the usual behavior found in the tight binding model.

In situations where it is necessary to consider the combined effects of both the impurities hopping and the impurities line position on the impurities localized states, our results show that impurities in the second row of the sublattice  $A$  give rise to similar effects as found for the edge localized states dispersion. For impurities in higher row numbers the impurities localized states are significantly modified and becomes nearly independent of the impurities line position in sublattice  $A$ .

The general model and formal results obtained in this chapter can also be used to study the effects of the hopping properties in a semi-infinite graphene nanoribbon with an edge and two separated lines of impurities at sublattice  $A$ . Dispersion relations can be deduced for the coupled localized states (edge and impurities), and an example of this is shown in Figure 4.6.

Finally, we comment that the results of considering the interaction of the edge with the interior sites, as represented by taking  $\Delta_s \neq 0$ , show a realistic behavior for the dependence of the edge localized states of zigzag graphene on the edge sites properties, which may help to explain the experimental results of measured local density of states at the edge of graphene [129]. At the same time it may help to resolve inconsistencies between the semiconductor behavior found in the experimental data for fabricated GNRs [125, 5] and the expected theoretical semi-metallic behavior calculated without considering the edge localized states [42, 41, 40, 33].

# Chapter 5

## The Effect of Next Nearest Neighbors on the Properties of Graphene Nanoribbons

### 5.1 Introduction

We saw in the previous chapters that the physical properties of 2D materials like graphene nanoribbons and magnetic stripes can, to a large extent, be attributed to both their lattice structure and the range of interactions between the sites. By fixing the range of interactions to include only the NN hopping, the comparisons made between the results obtained for the 2D magnetic square lattice (in Chapter 2), zigzag edged and armchair edged 2D magnetic honeycomb lattices (in Chapter 3) and graphene structures (in Chapter 4) show that the 2D lattice structure and its edge configuration play very important roles in the dispersion relations and consequently for the possible applications.

However, experiments and theories [130, 33, 49, 47] also suggest that increasing the range of the interaction to include the next nearest neighbor (NNN) in the graphene 2D honeycomb lattice also changes its dispersion relations by removing dispersion symmetry around the Fermi level and it changes the behavior around the impurities in the lattice [131]. Further, we note that including the NNN hopping in a 2D square lattice is known to change the dispersion relations

(see [132] and Chapter 2), so it is to be expected that this might be so in the graphene structure.

In this chapter, the graphene Hamiltonian (1.31) with inclusion of the NNN interaction term will be used to study the new effects on the dispersion relations, edge states, and impurities states in the graphene nanoribbons with zigzag and armchair edges. The obtained results should also be readily modifiable to apply to the magnetic case treated in Chapter 3, since the NNN interaction term can similarly be added to Heisenberg Hamiltonian [133, 134].

## 5.2 Theoretical model

The system initially under study is a 2D graphene nanoribbon in the  $xy$ -plane. The crystallographic description of the graphene honeycomb lattice has already been given in Section 1.1, and shown in Figure 1.5. As before, the nanoribbon is of finite width in the  $y$  direction with  $N$  atomic rows (labeled as  $n = 1, \dots, N$ ) and it is infinite in the  $x$  direction ( $-\infty \Leftrightarrow \infty$ ) (see Figure 5.1). The total Hamiltonian of the system is given by Equation (1.31) as follows:

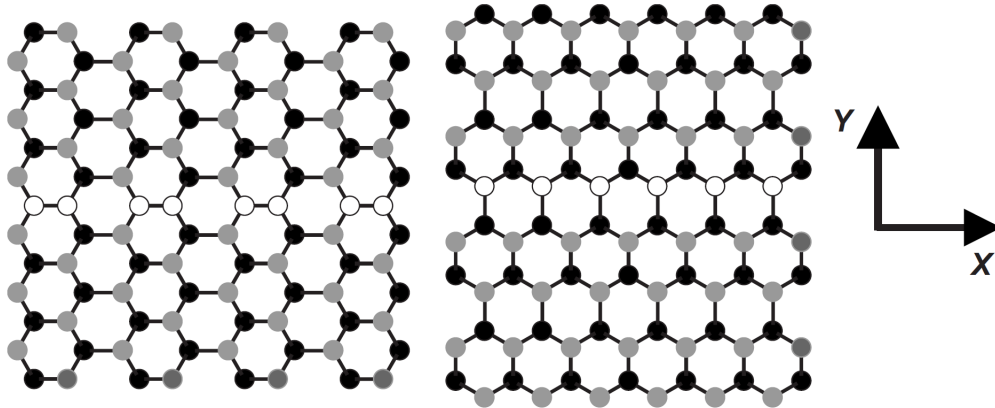


Figure 5.1: Armchair (left) and zigzag (right) graphene 2D honeycomb nanoribbons in the  $xy$ -plane, where the black (gray) dots are the sublattice sites A(B) with a line of impurities (white dots) in the middle of the sheet. The stripes are finite in the  $y$  direction with  $N$  rows ( $n = 1, \dots, N$ ) and they are infinite in the  $x$  direction. Figure taken from [39].

$$\hat{H} = - \sum_{\langle ij \rangle} t_{0ij} (\mathbf{a}_i^\dagger \mathbf{b}_j + \mathbf{h.c.}) + t_{1ij} (\mathbf{a}_i^\dagger \mathbf{a}_j + \mathbf{b}_i^\dagger \mathbf{b}_j + \mathbf{h.c.}). \quad (5.1)$$

The notation is defined in Chapter 1, where the first term  $t_{0ij}$  ( $\approx 2.8\text{eV}$ ) is the NN hopping energy given in Equation (1.21), and in graphene it is the hopping between different sublattices  $A$  and  $B$ . Also  $t_{1ij}$  ( $\approx 0.1\text{eV}$ ) is the NNN hopping energy which in graphene is hopping in the same sublattice [33, 49, 47]. The summations over  $i$  and  $j$  run over all the sites but they belong to different sublattices for the NN hopping term, and they belong to the same sublattice for the NNN hopping (see Section 1.1). The NN hopping  $t_{0ij}$  has a constant “bulk” value  $t$  when either  $i$  and  $j$  are in the interior of the nanoribbon, and another constant value  $t_e$  when  $i$  and  $j$  are both at the edge of the nanoribbon (i.e., in row  $n = 1$  or  $n = N$ ). Similarly, for the NNN hopping energy  $t_{1ij}$ , we assume that it has a constant value  $t'$  when the site  $i$  is inside the nanoribbon, and it is equal to  $t'_e$  for sites at the edge of the nanoribbon.

Since the nanoribbon extends to  $\pm\infty$  in the  $x$  direction, we may introduce a 1D Fourier transform to wavevector  $q_x$  along the  $x$  direction for the fermion operators  $a_i^\dagger$  ( $a_i$ ) and  $b_j^\dagger$  ( $b_j$ ) as follows:

$$\begin{aligned} b_j(x) &= \frac{1}{\sqrt{N_0}} \sum_n b_n(q_x) e^{-i\mathbf{q}_x \cdot \mathbf{r}_j} & b_j^\dagger(x) &= \frac{1}{\sqrt{N_0}} \sum_n b_n^\dagger(q_x) e^{i\mathbf{q}_x \cdot \mathbf{r}_j} \\ a_i(x) &= \frac{1}{\sqrt{N_0}} \sum_n a_n(q_x) e^{-i\mathbf{q}_x \cdot \mathbf{r}_i} & a_i^\dagger(x) &= \frac{1}{\sqrt{N_0}} \sum_n a_n^\dagger(q_x) e^{i\mathbf{q}_x \cdot \mathbf{r}_i}. \end{aligned} \quad (5.2)$$

Here  $N_0$  is the (macroscopically large) number of sites in any row,  $\mathbf{q}_x$  is a wavevector in the first Brillouin zone of the reciprocal lattice and both  $\mathbf{r}_i$  and  $\mathbf{r}_j$  are the position vectors of any carbon sites  $i$  and  $j$ . The new operators obey the following anticommutation relations:

$$\left[ a_n(q_x), a_n^\dagger(q'_x) \right] = \delta_{q_x q'_x}, \quad \left[ b_n(q_x), b_n^\dagger(q'_x) \right] = \delta_{q_x q'_x}. \quad (5.3)$$



Also, we define the two types of hopping sums

$$\begin{aligned}\tau(q_x) &= \sum_{\nu} t_{0ij} e^{-i\mathbf{q}_x \cdot (\mathbf{r}_i - \mathbf{r}_j)} \\ \tau'(q_x) &= \sum_{\nu'} t_{1ij} e^{-i\mathbf{q}_x \cdot (\mathbf{r}_i - \mathbf{r}_j)}.\end{aligned}\quad (5.4)$$

The sum for the hopping terms  $t_{0/1ij}$  is taken to be over all  $\nu$  NN and over all  $\nu'$  NNNs in the lattice. They depend on the edge configuration as zigzag or armchair for the stripe (see Section 1.1 and Figure 1.6). For the armchair configuration, the hopping sum for NN gives the following factors  $\tau_{nn'}(q_x)$

$$\tau_{nn'}(q_x) = t \left[ \exp(iq_x a) \delta_{n',n} + \exp\left(i\frac{1}{2}q_x a\right) \delta_{n',n\pm 1} \right] \quad (5.5)$$

and for the zigzag configuration it gives

$$\tau_{nn'}(q_x) = t \left[ 2 \cos\left(\frac{\sqrt{3}}{2}q_x a\right) \delta_{n',n\pm 1} + \delta_{n',n\mp 1} \right]. \quad (5.6)$$

The hopping sum for NNNs gives the following factors  $\tau'_{nn'}(q_x)$

$$\tau'_{nn'}(q_x) = t' [\delta_{n',n\pm 2} + 2 \cos(q_x a 3/2) \delta_{n',n\pm 1}] \quad (5.7)$$

for the armchair configuration, and

$$\tau_{nn'}(q_x) = 2t' \left[ \cos(\sqrt{3}q_x a) \delta_{n',n} + \cos(\sqrt{3}q_x a/2) \delta_{n',n\pm 2} \right] \quad (5.8)$$

for the zigzag configuration case, where the  $\pm$  sign, in all the above factors, depends on the sublattice since the atom lines alternate from A and B.

Substituting Equations (5.2) and (5.4) into Equation (5.1), and rewriting the summation

over NN and NNN sites, we get the following form of the operator term  $\hat{H}$ :

$$\hat{H} = - \sum_{nn'} \tau'_{nn'}(q_x) (a_n^\dagger a_{n'} + b_n^\dagger b_{n'}) + \tau_{nn'}(q_x) a_n b_{n'}^\dagger + \tau_{nn'}(-q_x) a_n^\dagger b_{n'}. \quad (5.9)$$

This expression contains both the intrasublattice and intersublattice coupling terms. In order to diagonalize  $\hat{H}$  and obtain the dispersion relations for graphene nanoribbons, we may again consider the time evolution of the creation and the annihilation operators  $a_i^\dagger$  ( $a_i$ ) and  $b_j^\dagger$  ( $b_j$ ), as calculated in the Heisenberg picture in quantum mechanics. In this case, the equations of motion (using the units with  $\hbar = 1$ ) for the annihilation operators  $a_i$  ( $b_j$ ) are as follows [44, 60, 37, 43, 48]:

$$\begin{aligned} \frac{da_n}{dt} &= i[H, a_n] \\ &= i \sum_{nn'} -\tau'_{nn'}(q_x) a_{n'} - \tau_{nn'}(-q_x) b_{n'} \end{aligned} \quad (5.10)$$

and

$$\begin{aligned} \frac{db_n}{dt} &= i[H, b_n] \\ &= i \sum_{nn'} -\tau'_{nn'}(q_x) b_{n'} - \tau_{nn'}(q_x) a_{n'} \end{aligned} \quad (5.11)$$

where the fermion relations in Equation (5.3) were used.

The electronic dispersion relations of the graphene nanoribbon (i.e., energy or frequency versus wavevector) can now be obtained by solving the above operator equations of motion. As before, the electronic energy can be expressed in terms of the frequency using the relation  $E = \hbar\omega$ , and assuming that electronic energy modes behave like  $\exp[-i\omega(q_x)t]$ . Eventually, on substituting this time dependence into the above equations, we get the following sets of

coupled equations:

$$\omega(q_x)a_n = \sum_{nn'} \tau'_{nn'}(q_x)a_{n'} + \tau_{nn'}(-q_x)b_{n'} \quad (5.12)$$

$$\omega(q_x)b_n = \sum_{nn'} \tau_{nn'}(q_x)a_{n'} + \tau'_{nn'}(q_x)b_{n'} \quad (5.13)$$

The above equations can next be written in matrix form as follows:

$$\omega(q_x) \begin{bmatrix} a_n \\ b_n \end{bmatrix} = \begin{bmatrix} T'(q_x) & T(q_x) \\ T^*(q_x) & T'(q_x) \end{bmatrix} \begin{bmatrix} a_n \\ b_n \end{bmatrix} \quad (5.14)$$

where the solution of this matrix equation is given by the condition

$$\det \begin{bmatrix} -(\omega(q_x)I_N - T'(q_x)) & T(q_x) \\ T^*(q_x) & -(\omega(q_x)I_N - T'(q_x)) \end{bmatrix} = 0 \quad (5.15)$$

while  $T(q_x)$  and  $T'(q_x)$  are the NN and NNN interaction matrices respectively, which depend

Table 5.1: NN hopping matrix elements for the graphene honeycomb lattice

Parameter	Zigzag	Armchair
$\alpha$	0	$te^{-iq_x a}$
$\beta$	$2t \cos(\sqrt{3}q_x a/2)$	$te^{iq_x a/2}$
$\gamma$	$t$	$te^{iq_x a/2}$

Table 5.2: NNN hopping matrix elements for the graphene honeycomb lattice

Parameter	Zigzag	Parameter	Armchair
$\epsilon$	$2t' \cos(\sqrt{3}q_x a)$	$\theta$	$t'$
$\zeta$	$2t' \cos(\sqrt{3}q_x a/2)$	$\eta$	$2t' \cos(q_x a/2)$

on the orientation of the ribbon, and  $\omega(q_x)$  are the energies of the modes. Explicitly the matrix

$T(q_x)$  is given by

$$\begin{pmatrix} \alpha & \beta & 0 & 0 & \cdots \\ \beta & \alpha & \gamma & 0 & \cdots \\ 0 & \gamma & \alpha & \beta & \cdots \\ 0 & 0 & \beta & \alpha & \cdots \\ \vdots & \vdots & \vdots & \vdots & \ddots \end{pmatrix}. \quad (5.16)$$

Similarly the matrix  $T'(q_x)$  for a zigzag ribbon is given by

$$\begin{pmatrix} \epsilon & 0 & \zeta & 0 & 0 & \cdots \\ 0 & \epsilon & 0 & \zeta & 0 & \cdots \\ \zeta & 0 & \epsilon & 0 & \zeta & \cdots \\ 0 & \zeta & 0 & \epsilon & 0 & \cdots \\ 0 & 0 & \zeta & 0 & \epsilon & \cdots \\ \vdots & \vdots & \vdots & \vdots & \vdots & \ddots \end{pmatrix} \quad (5.17)$$

and the matrix  $T'(q_x)$  for an armchair ribbon is given by

$$\begin{pmatrix} 0 & \eta & \theta & 0 & 0 & \cdots \\ \eta & 0 & \eta & \theta & 0 & \cdots \\ \theta & \eta & 0 & \eta & \theta & \cdots \\ 0 & \theta & \eta & 0 & \eta & \cdots \\ 0 & 0 & \theta & \eta & 0 & \cdots \\ \vdots & \vdots & \vdots & \vdots & \vdots & \ddots \end{pmatrix} \quad (5.18)$$

The parameters  $\alpha, \beta, \gamma, \epsilon, \zeta, \theta$  and  $\eta$  depend on the stripe edge geometry and are given in Tables 5.1 and 5.2.

We remark that in the limiting case when the NNN hopping  $t'$  can be neglected compared to NN hopping  $t$ , we may put  $T'(q_x)$  equal to the zero matrix  $\mathbf{0}$  and Equation (5.15) reduces to

$$\det \begin{bmatrix} -(\omega(q_x)I_N) & T(q_x) \\ T^*(q_x) & -(\omega(q_x)I_N) \end{bmatrix} = 0 \quad (5.19)$$

which is just the result obtained previously for graphene ribbons using the tight binding model with only the NN hopping [39]. This is as expected.

In this chapter we are more concerned with the specific effects of NNN hopping on the graphene properties, which are expected to be significant for the dispersion curves at certain wavevectors.

### 5.3 Numerical results

The dispersion relations for the above types of graphene nanoribbons are next obtained numerically as the eigenvalues [89, 90] at any chosen wave vector corresponding to the matrix Equation (5.14). From the numerical point of view, this is very similar to the form of Equation (3.13) for magnetic structures, and therefore the analogous numerical calculations as used in Section 3.3 can again be used here to get the required solutions.

To compare our results obtained for the case where there are both NN and NNN interactions in the system with the case of only NN interactions, we choose our stripe sizes and physical parameters similar to those used in Chapter 3 for the magnetic stripes and in reference [39] for graphene.

Figures 5.2 shows the effect of the NNN interaction in the dispersion relations, with edge states and impurities states included, for graphene zigzag nanoribbons. The panels on the left

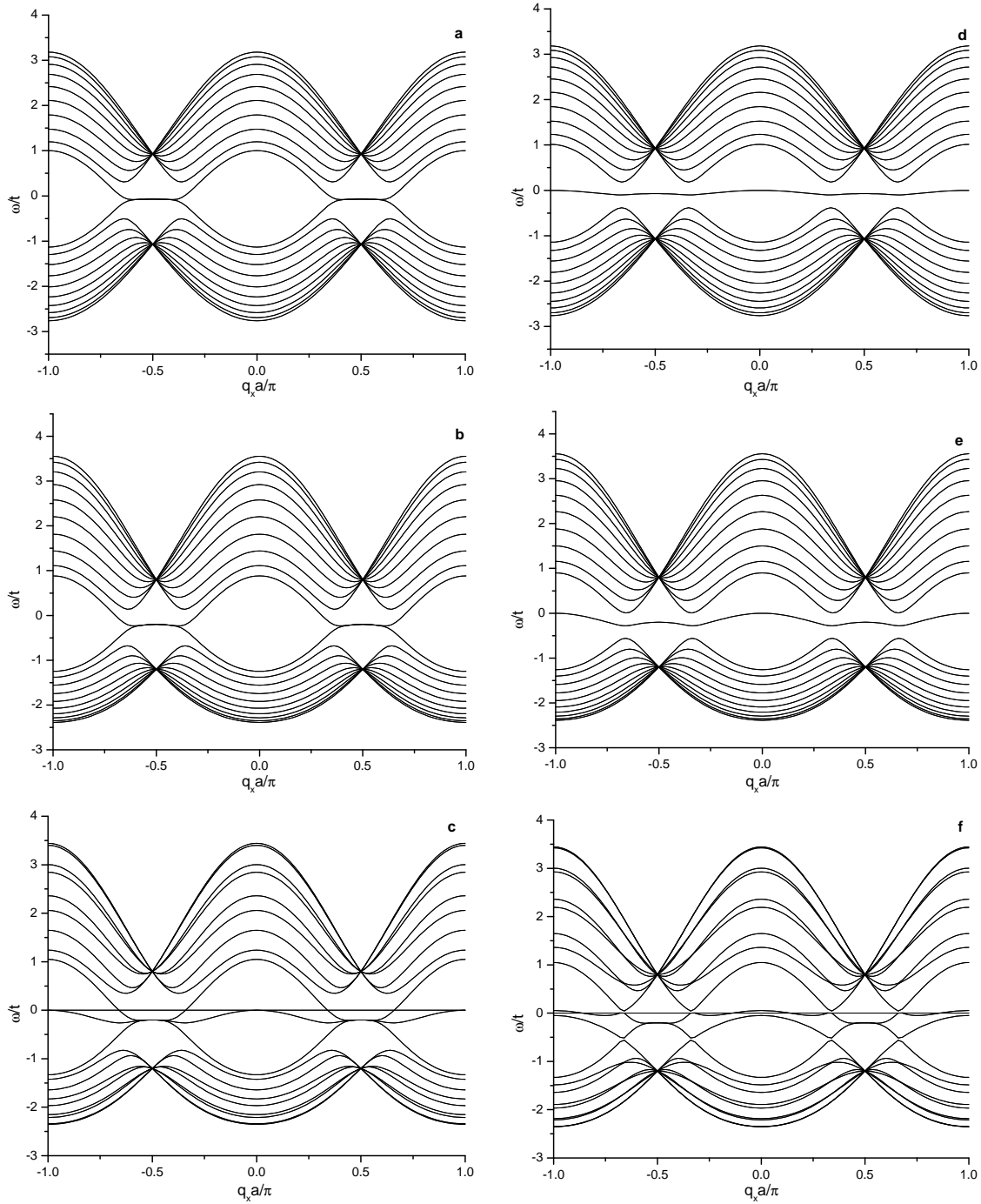


Figure 5.2: The effect of NNN interaction on the dispersion relations, edge states, and impurities states in the graphene zigzag nanoribbons. Left side: stripe width  $N = 20$  with (a)  $t' = 0.036t$  (b)  $t' = 0.1t$  (c)  $t' = 0.1t$  and with the impurities line at row number 11 with  $J_I = 0$ . Right side: stripe width  $N = 21$  with (d)  $t' = 0.036t$  (e)  $t' = 0.1t$  (f)  $t' = 0.1t$  and with the impurities line at row number 11 with  $J_I = 0$ .

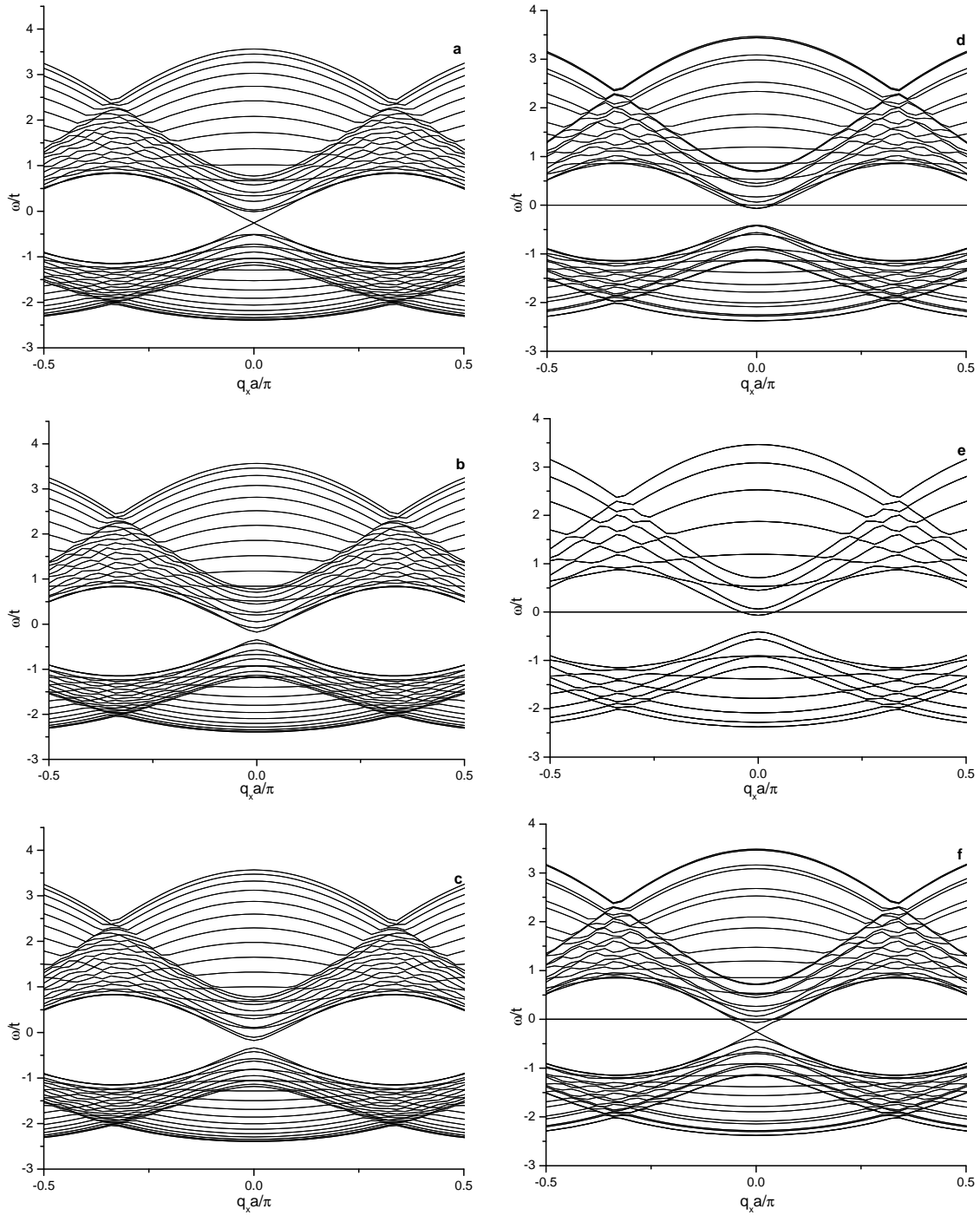


Figure 5.3: The effect of NNN interaction on the dispersion relations, band gap, and impurities states in the graphene armchair nanoribbons. Left side:  $t' = 0.1t$  for stripe width (a)  $N = 20$  (b)  $N = 21$  (c)  $N = 22$ . Right side:  $t' = 0.1t$  and with the impurities line at row number 11 with  $J_I = 0$  for stripe width (d)  $N = 20$  (e)  $N = 21$  (f)  $N = 22$ .

and right are for even ( $N = 20$ ) and odd ( $N = 21$ ) numbers of rows, respectively. In each case different ratios of  $t'/t$  are shown, either with or without a line of impurities. As expected, all figures show the absence of dispersion symmetry around the Fermi level with a shift of the Fermi level value towards the valence band. Figure 5.2 (a) and (d) show the effect for the NNN value of  $t' = 0.036t$ , which correspond to  $t' \approx 0.1$  eV and  $t \approx 2.8$  eV given in references [33, 49]. The change in the dispersion symmetry around the Fermi level with the shift of the Fermi level value is small compared to the analogous magnetic results in Chapter 3 for similar zigzag nanoribbons without the NNN interaction. When the NNN interaction increases to  $t' = 0.1t$  as shown in Figure 5.2 (b) and (e) the density of states increases in the conduction band and decreases in the valence band removing the symmetry around the Fermi level and shifting it.

Figures 5.2 (c) and (f) are included to show the effect of NNN interactions on the impurities states in the zigzag nanoribbons. Introducing the NNN hopping in the lattice shifts the Fermi level and changes the density of the states around the impurities level.

Figures 5.3 show the effect of the NNN interaction on the dispersion relations and impurities states in the case of the graphene armchair nanoribbons. For a full description we need to consider three consecutive values (taken here as 20, 21, and 22) of the integer  $N$  as explained earlier. The behavior in the armchair case when the NNN interactions are included is very similar to the zigzag case described above as regards removal of the symmetry around the Fermi level, its shift, and its effect on the impurities level. At zero wave vector it is found that there is no effect on the absence of edge states in armchair nanoribbons or on their band shape when NNN interactions are included in the model.



## 5.4 Discussion and Conclusions

In this chapter the effect of introducing NNN hopping was studied for the 2D honeycomb two-sublattice structure of graphene. Including the NNN interactions in the model resulted in the inclusion of an extra hopping matrix  $T'(q_x)$ , which depends on the wave vector  $q_x$  in the nanoribbons symmetry direction and provides intra-sublattice terms in the diagonalization matrix. This procedure was carried out for the NNN hopping in both zigzag and armchair stripes.

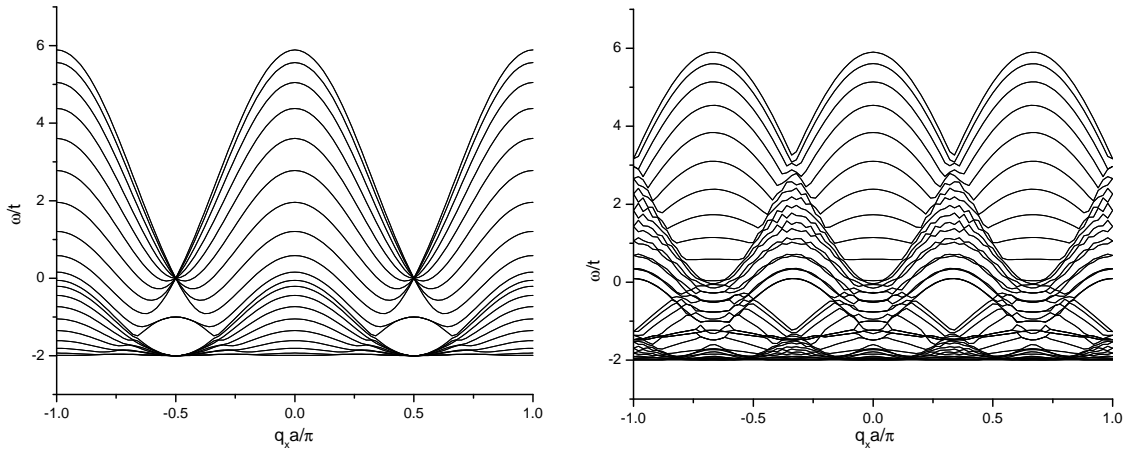


Figure 5.4: The effect of a higher NNN interaction corresponding to  $t' = 0.5t$  on the dispersion relations on the zigzag (left panel) and armchair (right panel) nanoribbons with width  $N = 20$ .

When  $t'$  is very small compared to  $t$ , we find that the extra contributions to the dispersion relations due to the intra-sublattice NNN hopping remain small for most wave vectors in the Brillouin zone, as anticipated. The main effect of NNN hopping, however, in the range of small  $t'/t$  is changing the density of states for the dispersion relations, which can be explained broadly as follows. The probability for the particles to hop within the same sublattice by NNN hopping increases with increasing energy and consequently the net number of particles from any given mode that are able to undergo NNN hopping is very roughly proportional to

the mode energy. The highest energy mode therefore has a higher number of particles that participate in NNN hopping, and this number decreases for lower mode energies. The overall effect is, after taking account of different phase-space factors at large and small wave vectors, that the density of states tends to be increased for the higher-energy modes, and vice-versa for the lower-energy modes. This contributes to the removal of the symmetry around the Fermi level and shifts it, and this effect increases with increasing NNN hopping. If the NNN hopping become comparable with the NN hopping the dispersion will become changed more drastically, and this is seen in Figure 5.4.

Finally, for comparison we made some calculations for the role of NNN interactions in analogous magnetic stripes with the 2D square lattice structure by contrasting it with the 2D honeycomb lattice (using methods in Chapters 2 and 3). We concluded that the NNN interactions (hopping terms) have a more significant influence on the dispersion relation in the honeycomb lattice case. This is, in part, due to the fact that the number and ratio of NNN sites to NN sites is different in the two structures.

# Chapter 6

## Some Properties of Bilayer Graphene Nanoribbons

### 6.1 Introduction

In the previous chapters, we have studied the effects of lattice structures (including both the honeycomb and square lattices), the interaction range (NN and NNN), and the presence of impurities on the dispersion relations of the 2D materials. This was carried out both for graphene nanoribbons and magnetic stripes in order to compare and contrast their behavior. The intrinsic physical properties of 2D materials may not, in general, be easily tunable and therefore they cannot necessarily meet many technological applications design requirements. However, it has been proposed in the literature that a system of two graphene layers stacked on top of each other might give rise to the possibility of controlling their physical properties by introducing asymmetry between the layers. This could be done in various ways like varying the external electric or magnetic field, rotation between the two layers, and introducing impurities in one layer [135, 136, 137, 138, 139]. This opens the possibility of technological applications using bilayer graphene [20].

In this chapter, we will extend our formalism for single-layer graphene as developed in

Chapters 4 and 5 to examine the effect of forming a system of two layers stacked on top of each other. We then derive the dispersion relations and study the localized edge modes. Specifically, the system that will be used for our study consists of two graphene layers stacked directly on top of each other to form what is called AA-stacking bilayer graphene (BLG) nanoribbons. This system is interesting both experimentally and theoretically [140, 141, 142, 143].

The tight binding Hamiltonian (1.31) will be used as before to describe the NN and NNN hopping in each graphene single layer (GSL), while additional tight binding terms are introduced to describe the direct hopping between the two layers [20, 33]. As well as the main applications to graphene bilayer nanoribbons, the results should also be capable of extension to similar magnetic stripes in bilayer configurations which could be fabricated as "nanodot" arrays [144, 145, 146, 147].

## 6.2 Theoretical model

The system initially under study consists of two graphene layers stacked directly on top of each other, i.e., AA-stacking bilayer graphene (BLG) nanoribbons in the  $xy$ -plane, where we use the indices "t" and "b" to label the top and bottom layer, respectively. The crystallographic description of each graphene layer with its honeycomb lattice is given in Section 1.1, and is shown in Figure 1.5. The bilayer nanoribbon is of finite width in the  $y$  direction with  $N$  atomic rows (labeled as  $n = 1, \dots, N$ ) and it is infinite in the  $x$  direction (see Figure 6.1).

The total Hamiltonian of the system is given as follows:

$$\hat{H} = \hat{H}_t + \hat{H}_b + \hat{H}_i, \quad (6.1)$$

where  $\hat{H}_t$  ( $\hat{H}_b$ ) is the Hamiltonian of the top (bottom) single layer of graphene (SLG) which

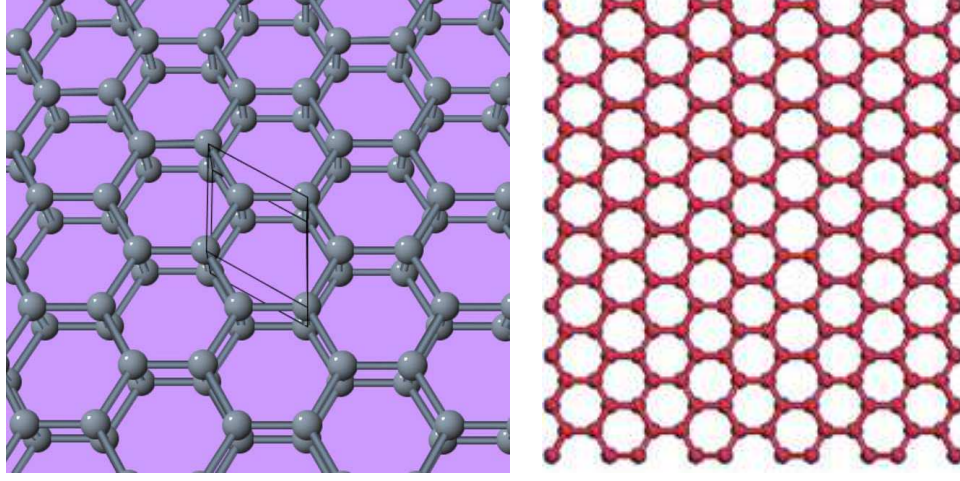


Figure 6.1: Direct on-top AA-stacking bilayer graphene (BLG). Left: the 2D unit cell is shown  $a = b = 0.267nm$ ,  $\gamma = 120^\circ$ . Right: AA-stacking BLG nanoribbons. Figures taken from [143, 142].

describes the in-plane hopping of non-interacting  $\pi$ -electrons on the top (bottom) layer and it is given by analogy with Equation (1.31) as

$$\begin{aligned}\hat{H}_t &= - \sum_{\langle ij,t \rangle} t_{0ij,t} (\mathbf{a}_{i,t}^\dagger \mathbf{b}_{j,t} + \mathbf{h.c}) + t_{1ij,t} (\mathbf{a}_{i,t}^\dagger \mathbf{a}_{j,t} + \mathbf{b}_{i,t}^\dagger \mathbf{b}_{j,t} + \mathbf{h.c}), \\ \hat{H}_b &= - \sum_{\langle ij,b \rangle} t_{0ij,b} (\mathbf{a}_{i,b}^\dagger \mathbf{b}_{j,b} + \mathbf{h.c}) + t_{1ij,b} (\mathbf{a}_{i,b}^\dagger \mathbf{a}_{j,b} + \mathbf{b}_{i,b}^\dagger \mathbf{b}_{j,b} + \mathbf{h.c}).\end{aligned}\quad (6.2)$$

The notation follows that defined in Chapter 1, where the first term in each layer  $t_{0ij}$  ( $\approx 2.8\text{eV}$ ) is the NN hopping energy given in Equation (1.21), and here in graphene it is the hopping between different sublattices  $A$  and  $B$ . Also  $t_{1ij}$  ( $\approx 0.1\text{eV}$ ) is the NNN hopping energy in each layer which here in graphene is the hopping in the same sublattice [33, 49, 47]. The summations in each layer over  $i$  and  $j$  run over all the sites where  $i$  and  $j$  belong to different sublattices for the NN hopping term, and they belong to the same sublattice for the NNN hopping energy (see Section 1.1). The labeling schemes for the various hopping terms (at an edge or in the interior) are the same as in the previous chapter for the single-layer case.

The third term in the total Hamiltonian  $\hat{H}_i$  represents the Hamiltonian of the direct inter-layer hopping between the top and the bottom single layers where the sublattice  $A_t$  ( $B_t$ ) of the top layer is directly above the sublattice  $A_t$  ( $B_t$ ) of the bottom layer. It is given by

$$\hat{H}_i = - \sum_{\langle i \rangle} \gamma_0 (\mathbf{a}_{i,b}^\dagger \mathbf{a}_{i,t} + \mathbf{b}_{j,b}^\dagger \mathbf{b}_{j,t} + \mathbf{h.c.}), \quad (6.3)$$

where  $\gamma_0$  the inter-layer NN coupling energy.

Since the nanoribbon extends to  $\pm\infty$  in the  $x$  direction, we may introduce a 1D Fourier transform to wavevector  $q_x$  along the  $x$  direction for the fermions operators  $a_i^\dagger$  ( $a_i$ ) and  $b_j^\dagger$  ( $b_j$ ) in each layer as follows:

$$\begin{aligned} b_j(x) &= \frac{1}{\sqrt{N_0}} \sum_n b_n(q_x) e^{-i\mathbf{q}_x \cdot \mathbf{r}_j}, & b_j^\dagger(x) &= \frac{1}{\sqrt{N_0}} \sum_n b_n^\dagger(q_x) e^{i\mathbf{q}_x \cdot \mathbf{r}_j}, \\ a_i(x) &= \frac{1}{\sqrt{N_0}} \sum_n a_n(q_x) e^{-i\mathbf{q}_x \cdot \mathbf{r}_i}, & a_i^\dagger(x) &= \frac{1}{\sqrt{N_0}} \sum_n a_n^\dagger(q_x) e^{i\mathbf{q}_x \cdot \mathbf{r}_i}. \end{aligned} \quad (6.4)$$

Here,  $N_0$  is the (macroscopically large) number of carbon sites in any row,  $\mathbf{q}_x$  is a wavevector in the first Brillouin zone of the reciprocal lattice and both  $\mathbf{r}_i$  and  $\mathbf{r}_j$  denote the position vectors of any carbon sites  $i$  and  $j$ . The new fermion operators obey the following anticommutation relations in each layer:

$$\left[ a_n(q_x), a_n^\dagger(q'_x) \right] = \delta_{q_x q'_x}, \quad \left[ b_n(q_x), b_n^\dagger(q'_x) \right] = \delta_{q_x q'_x}, \quad (6.5)$$

while the top layer operators anticommute with the bottom layer operators. Also, we define the hopping sums

$$\begin{aligned} \tau(q_x) &= \sum_v t_{0ij} e^{-i\mathbf{q}_x \cdot (\mathbf{r}_i - \mathbf{r}_j)}, \\ \tau'(q_x) &= \sum_{v'} t_{1ij} e^{-i\mathbf{q}_x \cdot (\mathbf{r}_i - \mathbf{r}_j)}. \end{aligned} \quad (6.6)$$

The sum for the hopping terms  $t_{0/1,ij}$  is taken to be over all  $\nu$  NNs and over all  $\nu'$  NNNs in the lattice and this depends on the edge configuration as zigzag or armchair for the stripe (see Section 1.1 and Figure 1.6). For the inter-layer coupling the in-plane wavevector  $\mathbf{q}_x$  is perpendicular to the inter-plane vector and so the hopping sum is only  $\gamma_0$  representing the corresponding NN coupling energy.

For the armchair configuration, the hopping sum for NNs gives the following factors  $\tau_{m'm'}(q_x)$  for each (top or bottom) layer:

$$\tau_{m'm'}(q_x) = t \left[ \exp(iq_x a) \delta_{n',n} + \exp\left(i\frac{1}{2}q_x a\right) \delta_{n',n\pm 1} \right] \quad (6.7)$$

and for the zigzag configuration, it gives:

$$\tau_{m'm'}(q_x) = t \left[ 2 \cos\left(\frac{\sqrt{3}}{2}q_x a\right) \delta_{n',n\pm 1} + \delta_{n',n\mp 1} \right]. \quad (6.8)$$

Explicitly the hopping sum for NNNs gives the following factors  $\tau'_{m'm'}(q_x)$  for each layer

$$\tau'_{m'm'}(q_x) = t' \left[ \delta_{n',n\pm 2} + 2 \cos(q_x a 3/2) \delta_{n',n\pm 1} \right] \quad (6.9)$$

for the armchair configuration, and

$$\tau_{m'm'}(q_x) = 2t' \left[ \cos(\sqrt{3}q_x a) \delta_{n',n} + \cos(\sqrt{3}q_x a/2) \delta_{n',n\pm 2} \right] \quad (6.10)$$

for the zigzag configuration case, where the  $\pm$  sign, in all the above factors, depends on the sublattice since the atom lines alternate between the A and B sublattices.

Substituting Equations (6.4) and (6.6) in Equation (6.1), and rewriting the summation over

NN and NNN sites, we get the following form of the total Hamiltonian operator  $\hat{H}$ :

$$\begin{aligned}
\hat{H} = & - \sum_{nn',t} \tau'(q_x)_t \left( a_{n,t}^\dagger a_{n',t} + b_{n,t}^\dagger b_{n',t} \right) + \tau(q_x)_t a_{n,t} b_{n',t}^\dagger + \tau(-q_x)_t a_{n,t}^\dagger b_{n',t} \\
& - \sum_{nn',b} \tau'(q_x)_b \left( a_{n,b}^\dagger a_{n',b} + b_{n,b}^\dagger b_{n',b} \right) + \tau(q_x)_b a_{n,b} b_{n',b}^\dagger + \tau(-q_x)_b a_{n,b}^\dagger b_{n',b} \\
& - \sum_n \gamma_0 (a_{n,b}^\dagger a_{n,t} + b_{n,b}^\dagger b_{n,t} + H.c.), \tag{6.11}
\end{aligned}$$

where the first two lines account for the NN and NNN intra-layer hopping in the t and b layers, respectively, and the third line represent inter-layer hopping.

In order to diagonalize  $\hat{H}$  and obtain the dispersion relations for AA-stacking bilayer graphene (BLG) nanoribbons, we may consider the modified time evolution of the creation and the annihilation operators  $a_i^\dagger$  ( $a_i$ ) and  $b_j^\dagger$  ( $b_j$ ), as calculated in the Heisenberg picture in quantum mechanics. In this case, the equations of motion (using the units with  $\hbar = 1$ ) for the annihilation operators  $a_i$  ( $b_j$ ) are as follows [44, 60, 37, 43, 48]:

$$\begin{aligned}
\frac{da_{n,t}}{dt} &= i[H, a_{n,t}] = i[H_t + H_b + H_i, a_{n,t}] \\
&= i \sum_{nn'} -\tau'(q_x) a_{n',t} - \tau(-q_x) b_{n',t} - \gamma_0 a_{n,b} \tag{6.12}
\end{aligned}$$

and

$$\begin{aligned}
\frac{db_{n,t}}{dt} &= i[H, b_{n,t}] = i[H_t + H_b + H_i, b_{n,t}] \\
&= i \sum_{nn'} -\tau'(q_x) b_{n',t} - \tau(q_x) a_{n',t} - \gamma_0 b_{n,b} \tag{6.13}
\end{aligned}$$

for the operators of the top layer. Similarly for the bottom layer we have

$$\begin{aligned}
\frac{da_{n,b}}{dt} &= i \sum_{nn'} -\tau'(q_x) a_{n',b} - \tau(-q_x) b_{n',b} - \gamma_0 a_{n,t} \\
\frac{db_{n,b}}{dt} &= i \sum_{nn'} -\tau'(q_x) b_{n',b} - \tau(q_x) a_{n',b} - \gamma_0 b_{n,t} \tag{6.14}
\end{aligned}$$



where Equation (6.5) was used.

The electronic dispersion relations of the double-layer graphene (i.e., energy or frequency versus wavevector) can now be obtained by solving the above operator equations of motion. Assuming, as before, that the coupled electronic modes behave like  $\exp[-i\omega(q_x)t]$ , on substituting this time dependent form into Equations 6.12-6.14, we get the following set of coupled equations:

$$\begin{aligned}
\omega(q_x)a_{n,t} &= \sum_{n'} \tau'_{nn'}(q_x)a_{n',t} + \tau_{nn'}(-q_x)b_{n',t} + \gamma_0 a_{n,b} \\
\omega(q_x)b_{n,t} &= \sum_{n'} \tau_{nn'}(q_x)a_{n',t} + \tau'_{nn'}(q_x)b_{n',t} + \gamma_0 b_{n,b} \\
\omega(q_x)a_{n,b} &= \sum_{n'} \tau'_{nn'}(q_x)a_{n',b} + \tau_{nn'}(-q_x)b_{n',b} + \gamma_0 a_{n,t} \\
\omega(q_x)b_{n,b} &= \sum_{n'} \tau_{nn'}(q_x)a_{n',b} + \tau'_{nn'}(q_x)b_{n',b} + \gamma_0 b_{n,t}
\end{aligned} \tag{6.15}$$

The above equations can be written in matrix form as follows:

$$\omega(q_x) \begin{bmatrix} a_{n,t} \\ b_{n,t} \\ a_{n,b} \\ b_{n,b} \end{bmatrix} = \begin{bmatrix} T'_t(q_x) & T_t(q_x) & U & 0 \\ T_t^*(q_x) & T'_t(q_x) & 0 & U \\ U & 0 & T'_b(q_x) & T_b(q_x) \\ 0 & U & T_b^*(q_x) & T'_b(q_x) \end{bmatrix} \begin{bmatrix} a_{n,t} \\ b_{n,t} \\ a_{n,b} \\ b_{n,b} \end{bmatrix} \tag{6.16}$$

where the solution of this matrix equation is given by the determinantal condition

$$\det \begin{bmatrix} -R(q_x)_t & T_t(q_x) & U & 0 \\ T_t^*(q_x) & -R(q_x)_t & 0 & U \\ U & 0 & -R(q_x)_b & T_b(q_x) \\ 0 & U & T_b^*(q_x) & -R(q_x)_b \end{bmatrix} = 0 \tag{6.17}$$

where we denote  $R(q_x)_t = \omega(q_x)I_N - T'_t(q_x)$ , and for each layer  $T(q_x)$  and  $T'(q_x)$  are the NN

and NNN interaction matrices respectively, which depend on the orientation of the ribbon, and  $\omega(q_x)$  are the energies of the modes. The matrix  $T(q_x)$  is given by

$$\begin{pmatrix} \alpha & \beta & 0 & 0 & \cdots \\ \beta & \alpha & \gamma & 0 & \cdots \\ 0 & \gamma & \alpha & \beta & \cdots \\ 0 & 0 & \beta & \alpha & \cdots \\ \vdots & \vdots & \vdots & \vdots & \ddots \end{pmatrix}. \quad (6.18)$$

whereas the NNN matrix  $T'(q_x)$  for zigzag ribbons is given by

$$\begin{pmatrix} \epsilon & 0 & \zeta & 0 & 0 & \cdots \\ 0 & \epsilon & 0 & \zeta & 0 & \cdots \\ \zeta & 0 & \epsilon & 0 & \zeta & \cdots \\ 0 & \zeta & 0 & \epsilon & 0 & \cdots \\ 0 & 0 & \zeta & 0 & \epsilon & \cdots \\ \vdots & \vdots & \vdots & \vdots & \vdots & \ddots \end{pmatrix} \quad (6.19)$$

and the matrix  $T'(q_x)$  for armchair ribbons is given by

$$\begin{pmatrix} 0 & \eta & \theta & 0 & 0 & \cdots \\ \eta & 0 & \eta & \theta & 0 & \cdots \\ \theta & \eta & 0 & \eta & \theta & \cdots \\ 0 & \theta & \eta & 0 & \eta & \cdots \\ 0 & 0 & \theta & \eta & 0 & \cdots \\ \vdots & \vdots & \vdots & \vdots & \vdots & \ddots \end{pmatrix} \quad (6.20)$$

Finally,  $U$  is the inter-layer hopping coupling matrix and it is given by

$$\begin{pmatrix} \gamma_0 & 0 & 0 & 0 & 0 & \cdots \\ 0 & \gamma_0 & 0 & 0 & 0 & \cdots \\ 0 & 0 & \gamma_0 & 0 & 0 & \cdots \\ 0 & 0 & 0 & \gamma_0 & 0 & \cdots \\ 0 & 0 & 0 & 0 & \gamma_0 & \cdots \\ \vdots & \vdots & \vdots & \vdots & \vdots & \ddots \end{pmatrix} \quad (6.21)$$

The parameters  $\alpha, \beta, \gamma, \epsilon, \zeta, \theta$  and  $\eta$  depend on the stripe edge geometry and are given in Tables 5.1 and 5.2.

In the special case that the NNN hopping  $t'$  can be neglected compared to the NN hopping  $t$ , the  $T'(q_x)$  matrix is equal to the zero matrix  $\mathbf{0}$  and Equation (6.17) simplifies to become

$$\det \begin{bmatrix} -\omega(q_x)I_N & T_t(q_x) & U & 0 \\ T_t^*(q_x) & -\omega(q_x)I_N & 0 & U \\ U & 0 & -\omega(q_x)I_N & T_b(q_x) \\ 0 & U & T_b^*(q_x) & -\omega(q_x)I_N \end{bmatrix} = 0 \quad (6.22)$$

The dispersion relations for the above graphene nanoribbons are next obtained numerically as the eigenvalues [89, 90] for the matrix Equation (6.16). Again, this is formally similar to Equation (3.13), and therefore the same numerical method used in Section 3.3 for analogous honeycomb magnetic stripes will be used here to get the required solutions. The effects of edges and impurities in each layer can be introduced into the numerical calculations just as in Chapters 4 and 5.

In the context of analogous bilayer magnetic materials, it is interesting to note that the

matrix Equation (6.16) can also be modified to apply to the 2D magnetic square lattice, taking into account the difference between it and the honeycomb lattice, including the existence of only one type of lattice site. Consequently the matrix size for the square lattice case is reduced to give the condition

$$\det \begin{bmatrix} -\omega(q_x)\alpha_t I_N + T'_t(q_x) + T_t(q_x) & U \\ U & -\omega(q_x)\alpha_b I_N + T'_b(q_x) + T_b(q_x) \end{bmatrix} = 0. \quad (6.23)$$

### 6.3 Numerical results

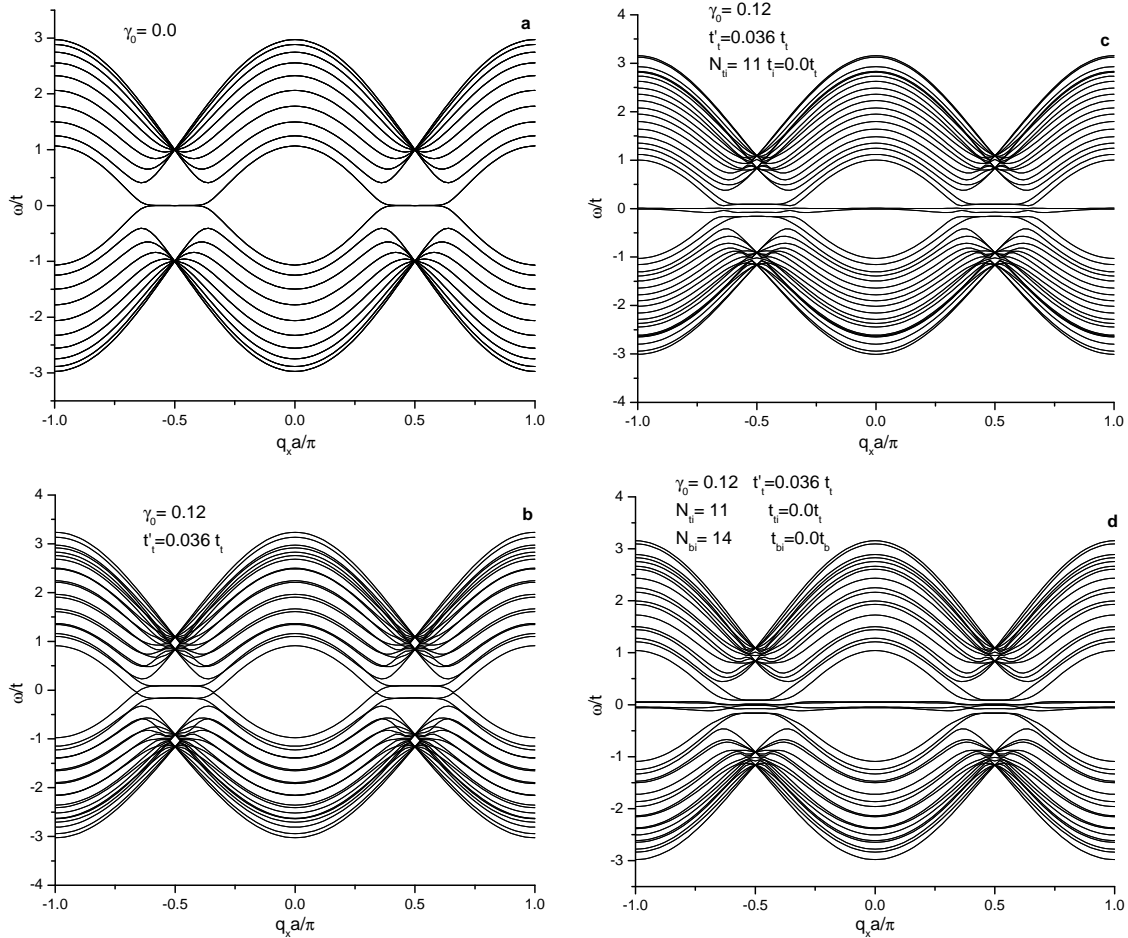


Figure 6.2: The tunable dispersion relations of AA-BLG nanoribbons with zigzag edge and width  $N = 20$ . (a)  $\gamma_0 = 0.0$  (b)  $\gamma_0 = 0.12$  and  $t' = 0.036t$  (c)  $\gamma_0 = 0.12$ ,  $t' = 0.036t$ ,  $N_{ii} = 11$ , and  $t_{ii} = 0.0t_t$  (d)  $\gamma_0 = 0.12$ ,  $t' = 0.036t$ ,  $N_{ii} = 11$ ,  $t_{ii} = 0.0t_t$ ,  $N_{bi} = 14$ , and  $t_{bi} = 0.0t_b$ .

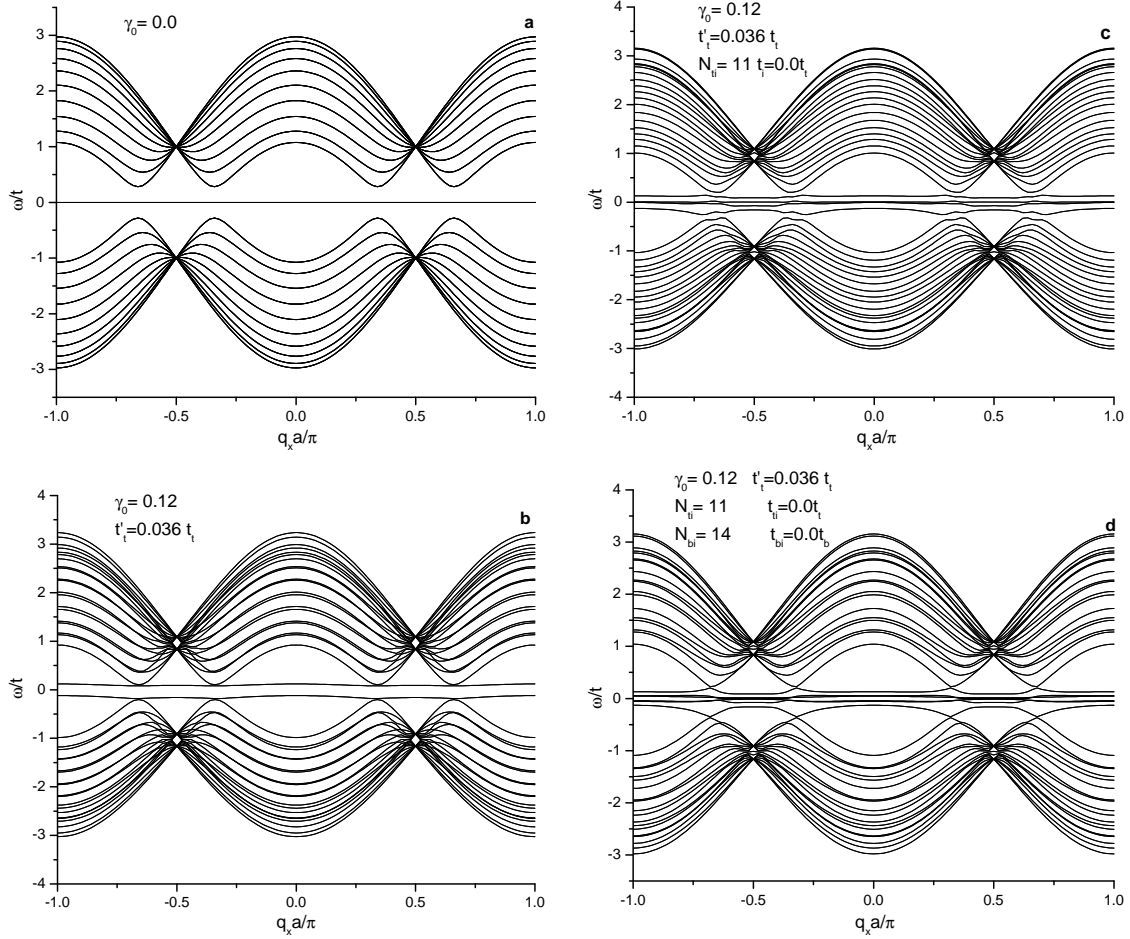


Figure 6.3: The tunable dispersion relations of AA-BLG nanoribbons with zigzag edge and width  $N = 21$ . (a)  $\gamma_0 = 0.0$  (b)  $\gamma_0 = 0.12$  and  $t' = 0.036t$  (c)  $\gamma_0 = 0.12$ ,  $t' = 0.036t$ ,  $N_{ii} = 11$ , and  $t_{ii} = 0.0t_t$  (d)  $\gamma_0 = 0.12$ ,  $t' = 0.036t$ ,  $N_{ii} = 11$ ,  $t_{ii} = 0.0t_t$ ,  $N_{bi} = 14$ , and  $t_{bi} = 0.0t_b$ .

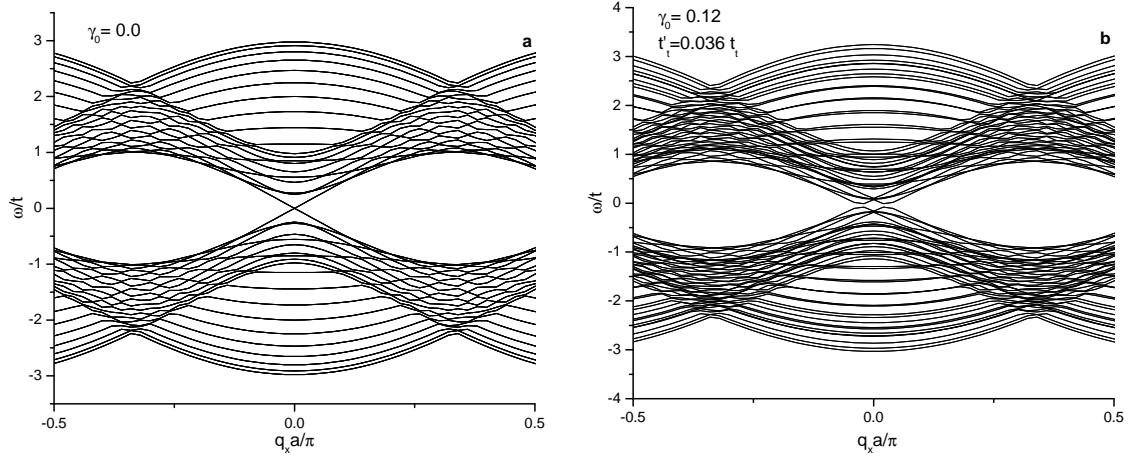


Figure 6.4: The tunable dispersion relations of AA-BLG nanoribbons with armchair edge and width  $N = 20$ . (a)  $\gamma_0 = 0.0$  (b)  $\gamma_0 = 0.12$  and  $t' = 0.036 t_1$ .

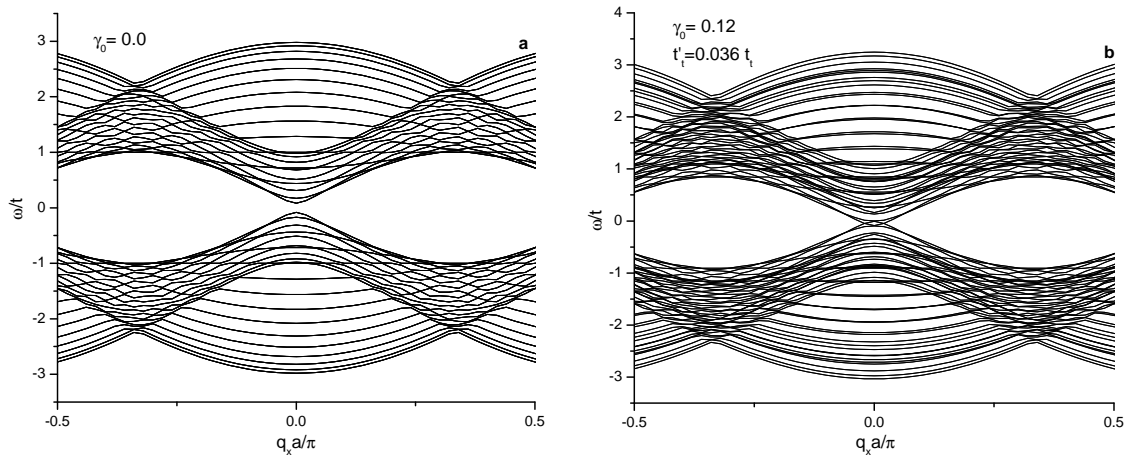


Figure 6.5: The tunable dispersion relations of AA-BLG nanoribbons with armchair edge and width  $N = 21$ . (a)  $\gamma_0 = 0.0$  (b)  $\gamma_0 = 0.12$  and  $t' = 0.036 t_1$ .

In this section the results for the 2D bilayer systems are presented so that a comparison can readily be made between the different structures (zigzag or armchair) and different interaction parameters (arising from the interlayer coupling strength, the range of in-plane hopping, and/or the presence of lines of impurities). These may be useful for controlling and tuning the mode properties in these ribbon structures, taking zigzag and armchair edged AA-BLG nanoribbons with all relevant cases for the width factor. As explained before, these consist of  $N$  even or odd for zigzag structures and  $N$  equal to  $2i$ ,  $2i + 1$ , or  $2i + 2$  for armchair structures. A brief

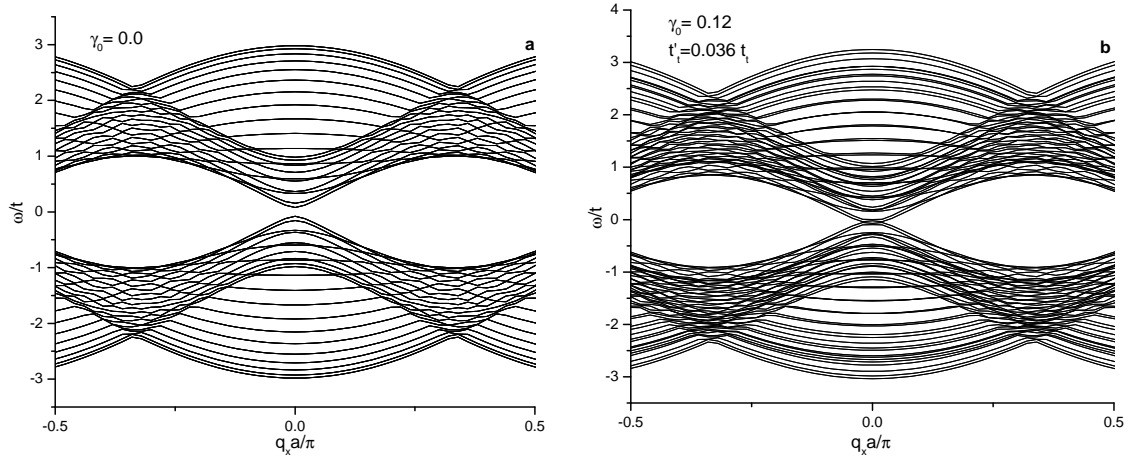


Figure 6.6: The tunable dispersion relations of AA-BLG nanoribbons with armchair edge and width  $N = 22$ . (a)  $\gamma_0 = 0.0$  (b)  $\gamma_0 = 0.12$  and  $t' = 0.036t$ .

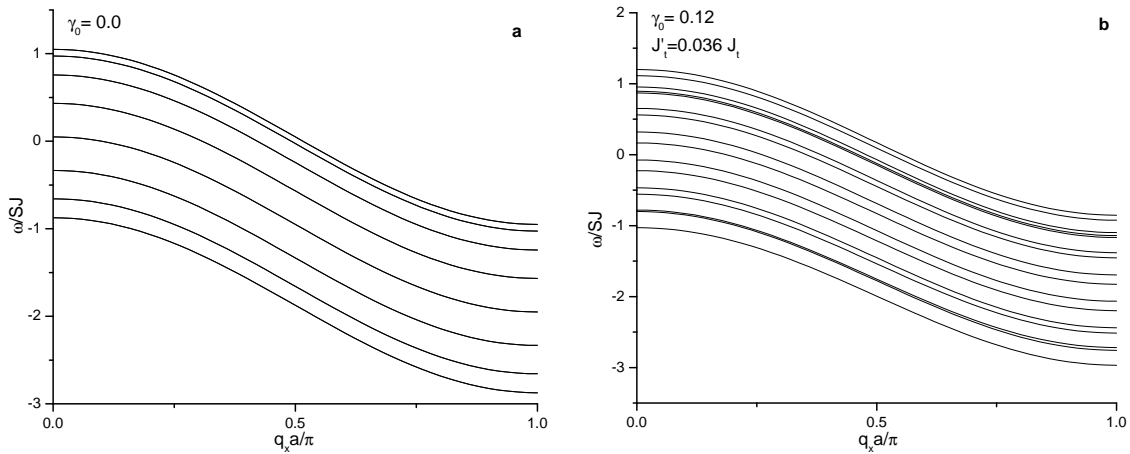


Figure 6.7: For comparison, the tunable dispersion relations of 2D square lattice magnetic stripes with width  $N = 8$ . (a)  $\gamma_0 = 0.0$  (b)  $\gamma_0 = 0.12$  and  $t' = 0.036t$ .

comparison will also be made with the analogous case of 2D magnetic square lattice stripes.

Figures 6.2-6.3 show some of the results obtained for the mode frequencies plotted versus the dimensionless wave vector, taking the above types of bilayer systems when the ribbon width is even ( $N = 20$ ) and odd ( $N = 21$ ), respectively, for the zigzag case. In each figure, panel (a) shows the dispersion relations of the bilayer systems when there is NN hopping within the layers and zero inter-layer NN coupling energy  $\gamma_0 = 0.0$ . Consequently, we obtain just the individual layer dispersion relations, but each mode is now doubly degenerate. Then panel (b)

in each figure shows the effect of introducing an asymmetry between the same coupled bilayer systems by choosing a nonzero value  $\gamma_0 = 0.12$  and including NNN hopping with  $t' = 0.036t$  in the top layer only. This results in an increased shift in frequency between the two layer modes and those of the single-layer case in all systems. We note that the wave-vector behavior of the modes near zero frequency is different in the odd and even  $N$  cases. Next, panel (c) in each of Figures 6.2 and 6.3 shows the effect of introducing a line of impurities at row 11 in the top layer only and with impurities hopping set equal to  $t_{ii} = 0.0t_t$ . This causes the introduction of extended flat localized impurities states at the Fermi level in the dispersion relations. Finally panel (d) shows the effect of introducing a second line of impurities, this time in the bottom layer, but now in a different row (chosen as row 14) and with impurities hopping equal to  $t_{bi} = 0.0t_b$ . This seems to result in an increased tendency towards degeneracy in the dispersion relations, compared with panel (c), for these zigzag-edge bilayer systems.

Next, in Figures 6.4-6.6, we show some of the analogous results obtained in the case of studying armchair-edge bilayer systems, taking width  $N$  equal to 20, 21, and 22, respectively. Panels (a) and (b) in each of these cases refer to similar situations as in the previous examples (i.e., the limit of uncoupled layers and the asymmetric case of coupled layers with NNN hopping in one of the layers). The interlayer coupling effects seem to be rather more significant for the case of  $N = 20$  compared with 21 or 22. We have also studied the effects of one or two lines of impurities. For brevity the results are not presented here, but they are broadly analogous to the zigzag case.

Finally, for comparison purposes, we show in Figure 6.7 some results to illustrate interlayer coupling in bilayer magnetic stripes with a square lattice structure, where the wavevector dependence of the SW modes is significantly different.



## 6.4 Discussion and Conclusions

In this chapter the AA-stacking bilayer graphene nanoribbons were used as an example of coupled bilayer systems which could be studied using the tight binding model. The tight binding model calculations for the AA-BLG nanoribbons show that the bilayer systems can be conveniently analyzed through an extension of the matrix direct diagonalization method used in earlier chapters. This is done by forming two block diagonal matrices with each block diagonal matrix representing the hopping terms within each individual layer. The effects of edges, NNN hopping and impurities of a single layer are introduced numerically as well as new terms for the interlayer coupling.

The bilayer results in this chapter can also be generalized to multilayered systems in general, provided they are formed by direct stacking of identical 2D layers with the same lattices and geometries as considered here.

The obtained dispersion relations for zigzag and armchair AA-BLG nanoribbons and magnetic square bilayer stripes show that the bilayer systems offer more flexibility with regards to the possibility of tuning their properties by changing parameters such as the interlayer hopping strength by changing the interlayer distance, adding different impurities configurations in individual layers, and changing the range of the interaction in individual layers. Also, the results show that the sensitivity of the bilayer systems to these parameters is strongly dependent on their lattice structure.

# Chapter 7

## Conclusions

In this thesis we have investigated the effects of the 2D lattice structures, the range of the interaction (with NN and NNN terms in general), the role of substitutional impurities, and the forming of bilayer systems in the electronic and the magnetic excitations in the 2D materials represented by zigzag and armchair graphene nanoribbons and the magnetic nanodots arrayed stripes (with either square lattice or honeycomb lattice).

The theoretical method employed throughout the thesis is based on the second quantization forms of both the tight-binding Hamiltonian (1.31) for electronic excitations and the Heisenberg Hamiltonian (1.48) for magnetic excitations. Both the NN exchange (hopping) interactions and the NNN exchange (hopping) interactions are incorporated in the respective Hamiltonians. In addition, for the magnetic cases the single-ion anisotropy and the Zeeman energy of an external magnetic field applied in the normal direction of stripes are also incorporated in the Heisenberg Hamiltonian.

In Chapter 2, the area and edge spin wave calculations were carried out using the Heisenberg Hamiltonian (1.48) and the tridiagonal matrix method for the 2D ferromagnetic square lattice stripes, where the SW modes can be characterized by a 1D in-plane wave vector  $q_x$ . An alternative matrix approach, referred to as the direct diagonalization method, is also employed

to advantage in these magnetic systems.

In Chapter 3, further spin wave calculations were carried out using the Heisenberg Hamiltonian (1.48) to study the allowed spin waves of zigzag and armchair edged stripes for ferromagnetic nanodots arrayed in a 2D honeycomb lattice. The calculations were achieved by extending the direct diagonalization method for the first time to apply to the honeycomb lattice structure. A much richer spectrum of spin waves was found (compared to the results in Chapter 2), leading to comparisons with the electronic excitations in graphene nanoribbons. We suggest that the fabrication of this magnetic counterpart to graphene may provide an exciting prospect for a new technology in the field of spintronic devices and magnetic applications.

In Chapter 4, which is applied to graphene, the tridiagonal method is again used, by building on results established in Chapter 3, to distinguish between edge modes and area modes and to study the behavior of edge localized states of a semi-infinite zigzag honeycomb sheet. The results show a realistic behavior for the dependence of edge localized states of zigzag graphene on the edge site parameters, allowing for an explanation of the experimental measurements of the local density of states at the edges of graphene [129]. At the same time it helps towards resolving some inconsistencies between the semiconductor behavior found in the experimental data for fabricated GNRs [125, 5] and the expected theoretical semi-metallic behavior as previously calculated without carefully considering the edge properties effect on the edge localized states [42, 41, 40, 33].

In Chapter 5, the effect of introducing NNN hopping is studied for graphene with its 2D honeycomb two-sublattice structure. It is found that introducing some small additional NNN hopping to the 2D materials removes the symmetry around the Fermi level and shifts it. This effect increases with increasing the NNN to NN hopping ratio. If the NNN hopping eventu-

ally becomes competitive with the NN hopping, the dispersion relations of the 2D materials are changed considerably from the NN hopping dispersion relations. The results show that the sensitivity of the 2D materials to the NNN hopping effect is much larger in the 2D honeycomb lattice than in the 2D square lattice. We therefore conclude that variations in the ratio between NNN and NN sites in the 2D lattice will lead, in principle, to the capability to tune the sensitivity for NNN hopping effects.

In Chapter 6, the tight binding model calculations are carried out for AA-BLG nanoribbons as an example of bilayer systems. The effects of edges, NNN hopping, and impurities of a single layer are introduced numerically as a change in the elements of the relevant block diagonal matrix appearing in the direct diagonalization method. The direct interlayer hopping between the top and the bottom single layers is constructed in the generalized direct diagonalization method by the off-diagonal block matrices in which the strength of the interlayer hopping is included.

There are several possible generalizations of this theoretical work on ribbons/stripes that could be carried within a similar matrix formalism of the tight binding model and/or the Heisenberg exchange model. Some of these are briefly described below.

One possible generalization is to consider different effects of impurities. For example, rather than having a line of substitutional impurities, it would be possible to consider single impurity sites or small clusters of impurities. The matrix formalism (particularly the direct diagonalization method) could be modified accordingly. Alternatively, other defects such as lattice vacancies (rather than substitutional impurities) could be taken into account. Another interesting area for future studies could involve generalizations of the bilayer work in Chapter 6. These calculations could include taking NNN interlayer coupling (as well as the NN terms)

for bilayers, different stacking schemes for the bilayers, or extensions of bilayer applications to multilayers. Finally, it would be possible to consider nanoribbons or stripes of finite length. This modification would remove the translational symmetry that we had along the  $x$  direction, but the effects would instead be treated in terms of using alternative matrix representations with larger dimension matrices.

In the author's opinion, the most novel aspect of this work is represented by Chapter 3, where theoretical results were derived for ferromagnetic nanoribbons (stripes) with a 2D hexagonal lattice structure, paralleling the geometry of graphene. Such a system could be produced as a magnetic nanodot array on a nonmagnetic substrate. It would be of interest to examine the temperature-dependent properties for this array.

# Bibliography

- [1] P. Rowley-Conwy, *From genesis to prehistory: the archaeological three age system and its contested reception in Denmark, Britain, and Ireland*. Oxford studies in the history of archaeology, Oxford University Press, 2007.
  
- [2] W. Kohn, “An essay on condensed matter physics in the twentieth century,” *Rev. Mod. Phys.*, vol. 71, pp. S59–S77, Mar 1999.
  
- [3] R. Kurzweil, “The law of accelerating returns,” *KurzweilAI.net*, 2001.
  
- [4] P. Avouris, Z. Chen, and V. Perebeinos, “Carbon-based electronics,” *Nat Nano*, vol. 2, pp. 605–615, Oct. 2007.
  
- [5] Z.-y. L. Bing Huang, Qi-min Yan and W. hui Duan, “Towards graphene nanoribbon-based electronics,” *Frontiers of Physics in China*, vol. 4, pp. 269–279, 9 2009.
  
- [6] J. E. Hill, *One-dimensional Electron Systems on Graphene Edges*. Thesis (ph.d.), The University of Texas at Austin, 2007.
  
- [7] A. Geim and A. MacDonald, “Graphene: Exploring carbon flatland,” *Physics Today*, pp. 35–41, 2007.

- [8] A. K. Geim and P. Kim, “Carbon wonderland,” *Scientific American*, pp. 90–97, April 2008.
- [9] P. A. Lee, N. Nagaosa, and X.-G. Wen, “Doping a mott insulator: Physics of high-temperature superconductivity,” *Rev. Mod. Phys.*, vol. 78, pp. 17–85, Jan 2006.
- [10] E. Dagotto, “Correlated electrons in high-temperature superconductors,” *Rev. Mod. Phys.*, vol. 66, pp. 763–840, Jul 1994.
- [11] G. Logvenov, A. Gozar, and I. Bozovic, “High-temperature superconductivity in a single copper-oxygen plane,” *Science*, vol. 326, no. 5953, pp. 699–702, 2009.
- [12] P. R. Wallace, “The band theory of graphite,” *Phys. Rev.*, vol. 71, pp. 622–634, May 1947.
- [13] J. W. McClure, “Diamagnetism of graphite,” *Phys. Rev.*, vol. 104, pp. 666–671, Nov 1956.
- [14] J. C. Slonczewski and P. R. Weiss, “Band structure of graphite,” *Phys. Rev.*, vol. 109, pp. 272–279, Jan 1958.
- [15] K. S. Novoselov, A. K. Geim, S. V. Morozov, D. Jiang, Y. Zhang, S. V. Dubonos, I. V. Grigorieva, and A. A. Firsov, “Electric field effect in atomically thin carbon films,” *Science*, vol. 306, no. 5696, pp. pp. 666–669, 2004.
- [16] A. Geim and K. Novoselov, “The rise of graphene,” *Nature Materials*, pp. 183–191, 2007.
- [17] A. K. Geim, “Graphene: Status and prospects,” *Nature Materials*, pp. 1530–1534, 2009.

- [18] H.-S. P. Wong and D. Akinwande, *Carbon Nanotube and Graphene Device Physics*. Cambridge University Press, 2011.
- [19] V. Singh, D. Joung, L. Zhai, S. Das, S. I. Khondaker, and S. Seal, “Graphene based materials: Past, present and future,” *Progress in Materials Science*, vol. 56, no. 8, pp. 1178 – 1271, 2011.
- [20] J. B.-K. Z. D.S.L. Abergel, V. Apalkov and T. Chakraborty, “Properties of graphene: a theoretical perspective,” *Advances in Physics*, vol. 59, no. 4, p. 261482, 2010.
- [21] Z. Chen, Y.-M. Lin, M. J. Rooks, and P. Avouris, “Graphene nano-ribbon electronics,” *Physica E: Low-dimensional Systems and Nanostructures*, vol. 40, no. 2, pp. 228 – 232, 2007. International Symposium on Nanometer-Scale Quantum Physics.
- [22] T. Chakraborty, “Graphene, nobel prize and all that jazz,” *Physics In Canada*, pp. 289–292, October 2010.
- [23] F. Schedin, A. K. Geim, S. V. Morozov, E. W. Hill, P. Blake, M. I. Katsnelson, and K. S. Novoselov, “Detection of individual gas molecules adsorbed on graphene,” *Nat Mater*, vol. 6, pp. 652–655, Sept. 2007.
- [24] Y.-M. Lin, A. Valdes-Garcia, S.-J. Han, D. B. Farmer, I. Meric, Y. Sun, Y. Wu, C. Dimitrakopoulos, A. Grill, P. Avouris, and K. A. Jenkins, “Wafer-scale graphene integrated circuit,” *Science*, vol. 332, no. 6035, pp. 1294–1297, 2011.
- [25] Y.-M. Lin, C. Dimitrakopoulos, K. A. Jenkins, D. B. Farmer, H.-Y. Chiu, A. Grill, and P. Avouris, “100-ghz transistors from wafer-scale epitaxial graphene,” *Science*, vol. 327, no. 5966, p. 662, 2010.



- [26] Y. Wang, X. Chen, Y. Zhong, F. Zhu, and K. P. Loh, "Large area, continuous, few-layered graphene as anodes in organic photovoltaic devices," *Applied Physics Letters*, vol. 95, no. 6, p. 063302, 2009.
- [27] P. Matyba, H. Yamaguchi, G. Eda, M. Chhowalla, L. Edman, and N. D. Robinson, "Graphene and mobile ions: The key to all-plastic, solution-processed light-emitting devices," *ACS Nano*, vol. 4, no. 2, pp. 637–642, 2010. PMID: 20131906.
- [28] S. Eigler, "A new parameter based on graphene for characterizing transparent, conductive materials," *Carbon*, vol. 47, no. 12, pp. 2936 – 2939, 2009.
- [29] L. Gomez De Arco, Y. Zhang, C. W. Schlenker, K. Ryu, M. E. Thompson, and C. Zhou, "Continuous, highly flexible, and transparent graphene films by chemical vapor deposition for organic photovoltaics," *ACS Nano*, vol. 4, no. 5, pp. 2865–2873, 2010. PMID: 20394355.
- [30] N. Mohanty and V. Berry, "Graphene-based single-bacterium resolution biodevice and dna transistor: Interfacing graphene derivatives with nanoscale and microscale biocomponents," *Nano Letters*, vol. 8, no. 12, pp. 4469–4476, 2008.
- [31] W. Hu, C. Peng, W. Luo, M. Lv, X. Li, D. Li, Q. Huang, and C. Fan, "Graphene-based antibacterial paper," *ACS Nano*, vol. 4, no. 7, pp. 4317–4323, 2010.
- [32] Y. H. Wu, T. Yu, and Z. X. Shen, "Two-dimensional carbon nanostructures: Fundamental properties, synthesis, characterization, and potential applications," *Journal of Applied Physics*, vol. 108, no. 7, p. 071301, 2010.

- [33] A. H. Castro Neto, F. Guinea, N. M. R. Peres, K. S. Novoselov, and A. K. Geim, "The electronic properties of graphene," *Rev. Mod. Phys.*, vol. 81, pp. 109–162, Jan 2009.
- [34] P. Y. Bruice, *Organic Chemistry*. Prentice Hall, 3rd ed., 2001.
- [35] L. A. N. Laboratory., "Periodic table of elements." online.
- [36] J. M. Stphanie Reich, Christian Thomsen, *Carbon nanotubes: basic concepts and physical properties*. Wiley-VCH, 2004.
- [37] L. Kantorovich, *Quantum Theory of the Solid State: An Introduction*. Springer, 2004.
- [38] M. S. D. Riichiro Saito, G. Dresselhaus, *Physical properties of carbon nanotubes*. Imperial College Press, 1998.
- [39] R. N. Costa Filho, G. A. Farias, and F. M. Peeters, "Graphene ribbons with a line of impurities: Opening of a gap," *Phys. Rev. B*, vol. 76, p. 193409, Nov 2007.
- [40] M. Fujita, K. Wakabayashi, K. Nakada, and K. Kusakabe, "Peculiar localized state at zigzag graphite edge," *Journal of the Physical Society of Japan*, vol. 65, no. 7, pp. 1920–1923, 1996.
- [41] K. Wakabayashi, M. Fujita, H. Ajiki, and M. Sigrist, "Electronic and magnetic properties of nanographite ribbons," *Phys. Rev. B*, vol. 59, pp. 8271–8282, Mar 1999.
- [42] K. Nakada, M. Fujita, G. Dresselhaus, and M. S. Dresselhaus, "Edge state in graphene ribbons: Nanometer size effect and edge shape dependence," *Phys. Rev. B*, vol. 54, pp. 17954–17961, Dec 1996.

- [43] U. Rssler, *Solid State Theory: An Introduction*. Springer, 2009.
- [44] D. R. Bs, *Quantum mechanics: a modern and concise introductory course*. Springer, 2007.
- [45] C. Bena and G. Montambaux, “Remarks on the tight-binding model of graphene,” *New Journal of Physics*, vol. 11, no. 9, p. 095003, 2009.
- [46] A. Altland and B. Simons, *Condensed matter field theory*. Cambridge University Press, 2ed ed., 2010.
- [47] S. Reich, J. Maultzsch, C. Thomsen, and P. Ordejón, “Tight-binding description of graphene,” *Phys. Rev. B*, vol. 66, p. 035412, Jul 2002.
- [48] K. F. Henrik Bruus, *Many-body quantum theory in condensed matter physics: an introduction*. Oxford University Press, 2004.
- [49] R. S. Deacon, K.-C. Chuang, R. J. Nicholas, K. S. Novoselov, and A. K. Geim, “Cyclotron resonance study of the electron and hole velocity in graphene monolayers,” *Phys. Rev. B*, vol. 76, p. 081406, Aug 2007.
- [50] A. T. Boothroyd, P. Babkevich, D. Prabhakaran, and P. G. Freeman, “An hour-glass magnetic spectrum in an insulating, hole-doped antiferromagnet,” *Nature*, vol. 471, pp. 341–344, Mar. 2011.
- [51] T. Dahm, V. Hinkov, S. V. Borisenko, A. A. Kordyuk, V. B. Zabolotnyy, J. Fink, B. Buchner, D. J. Scalapino, W. Hanke, and B. Keimer, “Strength of the spin-fluctuation-

- mediated pairing interaction in a high-temperature superconductor,” *Nat Phys*, vol. 5, pp. 217–221, Mar. 2009.
- [52] W. Guo and R. Han, “Spin pairing: the magnetic origin of high- $t_c$  superconductivity,” *Physica C: Superconductivity*, vol. 364-365, pp. 79 – 86, 2001.
- [53] K. Hida, “A spin wave theory of the high- $t_c$  oxide superconductor,” *Journal of the Physical Society of Japan*, vol. 57, no. 5, pp. 1544–1547, 1988.
- [54] A. P. Daniel D. Stancil, *Spin Waves: Theory and Applications*. Springer, 2009.
- [55] M. T. Nguyen, *Spin-wave excitations in ferromagnetic nanostructures*. PhD thesis, University of Western Ontario, 2007.
- [56] I. Žutić, J. Fabian, and S. Das Sarma, “Spintronics: Fundamentals and applications,” *Rev. Mod. Phys.*, vol. 76, pp. 323–410, Apr 2004.
- [57] S. D. Sarma, “Spintronics,” *American Scientist*, vol. 89, pp. 516–523, 2001.
- [58] P. Mohn, *Magnetism in the Solid State: An Introduction*. Springer, 2 ed., 2006.
- [59] J. Stohr and H. Siegmann, *Magnetism From Fundamentals to Nanoscale Dynamics*. Springer, 1 ed., 2006.
- [60] R. L. Liboff, *Introductory Quantum Mechanics*. Longman Higher Education, 1 ed., 1987.
- [61] C. Kittel, *Introduction to solid state physics*. Wiley, 2005.

- [62] M. Cottam and D. Tilley, *Introduction to Surface and Superlattice Excitations*. IOP Publishing, 2 ed., 2004.
- [63] H. T. Nguyen, *Dipole-Exchange Spin Waves in Magnetic Nanomaterials*. Phd, The University of Western Ontario, 2009.
- [64] E. Meloche, *Spin-wave properties in anisotropic magnetic materials*. PhD thesis, University of Western Ontario, 2006.
- [65] F. Bloch, “Zur theorie des ferromagnetismus,” *Z. Physik*, vol. 61, p. 206, 1930.
- [66] T. Holstein and H. Primakoff, “Field dependence of the intrinsic domain magnetization of a ferromagnet,” *Phys. Rev.*, vol. 58, pp. 1098–1113, Dec 1940.
- [67] L. Passell, O. W. Dietrich, and J. Als-Nielsen, “Neutron scattering from the heisenberg ferromagnets euo and eus. i. the exchange interactions,” *Phys. Rev. B*, vol. 14, pp. 4897–4907, Dec 1976.
- [68] A. Katanin and O. P. Sushkov, “Quasielastic neutron scattering from two-dimensional antiferromagnets at a finite temperature,” *Phys. Rev. B*, vol. 83, p. 094426, Mar 2011.
- [69] N. Tsyrlin, F. Xiao, A. Schneidewind, P. Link, H. M. Rønnow, J. Gavilano, C. P. Landee, M. M. Turnbull, and M. Kenzelmann, “Two-dimensional square-lattice  $s = \frac{1}{2}$  antiferromagnet  $cu(pz)_2(clo_4)_2$ ,” *Phys. Rev. B*, vol. 81, p. 134409, Apr 2010.
- [70] M. D. Lumsden, S. E. Nagler, B. C. Sales, D. A. Tennant, D. F. McMorrow, S.-H. Lee, and S. Park, “Magnetic excitation spectrum of the square lattice  $s = 1/2$  heisenberg antiferromagnet  $k_2v_3o_8$ ,” *Phys. Rev. B*, vol. 74, p. 214424, Dec 2006.

- [71] J. Cervenka, M. I. Katsnelson, and C. F. J. Flipse, “Room-temperature ferromagnetism in graphite driven by two-dimensional networks of point defects,” *Nat Phys*, vol. 5, pp. 840–844, Nov. 2009.
- [72] R. Allenspach, “Ultrathin films: magnetism on the microscopic scale,” *Journal of Magnetism and Magnetic Materials*, vol. 129, no. 2-3, pp. 160 – 185, 1994.
- [73] D. P. Arovas and A. Auerbach, “Functional integral theories of low-dimensional quantum heisenberg models,” *Phys. Rev. B*, vol. 38, pp. 316–332, Jul 1988.
- [74] D. Yoshioka, “Boson mean field theory of the square lattice heisenberg model,” *Journal of the Physical Society of Japan*, vol. 58, no. 10, pp. 3733–3745, 1989.
- [75] S. Chakravarty, B. I. Halperin, and D. R. Nelson, “Two-dimensional quantum heisenberg antiferromagnet at low temperatures,” *Phys. Rev. B*, vol. 39, pp. 2344–2371, Feb 1989.
- [76] V. Y. Irkhin, A. A. Katanin, and M. I. Katsnelson, “Self-consistent spin-wave theory of layered heisenberg magnets,” *Phys. Rev. B*, vol. 60, pp. 1082–1099, Jul 1999.
- [77] M. Takahashi, “Modified spin-wave theory of a square-lattice antiferromagnet,” *Phys. Rev. B*, vol. 40, pp. 2494–2501, Aug 1989.
- [78] J. J. Milton Pereira, *Microscopic theory of exchange and dipole-exchange spin waves in magnetic thin films*. PhD thesis, The University of Western Ontario, 2001.
- [79] M. G. Pereira, J. Milton; Cottam, “Theory of dipole-exchange spin waves in ultrathin antiferromagnetic films,” *Journal of Applied Physics*, vol. 85, no. 8, pp. 4949–4951, 1999.

- [80] V. V. Kruglyak, S. O. Demokritov, and D. Grundler, “Magnonics,” *Journal of Physics D: Applied Physics*, vol. 43, no. 26, p. 264001, 2010.
- [81] B. Hillebrands and A. Thiaville, eds., *Spin Dynamics in Confined Magnetic Structures I*, Springer, 2002.
- [82] B. Hillebrands and K. Ounadjela, eds., *Spin Dynamics in Confined Magnetic Structures II*, Springer, 2003.
- [83] B. Hillebrands and A. Thiaville, eds., *Spin Dynamics in Confined Magnetic Structures III*, Springer, 2006.
- [84] R. N. C. Filho, U. M. S. Costa, and M. G. Cottam, “Green function theory for a magnetic impurity layer in a semi-infinite transverse ising model,” *Journal of Magnetism and Magnetic Materials*, vol. 213, no. 1-2, pp. 195 – 200, 2000.
- [85] M. G. Cottam and D. E. Kontos, “The spin correlation functions of a finite-thickness ferromagnetic slab,” *Journal of Physics C: Solid State Physics*, vol. 13, no. 15, pp. 2945–2958, 1980.
- [86] M. G. Cottam, “The spin correlation functions of a semi-infinite heisenberg ferromagnet,” *Journal of Physics C: Solid State Physics*, vol. 9, no. 11, pp. 2121–2136, 1976.
- [87] R. E. De Wames and T. Wolfram, “Theory of surface spin waves in the heisenberg ferromagnet,” *Phys. Rev.*, vol. 185, pp. 720–727, Sep 1969.

- [88] P. R. L. Heron, *Theory of spin waves in Heisenberg ferromagnetic and antiferromagnetic thin films with nonuniaxial single-ion anisotropy*. Thesis (ph.d.), Faculty of Graduate Studies, University of Western Ontario, London, Ont., 1995.
- [89] J. R. M. Karim M. Abadir, *Matrix algebra*, vol. 1. Cambridge University Press, 2005.
- [90] W. H. Press, *Numerical recipes in FORTRAN :the art of scientific computing*, vol. 1. Cambridge England ; New York: Cambridge University Press, 1992.
- [91] C. F. Gerald and P. O. Wheatley, *Applied numerical analysis*. Reading, Mass.: Addison-Wesley, 1999.
- [92] M. Ahmed, "Understanding of hopping matrix for 2d materials taking 2d honeycomb and square lattices as study cases," *arXiv1110.6488v1*, 2011.
- [93] N. S. Headings, S. M. Hayden, R. Coldea, and T. G. Perring, "Anomalous high-energy spin excitations in the high- $t_c$  superconductor-parent antiferromagnet  $la_2cuo_4$ ," *Phys. Rev. Lett.*, vol. 105, p. 247001, Dec 2010.
- [94] M. Guarise, B. Dalla Piazza, M. Moretti Sala, G. Ghiringhelli, L. Braicovich, H. Berger, J. N. Hancock, D. van der Marel, T. Schmitt, V. N. Strocov, L. J. P. Ament, J. van den Brink, P.-H. Lin, P. Xu, H. M. Rønnow, and M. Grioni, "Measurement of magnetic excitations in the two-dimensional antiferromagnetic  $sr_2cuo_2cl_2$  insulator using resonant x-ray scattering: Evidence for extended interactions," *Phys. Rev. Lett.*, vol. 105, p. 157006, Oct 2010.



- [95] R. Coldea, S. M. Hayden, G. Aeppli, T. G. Perring, C. D. Frost, T. E. Mason, S.-W. Cheong, and Z. Fisk, “Spin waves and electronic interactions in  $la_2cuo_4$ ,” *Phys. Rev. Lett.*, vol. 86, pp. 5377–5380, Jun 2001.
- [96] K. Hida, “A spin wave theory of the high- $t_c$  oxide superconductor,” *Journal of the Physical Society of Japan*, vol. 57, no. 5, pp. 1544–1547, 1988.
- [97] G. Wei and H. Ru-Shan, “Electron spin pairing and the phase diagram of high-  $t_c$  superconductors,” *Chinese Physics Letters*, vol. 18, no. 10, p. 1398, 2001.
- [98] W. Guo and R. Han, “Spin pairing: the magnetic origin of high- $t_c$  superconductivity,” *Physica C: Superconductivity*, vol. 364-365, pp. 79 – 86, 2001.
- [99] Z. L. G.M. Zhang and T. Xiang, “Superconductivity mediated by the antiferromagnetic spin-wave in chalcogenide iron-base superconductors,” Feb 2011.
- [100] J. Zhao, D. T. Adroja, D.-X. Yao, R. Bewley, S. Li, X. F. Wang, G. Wu, X. H. Chen, J. Hu, and P. Dai, “Spin waves and magnetic exchange interactions in  $cafe_2as_2$ ,” *Nat Phys*, vol. 5, pp. 555–560, Aug. 2009.
- [101] O. V. Yazyev, “Emergence of magnetism in graphene materials and nanostructures,” *Reports on Progress in Physics*, vol. 73, no. 5, p. 056501, 2010.
- [102] M. Mecklenburg and B. C. Regan, “Spin and the honeycomb lattice: Lessons from graphene,” *Phys. Rev. Lett.*, vol. 106, p. 116803, Mar 2011.
- [103] R. S. E.O. Kamenetskii and M. Sigalov, “Magnetic artificial atoms based on thin-film ferrite disk particles,” Mar 2003.

- [104] M. Rontani, “Artificial atoms: Shape the wave,” *Nat Mater*, vol. 10, pp. 173–175, Mar. 2011.
- [105] O. Astafiev, K. Inomata, A. O. Niskanen, T. Yamamoto, Y. A. Pashkin, Y. Nakamura, and J. S. Tsai, “Single artificial-atom lasing,” *Nature*, vol. 449, pp. 588–590, Oct. 2007.
- [106] R. Bratschitsch and A. Leitenstorfer, “Quantum dots: Artificial atoms for quantum optics,” *Nat Mater*, vol. 5, pp. 855–856, Nov. 2006.
- [107] M. A. Kastner, “Artificial atoms,” *Physics Today*, vol. 46, p. 24, 1993.
- [108] L. Malkinski, R. E. Camley, Z. Celinski, T. A. Winningham, S. G. Whipple, and K. Douglas, “Hexagonal lattice of 10-nm magnetic dots,” *Journal of Applied Physics*, vol. 93, no. 10, pp. 7325–7327, 2003.
- [109] M. Tanaka, E. Saitoh, H. Miyajima, T. Yamaoka, and Y. Iye, “Magnetic interactions in a ferromagnetic honeycomb nanoscale network,” *Phys. Rev. B*, vol. 73, p. 052411, Feb 2006.
- [110] M. Stepanova and S. Dew, *Nanofabrication: Techniques and Principles*. Springer, 2011.
- [111] J. Richter, J. Schulenburg, and A. Honecker, “Quantum magnetism in two dimensions: From semi-classical néel order to magnetic disorder,” in *Quantum Magnetism* (U. Schollwck, J. Richter, D. Farnell, and R. Bishop, eds.), vol. 645 of *Lecture Notes in Physics*, pp. 85–153, Springer Berlin / Heidelberg, 2004. 10.1007/BFb0119592.
- [112] H. S. Darendelioglu, “Magnetization process in honeycomb lattice,” *Scripta Metallurgica et Materialia*, vol. 33, no. 10-11, pp. 1825 – 1829, 1995.

- [113] J. Oitmaa, C. J. Hamer, and Z. Weihong, "Quantum magnets on the honeycomb and triangular lattices at  $t=0$ ," *Phys. Rev. B*, vol. 45, pp. 9834–9841, May 1992.
- [114] J. D. Reger, J. A. Riera, and A. P. Young, "Monte carlo simulations of the spin-  $1/2$  heisenberg antiferromagnet in two dimensions," *Journal of Physics: Condensed Matter*, vol. 1, no. 10, p. 1855, 1989.
- [115] A. A. Tsirlin, O. Janson, and H. Rosner, " $\beta - \text{Cu}_2\text{V}_2\text{O}_7$  : A spin-  $\frac{1}{2}$  honeycomb lattice system," *Phys. Rev. B*, vol. 82, p. 144416, Oct 2010.
- [116] E. Rastelli and A. Tassi, "Hexagonal spin lattice with ferromagnetic intrachain and anti-ferromagnetic interchain couplings in an external magnetic field," *Phys. Rev. B*, vol. 49, pp. 9679–9687, Apr 1994.
- [117] H. Zheng, Z. F. Wang, T. Luo, Q. W. Shi, and J. Chen, "Analytical study of electronic structure in armchair graphene nanoribbons," *Phys. Rev. B*, vol. 75, p. 165414, Apr 2007.
- [118] M. Ezawa, "Peculiar width dependence of the electronic properties of carbon nanoribbons," *Phys. Rev. B*, vol. 73, p. 045432, Jan 2006.
- [119] S. Gopalan, T. M. Rice, and M. Sgrist, "Spin ladders with spin gaps: A description of a class of cuprates," *Phys. Rev. B*, vol. 49, pp. 8901–8910, Apr 1994.
- [120] M. Fabrizio, A. Parola, and E. Tosatti, "Strong-coupling phases of two hubbard chains with interchain hopping," *Phys. Rev. B*, vol. 46, pp. 3159–3162, Aug 1992.
- [121] K. C. M. O. H. Hosoya, H. Kumazaki and Y.-D. Gao, "How do the polycyclic aromatic hydrocarbons approach infinity?," *Pure Appl. Chem.*, vol. 62, no. 3, pp. 445–450, 1990.

- [122] M. Y. Han, B. Özyilmaz, Y. Zhang, and P. Kim, “Energy band-gap engineering of graphene nanoribbons,” *Phys. Rev. Lett.*, vol. 98, p. 206805, May 2007.
- [123] Y.-W. Son, M. L. Cohen, and S. G. Louie, “Energy gaps in graphene nanoribbons,” *Phys. Rev. Lett.*, vol. 97, p. 216803, Nov 2006.
- [124] X. Jia, J. Campos-Delgado, M. Terrones, V. Meunier, and M. S. Dresselhaus, “Graphene edges: a review of their fabrication and characterization,” *Nanoscale*, vol. 3, pp. 86–95, 2011.
- [125] X. Wang, Y. Ouyang, X. Li, H. Wang, J. Guo, and H. Dai, “Room-temperature all-semiconducting sub-10-nm graphene nanoribbon field-effect transistors,” *Phys. Rev. Lett.*, vol. 100, p. 206803, May 2008.
- [126] R. E. De Wames and T. Wolfram, “Surface spin waves in the heisenberg antiferromagnet with changes in exchange and anisotropy constants at the surface,” *Phys. Rev.*, vol. 185, pp. 752–759, Sep 1969.
- [127] R. N. C. Filho, U. M. S. Costa, and M. G. Cottam, “Green function theory for a magnetic impurity layer in a semi-infinite transverse ising model,” *J. Magn. Magn. Mater.*, vol. 213, no. 1-2, pp. 195 – 200, 2000.
- [128] B. Xu, J. Yin, Y. D. Xia, X. G. Wan, K. Jiang, and Z. G. Liu, “Electronic and magnetic properties of zigzag graphene nanoribbon with one edge saturated,” *Applied Physics Letters*, vol. 96, no. 16, p. 163102, 2010.
- [129] Z. Klusek, W. Kozłowski, Z. Waqar, S. Datta, J. Burnell-Gray, I. Makarenko, N. Gall, E. Rutkov, A. Tontegode, and A. Titkov, “Local electronic edge states of graphene layer

- deposited on ir(111) surface studied by stm/cits,” *Applied Surface Science*, vol. 252, no. 5, pp. 1221 – 1227, 2005.
- [130] J. Barrios-Vargas and G. G. Naumis, “Electrical conductivity and resonant states of doped graphene considering next-nearest neighbor interaction,” Mar 2011.
- [131] Y. V. Skrypnik and V. M. Loktev, “Impurity effects in a two-dimensional system with the dirac spectrum,” *Phys. Rev. B*, vol. 73, p. 241402, Jun 2006.
- [132] K. Sun, Z. Gu, H. Katsura, and S. Das Sarma, “Nearly flatbands with nontrivial topology,” *Phys. Rev. Lett.*, vol. 106, p. 236803, Jun 2011.
- [133] D. S. Xue, M. Z. Gao, J. B. Yang, Y. Kong, and F. S. Li, “Spin waves of anisotropic ferromagnets with nearest neighbor and next-nearest neighbor interactions,” *physica status solidi (b)*, vol. 193, no. 1, pp. 161–166, 1996.
- [134] M. S. Seehra and T. M. Giebultowicz, “Magnetic structures of fcc systems with nearest-neighbor and next-nearest-neighbor exchange interactions,” *Phys. Rev. B*, vol. 38, pp. 11898–11900, Dec 1988.
- [135] E. V. Castro, K. S. Novoselov, S. V. Morozov, N. M. R. Peres, J. M. B. L. dos Santos, J. Nilsson, F. Guinea, A. K. Geim, and A. H. C. Neto, “Electronic properties of a biased graphene bilayer,” *Journal of Physics: Condensed Matter*, vol. 22, no. 17, p. 175503, 2010.
- [136] H. Xu, T. Heinzl, and I. V. Zozoulenko, “Edge disorder and localization regimes in bilayer graphene nanoribbons,” *Phys. Rev. B*, vol. 80, p. 045308, Jul 2009.

- [137] G. Kalon, Y. J. Shin, and H. Yang, “Tunable metal–insulator transitions in bilayer graphene by thermal annealing,” *Applied Physics Letters*, vol. 98, no. 23, p. 233108, 2011.
- [138] G. Trambly de Laissardiere, D. Mayou, and L. Magaud, “Localization of dirac electrons in rotated graphene bilayers,” *Nano Letters*, vol. 10, no. 3, pp. 804–808, 2010. PMID: 20121163.
- [139] T. Ohta, A. Bostwick, T. Seyller, K. Horn, and E. Rotenberg, “Controlling the electronic structure of bilayer graphene,” *Science*, vol. 313, no. 5789, pp. 951–954, 2006.
- [140] Z. Liu, K. Suenaga, P. J. F. Harris, and S. Iijima, “Open and closed edges of graphene layers,” *Phys. Rev. Lett.*, vol. 102, p. 015501, Jan 2009.
- [141] O. Fang-Ping, C. Li-Jian, X. Jin, and Z. Hua, “Electronic properties of bilayer zigzag graphene nanoribbons: First principles study,” *Chinese Physics Letters*, vol. 28, no. 4, p. 047304, 2011.
- [142] X. Chang, Y. Ge, and J. M. Dong, “Ripples of a a and a b stacking bilayer graphenes,” *The European Physical Journal B - Condensed Matter and Complex Systems*, vol. 78, pp. 103–109, 2010. 10.1140/epjb/e2010-10498-8.
- [143] P. L. de Andres, R. Ramírez, and J. A. Vergés, “Strong covalent bonding between two graphene layers,” *Phys. Rev. B*, vol. 77, p. 045403, Jan 2008.
- [144] L. Jiang, *Quantum Theory of Spin-Wave Excitations in Ferromagnetic Layered Structures*. PhD thesis, The University of Western Ontario, 1996.

- [145] A. Belkin, V. Novosad, M. Iavarone, J. Pearson, and G. Karapetrov, “Superconductor/ferromagnet bilayers: Influence of magnetic domain structure on vortex dynamics,” *Phys. Rev. B*, vol. 77, p. 180506, May 2008.
- [146] G. Beutier, G. van der Laan, K. Chesnel, A. Marty, M. Belakhovsky, S. P. Collins, E. Dudzik, J.-C. Toussaint, and B. Gilles, “Characterization of fepd bilayers and trilayers using soft x-ray resonant magnetic scattering and micromagnetic modeling,” *Phys. Rev. B*, vol. 71, p. 184436, May 2005.
- [147] G. Carapella, V. Granata, F. Russo, and G. Costabile, “Bistable abrikosov vortex diode made of a py–nb ferromagnet-superconductor bilayer structure,” *Applied Physics Letters*, vol. 94, no. 24, p. 242504, 2009.

# Appendix A

## Algorithms used in Chapter 2

In this appendix we list the Algorithms used in writing the Fortran code to calculate some of the numerical results. Specifically, Algorithm 1 describes the procedure followed for obtaining the roots of the polynomials for  $x$  in Section 2.3. Algorithm 2 describes the next step followed in Section 2.4 to find the SW dispersion relations.

### A.1 Algorithm 1

1. Enter the value of  $N$
2. Begin a loop for scanning the values of  $\Delta$  from -3 to 3
3. Evaluate the first polynomial 2.26
4. Find the minimum positive values of  $\Delta$  that satisfying (2.28)
5. Find the maximum negative values of  $\Delta$  that satisfying (2.28)
6. Evaluate the second polynomial 2.27
7. Find the minimum positive values of  $\Delta$  that satisfying (2.28)
8. Find the maximum negative values of  $\Delta$  that satisfying (2.28)



9. End the loop

## A.2 Algorithm 2

1. Enter the value of  $N$
2. Begin a loop for scanning the values of  $q_x a$  from 0 to  $\pi$
3. Compute  $\Delta$  for  $q_x a$  using the above physical parameters
4. Compute all solutions of  $x$  for a given  $N$  and  $\Delta(q_x a)$
5. Filter the solutions of  $x$  according to boundary and physical conditions  
(2.28)
6. Compute the frequency from  $x + x^{-1} = a$
7. End the loop

# Appendix B

## Derivation of Equation (4.6)

In this appendix we outline the main steps in using Equation (4.5) to obtain Equation (4.6). These results are required for the derivation of the dispersion relations for the edge states and impurity states of graphene in Section 4.2. The starting point from Equation (4.5) is

$$\begin{aligned}\omega(q_x)a_{q_x,n} &= \sum_{q_x,n'} \tau_{nn'}(-q_x)b_{q_x,n'} \\ \omega(q_x)b_{q_x,n'} &= \sum_{q_x,n} \tau_{n'n}(q_x)a_{q_x,n}.\end{aligned}$$

Next the above coupled equations are expanded using the sublattice indexes  $n$  and  $n'$

$$\begin{aligned}\omega(q_x)a_{q_x,1} &= \beta b_{q_x,1} \\ \omega(q_x)a_{q_x,2} &= \gamma b_{q_x,1} + \beta b_{q_x,2} \\ \omega(q_x)a_{q_x,3} &= \gamma b_{q_x,2} + \beta b_{q_x,3} \\ &\vdots \\ \omega(q_x)a_{q_x,n} &= \gamma b_{q_x,n'-1} + \beta b_{q_x,n'}\end{aligned}$$

$$\omega(q_x)b_{q_x,1} = \beta a_{q_x,1} + \gamma a_{q_x,2}$$

$$\omega(q_x)b_{q_x,2} = \beta a_{q_x,2} + \gamma a_{q_x,3}$$

$$\omega(q_x)b_{q_x,3} = \beta a_{q_x,3} + \gamma a_{q_x,4}$$

$$\vdots$$

$$\omega(q_x)b_{q_x,n'} = \beta a_{q_x,n} + \gamma a_{q_x,n+1}$$

We then divide by  $\omega(q_x)$ , and after rearranging we get

$$b_{q_x,n'} - \frac{\gamma}{\omega(q_x)}a_{q_x,n} - \frac{\beta}{\omega(q_x)}a_{q_x,n+1} = 0$$

$$\omega(q_x)b_{q_x,n'} = \beta a_{q_x,n} + \gamma a_{q_x,n+1}$$

$$\omega(q_x)b_{q_x,n'-1} = \beta a_{q_x,n-1} + \gamma a_{q_x,n}$$

$$\omega(q_x)a_{q_x,n} = \gamma b_{q_x,n'-1} + \beta b_{q_x,n'}$$

$$\omega(q_x)a_{q_x,n} = \gamma \frac{\beta a_{q_x,n-1} + \gamma a_{q_x,n}}{\omega(q_x)} + \beta \frac{\beta a_{q_x,n} + \gamma a_{q_x,n+1}}{\omega(q_x)}$$

$$\omega^2(q_x)a_{q_x,n} = \gamma(\beta a_{q_x,n-1} + \gamma a_{q_x,n}) + \beta(\beta a_{q_x,n} + \gamma a_{q_x,n+1})$$

The above results lead to the following set of equations that are in terms of the  $a$  coefficients only:

$$-a_{q_x, n-1} + \frac{\omega^2(q_x) - (\beta^2 + \gamma^2)}{\gamma\beta} a_{q_x, n} - a_{q_x, n+1} = 0$$

# Appendix C

## Partitioning of the $D_N$ matrix in Chapter 4

In this appendix we list the steps involved in partitioning the  $D_N$  matrix, which was defined in Equation (4.16) of Section 4.2. It follows from Equation (4.16) and the preceding equations that

$$A^{-1} = \begin{pmatrix} A_{11}^{-1} & A_{12}^{-1} & A_{13}^{-1} & \cdots & A_{1n_0-1}^{-1} & A_{1n_0}^{-1} & A_{1n_0+1}^{-1} & \cdots & A_{1n'_0-1}^{-1} & A_{1n'_0}^{-1} & A_{1n'_0+1}^{-1} & \cdots \\ A_{21}^{-1} & A_{22}^{-1} & A_{23}^{-1} & \cdots & A_{2n_0-1}^{-1} & A_{2n_0}^{-1} & A_{2n_0+1}^{-1} & \cdots & A_{2n'_0-1}^{-1} & A_{2n'_0}^{-1} & A_{2n'_0+1}^{-1} & \cdots \\ A_{31}^{-1} & A_{32}^{-1} & A_{33}^{-1} & \cdots & A_{3n_0-1}^{-1} & A_{3n_0}^{-1} & A_{3n_0+1}^{-1} & \cdots & A_{3n'_0-1}^{-1} & A_{3n'_0}^{-1} & A_{3n'_0+1}^{-1} & \cdots \\ \vdots & \vdots & \vdots & \vdots & \vdots & \vdots & \vdots & \vdots & \vdots & \vdots & \vdots & \cdots \\ A_{n1}^{-1} & A_{n2}^{-1} & A_{n3}^{-1} & \cdots & A_{nn_0-1}^{-1} & A_{nn_0}^{-1} & A_{nn_0+1}^{-1} & \cdots & A_{nn'_0-1}^{-1} & A_{nn'_0}^{-1} & A_{nn'_0+1}^{-1} & \cdots \\ \vdots & \vdots & \vdots & \vdots & \vdots & \vdots & \vdots & \vdots & \vdots & \vdots & \vdots & \cdots \\ A_{n'_01}^{-1} & A_{n'_02}^{-1} & A_{n'_03}^{-1} & \cdots & A_{n'_0n_0-1}^{-1} & A_{n'_0n_0}^{-1} & A_{n'_0n_0+1}^{-1} & \cdots & A_{n'_0n'_0-1}^{-1} & A_{n'_0n'_0}^{-1} & A_{n'_0n'_0+1}^{-1} & \cdots \\ \vdots & \vdots & \vdots & \vdots & \vdots & \vdots & \vdots & \vdots & \vdots & \vdots & \vdots & \ddots \end{pmatrix} \quad (\text{C.1})$$

$$\Delta A_N = \begin{pmatrix} \Delta_e & \Delta_s & 0 & 0 & 0 & 0 & 0 & 0 & 0 & 0 & 0 & \dots \\ \Delta_s & 0 & 0 & 0 & 0 & 0 & 0 & 0 & 0 & 0 & 0 & \dots \\ 0 & 0 & 0 & 0 & 0 & 0 & 0 & 0 & 0 & 0 & 0 & \dots \\ 0 & 0 & 0 & 0 & \Delta_{In_0} & 0 & 0 & 0 & 0 & 0 & 0 & \dots \\ 0 & 0 & 0 & \Delta_{In_0} & \Delta_{n_0} & \Delta_{In_0} & 0 & 0 & 0 & 0 & 0 & \dots \\ 0 & 0 & 0 & 0 & \Delta_{In_0} & 0 & 0 & 0 & 0 & 0 & 0 & \dots \\ 0 & 0 & 0 & 0 & 0 & 0 & 0 & 0 & 0 & 0 & 0 & \dots \\ 0 & 0 & 0 & 0 & 0 & 0 & 0 & 0 & \Delta_{In'_0} & 0 & 0 & \dots \\ 0 & 0 & 0 & 0 & 0 & 0 & 0 & \Delta_{In'_0} & \Delta_{n'_0} & \Delta_{In'_0} & 0 & \dots \\ 0 & 0 & 0 & 0 & 0 & 0 & 0 & 0 & \Delta_{In'_0} & 0 & 0 & \dots \\ 0 & 0 & 0 & 0 & 0 & 0 & 0 & 0 & 0 & 0 & 0 & \dots \\ \vdots & \vdots & \vdots & \vdots & \vdots & \vdots & \vdots & \vdots & \vdots & \vdots & \vdots & \ddots \end{pmatrix}, \quad (\text{C.2})$$



which can next be written in the following partitioned form

$$D_N = \left( \begin{array}{c|c} Q & O \\ \hline S & I \end{array} \right), \quad (\text{C.3})$$

where  $O$  is a square null matrix,  $I$  a square identity matrix,  $S$  a square submatrix of  $D_N$ , and  $Q$  is a square submatrix of  $D_N$  with dimension of  $n'_0 + 1 \times n'_0 + 1$ .



# Curriculum Vitae

**Name:** Maher Zakaria Ahmed Selim

**Place of Birth** Cairo, Egypt

**Date of Birth** September 8, 1975

**Post-Secondary Education and Degrees:** Ain Shams University  
Cairo, Egypt  
1993-1997 B.Sc.

Helwan University  
Cairo, Egypt  
2003 - 2006 M.Sc.

University of Western Ontario  
London, ON, Canada  
2007 - 2012 Ph.D.

**Honours and Awards:** M.Sc. Ain Shams University scholarship  
1997-1998

M.Sc. Helwan University scholarship  
2001-2003

Egyptian ministry of higher education and scientific research PhD scholarship  
2007-2011

**Related Work Experience:** Academic compositor  
Hindawi Publishing co.  
1998-1999

Researcher Assistant  
Egyptian National Institute of Standards  
2003- 2007

Teaching Assistant  
The University of Western Ontario  
2008 - 2009

**Publications:**

Maher Ahmed, “The next nearest neighbor effect on the 2D materials properties”, <http://arxiv.org>, arXiv:1111.0104, Nov. 2011.

Maher Ahmed, “Understanding of hopping matrix for 2D materials taking 2D honeycomb and square lattices as study cases”, <http://arxiv.org>, arXiv:1110.6488, Oct. 2011.

Maher Ahmed, “Spin Waves in Ferromagnetic Dots 2D Honeycomb Lattice Stripes”, <http://arxiv.org>, arXiv:1110.5716, Oct. 2011.

Maher Ahmed, “The effect of edge and impurities sites properties on their localized states in semi-infinite zigzag edged 2D honeycomb graphene sheet”, <http://arxiv.org>, arXiv:1110.5105, Oct. 2011.

Maher Ahmed, “Spin Waves in 2D ferromagnetic square lattice stripe”, <http://arxiv.org>, arXiv:1110.4369, Oct. 2011.

Ph.D. thesis “Electronic and magnetic excitations in graphene and magnetic nano-ribbons”, University of Western Ontario, London, ON, Canada, 2012

Maher Ahmed, “A map to unified grand model for space time, particles, fields and universe builded on a trial mathematical physics interpretation of the holy Quran creation story”, [vixra.org](http://vixra.org), viXra:1009.0068, Sep 2010.

Maher Ahmed, “How to help your students win a Nobel Prize: coaching creative thinking through teaching”, online video <http://sciencestage.com/v/27851/>, April 2010.

M.Sc. thesis “Evaluation of moisture content in wood fibre and recommendation of the best method for its determination”, Helwan University, Cairo, Egypt, 2006.

B.Sc. thesis “Application of some nuclear models to even-even Er isotopes”, Ain Shams University, Cairo, Egypt, 1997.